NASA/TP-20220006634

Haystack Ultra-Wideband Satellite Imaging Radar Measurements of the Orbital Debris Environment: 2020

Orbital Debris Program Office

James Murray
Jacobs – Jacobs JETS Contract

Timothy Kennedy
NASA Johnson Space Center

May 2022

NASA STI Program Report Series

The NASA STI Program collects, organizes, provides for archiving, and disseminates NASA's STI. The NASA STI program provides access to the NTRS Registered and its public interface, the NASA Technical Reports Server, thus providing one of the largest collections of aeronautical and space science STI in the world. Results are published in both non-NASA channels and by NASA in the NASA STI Report Series, which includes the following report types:

- TECHNICAL PUBLICATION. Reports of completed research or a major significant phase of research that present the results of NASA Programs and include extensive data or theoretical analysis. Includes compila- tions of significant scientific and technical data and information deemed to be of continuing reference value. NASA counter-part of peer-reviewed formal professional papers but has less stringent limitations on manuscript length and extent of graphic presentations.

- TECHNICAL MEMORANDUM. Scientific and technical findings that are preliminary or of specialized interest, e.g., quick release reports, working papers, and bibliographies that contain minimal annotation. Does not contain extensive analysis.

- CONTRACTOR REPORT. Scientific and technical findings by NASA-sponsored contractors and grantees.

- CONFERENCE PUBLICATION. Collected papers from scientific and technical conferences, symposia, seminars, or other meetings sponsored or co-sponsored by NASA.

- SPECIAL PUBLICATION. Scientific, technical, or historical information from NASA programs, projects, and missions, often concerned with subjects having substantial public interest.

- TECHNICAL TRANSLATION. English-language translations of foreign scientific and technical material pertinent to NASA's mission.

Specialized services also include organizing and publishing research results, distributing specialized research announcements and feeds, providing information desk and personal search support, and enabling data exchange services.

For more information about the NASA STI program, see the following:

- Access the NASA STI program home page at http://www.sti.nasa.gov

- Help desk contact information:

https://www.sti.nasa.gov/sti-contact-form/ and select the "General" help request type.

NASA/TP-20220006634

Haystack Ultra-Wideband Satellite Imaging Radar Measurements of the Orbital Debris Environment: 2020

Orbital Debris Program Office

James Murray
Jacobs – Jacobs JETS Contract

Timothy Kennedy
NASA Johnson Space Center

National Aeronautics and
Space Administration

Johnson Space Center
Houston, Texas 77058

May 2022

ACKNOWLEDGEMENTS

The authors would like to thank Eugene Stansbery and Mark Matney for their thorough technical review of this report and the data contained within. Additionally, the authors would like to thank Drake Gates for his significant contributions to the debris cloud modeling in Section 4.4 of this report. We would like to thank Debra Shoots for her editing contributions. Finally, the authors would like to thank Quanette Juarez for her contributions to the data processing and data quality control efforts.

Available from:

NASA STI Program
Mail Stop 148
NASA Langley Research Center
Hampton, VA 23681-2199

National Technical Information Service
5285 Port Royal Road
Springfield, VA 22161

This report is also available in electronic form at http://www.sti.nasa.gov/ and http://ntrs.nasa.gov

TABLE OF CONTENTS

SECTION **PAGE**

1.0 Introduction 1
1.1 Purpose 1
1.2 Scope 1
1.3 Overview 1
2.0 Radar System Overview 2
2.1 Radar Performance 3
3.0 Radar Processing and Data Collection 6
3.1 Radar Signal Processing at Johnson Space Center 8
3.2 DRADIS Processing 9
3.3 Sphere Track Calibration 9
3.4 Spiral Scan Calibration 10
3.5 RFI Review 12
3.5.1 RFI: Wideband 13
3.5.2 RFI: Narrowband 14
3.6 Radar Calibration using NaK Coolant Droplets 15
3.7 The NASA Size Estimation Model 17
4.0 Results 20
4.1 Data Collection Overview 20
4.2 Radar Measurements 20
4.2.1 Range Versus Range-Rate 21
4.2.2 Altitude Versus Inclination 22
4.2.3 Range Versus Total RCS 23
4.2.4 Polarization Distribution 24
4.2.5 Comparison of Derived Parameters for Cataloged Objects 25
4.3 Environment Characterization Summary 29
4.3.1 SEM-size Cumulative Distribution 29
4.3.2 Flux Versus Altitude 31
4.3.3 Flux Versus Inclination 35
4.4 Breakup Identification 38
4.4.1 SL-23 DEB 38
4.5 HUSIR Observations vs. ORDEM 3.1 predictions 44
5.0 Summary 48
6.0 References 50

Appendix A: Total Number of Hours Received from MIT/LL 52
Appendix B: Empirical Sensitivity Estimation.. 53
Appendix C: HUSIR 75° Elevation, East Pointing, 10.0 GHz 59
Appendix D: HUSIR 75° Elevation, East Pointing, 10.1 GHz 64
Appendix E: HUSIR 10° Elevation, South Pointing, 10.0 GHz 69
Appendix F: HUSIR 10° Elevation, South Pointing, 10.1 GHz 73
Appendix G: HUSIR 20° Elevation, South Pointing, 10.0 GHz.. 77
Appendix H: HUSIR 20° Elevation, South Pointing, 10.1 GHz.. 81

FIGURES

FIGURE **PAGE**

Figure 2-1. HUSIR CY2020 transmit power history for both the 10.0 GHz and 10.1 GHz waveforms. The horizontal dashed line represents the nominal HUSIR transmit power of 250 kW. 4

Figure 2-2. Orbit altitude versus SEM size for HUSIR CY2020 75E data at 10 GHz with 99%, 95%, and 90% completeness curves as a function of altitude. 5

Figure 3-1. An overview of the data collection and analysis. 6

Figure 3-2. Orbital debris data collection and pre- and post-data collection timeline. 7

Figure 3-3. Overview of the radar data processing conducted by DRADIS. 9

Figure 3-4. Histograms of ΔRCS values measured at 10 GHz and 10.1 GHz in CY2020. 10

Figure 3-5. Data visualization in DRADIS of a spiral scan on a GEO satellite. 11

Figure 3-6. Contour plot of polynomial fit to spiral scan data taken at 10.0 GHz. 12

Figure 3-7. Contour plot of polynomial fit to spiral scan data taken at 10.1 GHz. 12

Figure 3-8. Percentage of detections affected by RFI. 13

Figure 3-9. Range-rate versus DOY for CY2020 75E data taken at 10 GHz with wideband RFI identified. 14

Figure 3-10. Example pulse-by-pulse range versus range-rate plot used for narrowband RFI identification. 15

Figure 3-11. Empirical model of NaK RCS distribution. 17

Figure 3-12. RCS distribution of NaK. The shaded regions represent the 2σ uncertainty bounds. 17

Figure 3-13. Illustration of body and projected measurement on complex shape used in determining characteristic length. 18

Figure 3-14. Results of RCS-to-size measurements on 39 representative debris objects. 19

Figure 4-1. Range versus range-rate for the HUSIR 75E data from 2020. 21

Figure 4-2. Altitude versus Doppler inclination for the HUSIR 75E data from 2020. 22

Figure 4-3. Range versus total RCS for the HUSIR 75E data from 2020. 23

Figure 4-4. Orbit altitude versus SEM size for the HUSIR 75E data from 2020. 24

Figure 4-5. Polarization distribution for the HUSIR 75E data from 2020, limited to 5.62 mm and 1000 km altitude. The shaded regions represent the 2σ uncertainty bounds. 25

Figure 4-6. Comparison of the HUSIR-derived size and SSN-reported size HUSIR 75E detections collected in CY2020 with the 10 GHz waveform that correlate to cataloged objects. 27

Figure 4-7. Comparison of the HUSIR-derived size and SSN-reported size HUSIR 75E detections collected in CY2020 with the 10.1 GHz waveform that correlate to cataloged objects. 27

Figure 4-8. Comparison of the Doppler inclination derived from HUSIR data with the cataloged inclination for correlated targets in the CY2020 75E data. 28

Figure 4-9. Comparison of the Doppler inclination derived from HUSIR data with the Doppler inclination for correlated targets calculated from the TLE-predicted range and range-rate. 29

Figure 4-10. SEM-size cumulative distribution for all 10 GHz, 75E data, by year. 30

Figure 4-11. SEM-size cumulative distribution for all CY2020, 75E data. 31
Figure 4-12. Cumulative surface area flux versus altitude limited to 1 cm for all 10 GHz, 75E data, by year. 32
Figure 4-13. Cumulative surface area flux versus altitude limited to 5.62 mm for all 10 GHz, 75E data, by year. 33
Figure 4-14. Cumulative surface area flux versus altitude limited to 1 cm for all CY2020, 75E data. 34
Figure 4-15. Cumulative surface area flux versus altitude limited to 5.62 mm for all CY2020, 75E data. 34
Figure 4-16. Cumulative surface area flux versus inclination limited to 1 cm for all 10 GHz, 75E data, by year. 35
Figure 4-17. Cumulative surface area flux versus inclination limited to 5.62 mm for all 10 GHz, 75E data, by year. 36
Figure 4-18. Cumulative surface area flux versus inclination limited to 1 cm for all CY2020, 75E data. 37
Figure 4-19. Cumulative surface area flux versus inclination limited to 5.62 mm for all CY2020, 75E data. 37
Figure 4-20. Modeled SL-23 DEB (*Fregat*) cloud in range/range-rate space comparing the effect of true anomaly at the time of the breakup on cloud distribution. 40
Figure 4-21. Modeled SL-23 DEB (*Fregat*) cloud in range/range-rate space comparing the effect of true anomaly at the time of the breakup on cloud distribution. 41
Figure 4-22. Count density in altitude and inclination for 74 modeled SL-23 DEB fragment clouds. 43
Figure 4-23. Cumulative flux versus SEM size for objects detected with altitudes between 400 km and 1000 km. 45
Figure 4-24. Surface area flux versus altitude for objects detected with SEM sizes 5.5 mm and larger. 46
Figure 4-25. Surface area flux versus altitude for objects detected with SEM sizes 1 cm and larger. 47
Figure B-1. Cumulative PP XNR for the HUSIR CY2020 75E, 10.1 GHz dataset. 53
Figure B-2. Cumulative PP XSNR versus log10(counts) showing the original distribution in blue and the resampled distribution in orange. 54
Figure B-3. Example ratio of data to fit in the roll off region, with completeness XSNR values and corresponding sizes at 1000 km altitude to 99%, 95%, and 90% indicated. 55
Figure B-4. HUSIR CY2020, 75E, 10.1 GHz cumulative PP XSNR distribution with the original data as a blue line, the resampled points used in the fit as red "+" symbols, the fit as a dashed black line, and the XSNR levels of 99%, 95%, and 90% as red dashed, dotted, and dash-dotted vertical lines. 56
Figure B-5. HUSIR CY2020, 75E, 10.0 GHz cumulative PP XSNR distribution with the original data as a blue line, the resampled points used in the fit as red "+" symbols, the fit as a dashed black line, and the XSNR levels of 99%, 95%, and 90% as red dashed, dotted, and dash-dotted vertical lines. 56
Figure B-6. HUSIR CY2020, 20S, 10.1 GHz cumulative PP XSNR distribution with the original data as a blue line, the resampled points used in the fit as red "+" symbols, the fit as a dashed black line, and the XSNR levels of 99%, 95%, and 90% as red dashed, dotted, and dash-dotted vertical lines. 57

Figure B-7. HUSIR CY2020, 20S, 10.0 GHz cumulative PP XSNR distribution with the original data as a blue line, the resampled points used in the fit as red "+" symbols, the fit as a dashed black line, and the XSNR levels of 99%, 95%, and 90% as red dashed, dotted, and dash-dotted vertical lines. 57
Figure B-8. HUSIR CY2020, 10S, 10.1 GHz cumulative PP XSNR distribution with the original data as a blue line, the resampled points used in the fit as red "+" symbols, the fit as a dashed black line, and the XSNR levels of 99%, 95%, and 90% as red dashed, dotted, and dash-dotted vertical lines. 58
Figure B-9. HUSIR CY2020, 10S, 10.0 GHz cumulative PP XSNR distribution with the original data as a blue line, the resampled points used in the fit as red "+" symbols, the fit as a dashed black line, and the XSNR levels of 99%, 95%, and 90% as red dashed, dotted, and dash-dotted vertical lines. 58
Figure C-1. Range versus Range-Rate, HUSIR 75E, CY2020. 59
Figure C-2. Altitude versus Doppler inclination, HUSIR 75E, CY2020. 59
Figure C-3. Range versus Radar Cross Section, HUSIR 75E, CY2020. 60
Figure C-4. Cumulative count rate versus SEM Size, HUSIR 75E, CY2020. 60
Figure C-5. Cumulative count rate versus detection SNR of the principal polarization, HUSIR 75E, CY2020. 61
Figure C-6. Cumulative count rate versus Total Radar Cross Section, HUSIR 75E, CY2020. 61
Figure C-7. Count Rate versus polarization ratio, HUSIR 75E, CY2020. 62
Figure C-8. Flux versus altitude, HUSIR 75E, CY2020. No size or altitude limits are applied. 62
Figure C-9. Flux versus orbital inclination, HUSIR 75E, CY2020. No size or altitude limits are applied. 63
Figure D-1. Range versus Range-Rate, HUSIR 75E, CY2020. 64
Figure D-2. Altitude versus Doppler inclination, HUSIR 75E, CY2020. 64
Figure D-3. Range versus Radar Cross Section, HUSIR 75E, CY2020. 65
Figure D-4. Cumulative count rate versus SEM Size, HUSIR 75E, CY2020. 65
Figure D-5. Cumulative count rate versus detection SNR of the principal polarization, HUSIR 75E, CY2020. 66
Figure D-6. Cumulative count rate versus Total Radar Cross Section, HUSIR 75E, CY2020. 66
Figure D-7. Count Rate versus polarization ratio, HUSIR 75E, CY2020. 67
Figure D-8. Flux versus altitude, HUSIR 75E, CY2020. No size or altitude limits are applied. 67
Figure D-9. Flux versus orbital inclination, HUSIR 75E, CY2020. No size or altitude limits are applied. 68
Figure E-1. Range versus Range-Rate, HUSIR 10S, CY2020. 69
Figure E-2. Altitude versus Doppler inclination, HUSIR 10S, CY2020. 69
Figure E-3. Range versus Radar Cross Section, HUSIR 10S, CY2020. 70
Figure E-4. Cumulative count rate versus SEM size, HUSIR 10S, CY2020. 70
Figure E-5. Cumulative count rate versus detection SNR of the principal polarization, HUSIR 10S, CY2020. 71
Figure E-6. Cumulative count rate versus Total Radar Cross Section, HUSIR 10S, CY2020. 71
Figure E-7. Count Rate versus polarization ratio, HUSIR 10S, CY2020. 72
Figure F-1. Range versus Range-Rate, HUSIR 10S, CY2020. 73
Figure F-2. Altitude versus Doppler inclination, HUSIR 10S, CY2020. 73

Figure F-3. Range versus Radar Cross Section, HUSIR 10S, CY2020. 74
Figure F-4. Cumulative count rate versus SEM size, HUSIR 10S, CY2020. 74
Figure F-5. Cumulative count rate versus detection SNR of the principal polarization, HUSIR 10S, CY2020. 75
Figure F-6. Cumulative count rate versus Total Radar Cross Section, HUSIR 10S, CY2020. 75
Figure F-7. Count Rate versus polarization ratio, HUSIR 10S, CY2020. 76
Figure G-1. Range versus Range-Rate, HUSIR 20S, CY2020. 77
Figure G-2. Altitude versus Doppler inclination, HUSIR 20S, CY2020. 77
Figure G-3. Range versus Radar Cross Section, HUSIR 20S, CY2020. 78
Figure G-4. Cumulative count rate versus SEM size, HUSIR 20S, CY2020. 78
Figure G-5. Cumulative count rate versus detection SNR of the principal polarization, HUSIR 20S, CY2020. 79
Figure G-6. Cumulative count rate versus Total Radar Cross Section, HUSIR 20S, CY2020. 79
Figure G-7. Count Rate versus polarization ratio, HUSIR 20S, CY2020. 80
Figure H-1. Range versus Range-Rate, HUSIR 20S, CY2020. 81
Figure H-2. Altitude versus Doppler inclination, HUSIR 20S, CY2020. 81
Figure H-3. Range versus Radar Cross Section, HUSIR 20S, CY2020. 82
Figure H-4. Cumulative count rate versus SEM size, HUSIR 20S, CY2020. 82
Figure H-5. Cumulative count rate versus detection SNR of the principal polarization, HUSIR 20S, CY2020. 83
Figure H-6. Cumulative count rate versus Total Radar Cross Section, HUSIR 20S, CY2020. 83
Figure H-7. Count Rate versus polarization ratio, HUSIR 20S, CY2020. 84

TABLES

TABLE **PAGE**

Table 2-1: HUSIR Location with Respect to the 1984 World Geodetic System (WGS 84) Earth Model ... 2
Table 2-2: Radar Debris Mode Nominal Operating Parameters ... 2
Table 2-3. Sensitivity at 1000 km for All CY2020 HUSIR Datasets to 99%, 95%, and 90% Levels of Completeness ... 5
Table 3-1: DRADIS Signal Processing Parameters ... 8
Table 4-1. Minimum and Maximum Observable Ranges and Corresponding Orbital Altitudes for Observation Geometry ... 20
Table 4-2: Data Collection Summary Reflecting the Final Curated Data Set ... 20
Table 4-3. All Known Breakups that Occurred in CY2020, as of 3 February 2021 ... 38
Table A-1: Data Collection Summary Reflecting the Total Number of Observation Hours Received from MIT/LL in CY2020 ... 52

Acronyms

ASAT	Anti-Satellite
AZ	Azimuth
CY	Calendar Year
CW	Continuous Wave
DOY	Day of Year
dB	Decibels
DBSCAN	Density-based spatial clustering of applications with noise
dBsm	Square meters measured in decibels
DRADIS	Debris Radar Automated Data Inspection System
EL	Elevation
FFT	Fast Fourier Transform
FOC	Full Operating Capability
FY	Fiscal Year
GEO	Geostationary Orbit
GMT	Greenwich Mean Time
HAX	Haystack Auxiliary Radar
HUSIR	Haystack Ultra-Wideband Satellite Imaging Radar
I	In-phase
JSC	Johnson Space Center
LEO	Low Earth Orbit
MIT/LL	Massachusetts Institute of Technology/Lincoln Laboratory
NaK	Sodium-Potassium
NASA	National Aeronautics and Space Administration
NWF	New Waveform
OD	Orbital Debris
ODPO	Orbital Debris Program Office
OP	Orthogonal Polarization
ORDEM	Orbital Debris Engineering Model
PCHIP	Piecewise Cubic Hermite Interpolating Polynomial
PP	Principal Polarization
Q	Quadrature, Quadrature-phase
RAAN	Right Ascension of the Ascending Node
R/B	Rocket Body
RCS	Radar Cross Section (typically reported in dBsm)
RDI	Range Doppler Image
RF	Radio Frequency
RFI	Radio Frequency Interference

RORSAT	Radar Ocean Reconnaissance SATellites
ROSA	Radar Open System Architecture
SEM	Size Estimation Model
SNR	Signal-to-Noise Ratio
SpaceX	Space Exploration Technologies Corp.
SSBM	Standard Satellite Break-up Model
SSN	U.S. Space Surveillance Network
TLE	Two-line Element Set
TWT	Traveling-wave Tube
WGS	World Geodetic System
WFC	Waveform Code
XSNR	Excess SNR

(This page intentionally left blank)

1.0 Introduction

1.1 PURPOSE

This report summarizes radar measurement data of the orbital debris (OD) environment in low Earth orbit (LEO) from the Haystack Ultra-wideband Satellite Imaging Radar (HUSIR) operated by the Massachusetts Institute of Technology's Lincoln Laboratory (MIT/LL) and provided to the National Aeronautics and Space Administration (NASA) Orbital Debris Program Office (ODPO).

1.2 SCOPE

The period covered by this report includes data collected during calendar year (CY) 2020. Additionally, data from CY2018 and CY2019 are included for year-to-year comparison purposes. Data collected from the Haystack Auxiliary Radar (HAX), during the same period, will be presented in a separate report.

Results presented in this report represent a broad overview of the current state of the OD environment in LEO, as measured by HUSIR. Limited analysis of breakups of interest is also presented.

1.3 OVERVIEW

The NASA ODPO relies primarily on ground-based radar measurements to characterize the distribution of small debris in low Earth orbit down to limiting sizes determined by the sensitivities of each radar. Since 1990, MIT/LL has been collecting radar measurements for the NASA ODPO under agreements with the U.S. Department of Defense [1]. This first began with the Haystack radar (now HUSIR) in October 1990 and was then supplemented by the HAX radar beginning in March 1994. The NASA ODPO has historically received nominally 1000 hours of data collected per U.S. Government Fiscal Year (FY), approximately 600 of which were collected by HUSIR and 400 of which were collected by HAX. Contract changes in FY2020 reduced the target number of hours to 500 per FY for HUSIR and radar data is no longer being collected by HAX for the NASA ODPO. Both radars operate in a stare mode designed to statistically sample objects in LEO that are smaller than those typically tracked and cataloged by the U.S. Space Command's Space Surveillance Network (SSN).

Historically, the ODPO has used these radars to sample the OD environment down to approximately 3 cm with HAX and 5.5 mm with HUSIR to an altitude of up to 1000 km. The data collected by these radars is used to characterize the OD environment in altitude, inclination, and size for a large fraction of LEO (altitude < 2000 km) – limited by the latitude, pointing geometry, and sensitivity of each sensor – and eccentric orbits traversing LEO.

This report includes an overview of HUSIR's radar systems, radar signal processing, radar measurements, and environment characterization. Some background information, originally presented in previous HUSIR radar reports, is repeated here for the benefit of the reader.

2.0 Radar System Overview

Located in Tyngsborough, Massachusetts, the HUSIR radar is of a Cassegrain configuration with a focus at the coordinates described in Table 2-1 [2].

Table 2-1: HUSIR Location with Respect to the 1984 World Geodetic System (WGS 84) Earth Model

	Latitude	Longitude	Elevation
HUSIR	42.623287° N	288.511846° E	115.69 m

The HUSIR radar consists of a 36.6 meter-diameter parabolic reflector transmitting right-hand circularly-polarized waveforms and receiving both right- and left-hand circularly-polarized returns – representing the orthogonal polarization (OP) and principal polarization (PP) channels, respectively, of the radar. The waveform for OD measurements – referred to internally as waveform code 4 – consists of transmitting a pulsed continuous wave (CW) signal at X-band with a center frequency of 10 GHz. In CY2020, data collection using a new waveform (NWF) with a center frequency of 10.1 GHz was also conducted. The operating parameters of waveform code 4 are found in Table 2-2. Other waveforms of interest are waveform codes 1 and 11, which are used to calibrate the radar. Additional details are provided in section 3.0.

Table 2-2: Radar Debris Mode Nominal Operating Parameters

Operating Parameter	HUSIR
Peak Power (kW)	250
Transmitter Frequency (GHz)	10.0/10.1
Transmitter Wavelength (cm)	3.0
Antenna Diameter (m)	36.6
Antenna Half-power Beamwidth (deg)	0.058
Antenna Gain (dB)	67.23
System Temperature (K)	186
Total System Losses (dB)	3.9
Waveform Code	4
Range Gates	16
Intermediate Frequency Bandwidth (kHz)	1250
Independent Range/Doppler Samples	15158
FFT Size	16384
Number of non-coherently integrated pulses used for detection	16
Pulse Width (msec)	1.6384
Receive Window (msec)	12.1264
Pulse Repetition Frequency (Hz)	60
Nominal Sensitivity (dB)	59.2
Average Power (kW)	24.6
Doppler Extent (km/s)	±7.5

The HUSIR radar also features a monopulse feed horn capable of estimating object position in the beam with a single pulse using amplitude-comparison monopulse techniques. While traditionally used for maintaining tracked objects on boresight, instead the NASA ODPO uses monopulse to estimate an object's path through the beam while the radar remains stationary (beam-park mode).

The 16 range gates, referenced in Table 2-2, refer to the number of range gates used in the initial detections performed by MIT/LL using their real time processor, discussed in section 3.0. Subsequent processing of the data by the NASA ODPO uses a higher number of range gates to reduce the effects of discretization.

Over the past several years, radio frequency interference (RFI) has become more prevalent at the center frequency of the debris waveform. Preliminary testing by MIT/LL showed that shifting the center frequency of the waveform to 10.1 GHz significantly reduced the effects of RFI on collected data without significantly affecting the nominal operating parameters of the radar. To validate the performance of this new waveform, data was taken at both 10 GHz and 10.1 GHz center frequencies in CY2020. Comparisons between the two waveforms are presented throughout this report. While the center frequency of the new waveform has changed, the waveform code designations have not.

2.1 RADAR PERFORMANCE

The nominal sensitivity of HUSIR is 59.2 decibels (dB), where sensitivity is defined as the single pulse signal-to-noise ratio (SNR) for an object with a radar cross section (RCS) of one square meter at 1000 km slant range. Of the operating parameters that significantly affect sensitivity, transmit power is the most variable, and understanding its history over the CY is of interest. Figure 2-1 shows the transmitted power history of HUSIR during CY2020 at both 10 GHz and 10.1 GHz.

During the entirety of CY2020, HUSIR operated with all four traveling wave tubes (TWTs). For the first two months they were operated at a lower set point voltage that reduced transmission power as part of a conditioning period for a TWT that was replaced during CY2019. HUSIR experienced minimal downtime during CY2020, with the only extended period being related to a solid-state upgrade to the modulator that occurred from August to October. A brief period of downtime occurred in November after a waveguide dry-air compressor failure, after which HUSIR came back online at lower power temporarily before returning to full power by the end of November.

Figure 2-1 also shows that the peak power of the 10.1 GHz waveform is slightly higher than that of the 10 GHz waveform on average. Based on test measurements taken by MIT/LL between April and June 2020, the average peak power for the 10 GHz waveform during this time was 183 kW, while the average peak power for the 10.1 GHz waveform during this time was 196 kW: a 13 kW increase. This corresponded to a 0.4 dB increase in sensitivity overall.

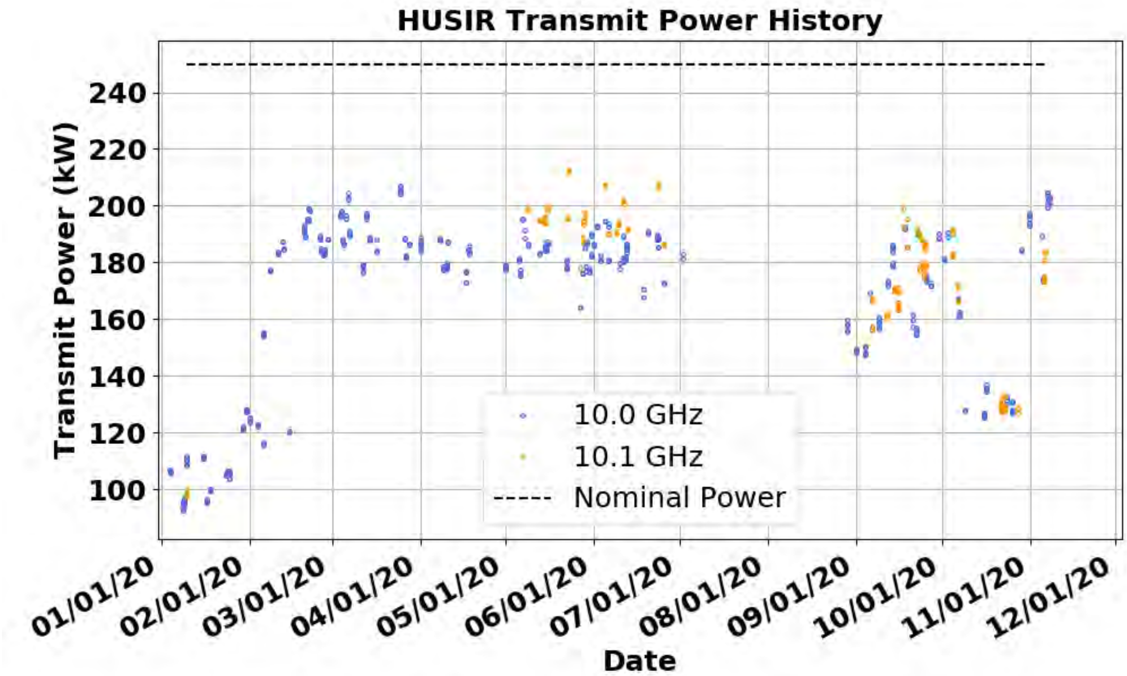

Figure 2-1. HUSIR CY2020 transmit power history for both the 10.0 GHz and 10.1 GHz waveforms. The horizontal dashed line represents the nominal HUSIR transmit power of 250 kW.

The altitude-dependent size of debris that can be detected by HUSIR is determined by sensitivity and staring geometry. There are three staring geometries employed by the NASA ODPO; 75° elevation, due East (75E); 20° elevation, due South (20S); and 10° elevation, due South (10S). These geometries are discussed further in Section 3.0. Figure 2-2 shows the sensitivity curves as a function of altitude of HUSIR CY2020 75E data at 10 GHz to 99%, 95%, and 90% completeness levels, which are overlaid on a scatter plot of orbit altitude versus Size Estimation Model (SEM) size for the dataset. These completeness curves are estimated from the data and a complete description of the methodology is presented in Appendix B. These curves represent the altitude-dependent size at which the prescribed percentage of objects passing through the beam are detected. From the figure, the HUSIR CY2020 75E data at 10 GHz is approximately 99% complete down to a size of 6 mm at 1000 km altitude. Table 2-3 shows the sensitivity at 1000 km for all HUSIR CY2020 datasets to 99%, 95%, and 90% levels of completeness.

Table 2-3. Sensitivity at 1000 km for All CY2020 HUSIR Datasets to 99%, 95%, and 90% Levels of Completeness

Completeness	75E 10 GHz	75E 10.1 GHz	20S 10 GHz	20S 10.1 GHz	10S 10 GHz	10S 10.1 GHz
99%	6.0 mm	6.0 mm	1.5 cm	1.5 cm	3.1 cm	2.9 cm
95%	5.8 mm	5.8 mm	1.3 cm	1.3 cm	2.8 cm	2.6 cm
90%	5.7 mm	5.7 mm	1.2 cm	1.2 cm	2.6 cm	2.5 cm

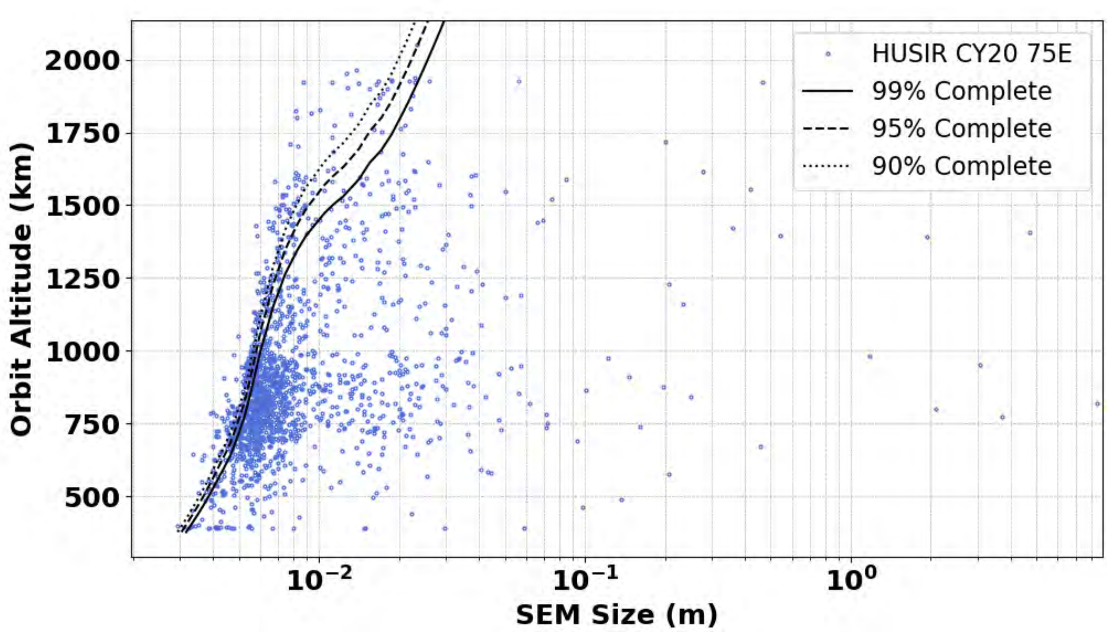

Figure 2-2. Orbit altitude versus SEM size for HUSIR CY2020 75E data at 10 GHz with 99%, 95%, and 90% completeness curves as a function of altitude.

3.0 Radar Processing and Data Collection

For OD radar data collection, both the HUSIR and HAX radars operate in a "beam-park" mode in which the radar antenna is pointed at a fixed elevation (EL) and azimuth (AZ), allowing portions of the debris environment to randomly pass through the radar beam. This provides a fixed detection volume that simplifies calculations of the debris flux, or number of objects detected per unit area, per unit time. Since the radar does not change its pointing in beam-park mode, and the radar beam has a 0.058° beamwidth, the observation time is short and relatively few pulses are collected on each object. Although this limits the precise measurement of a detected object's orbital parameters, the pointing geometry can be utilized to provide meaningful orbital information.

Typically, OD radar data is collected in one of three staring geometries: 75E, 20S, and 10S. By staring just off-zenith, the 75E staring geometry allows the radar to measure Doppler shifts that give meaningful orbital information for orbital inclinations between approximately 40° inclination and 140° inclination – using a circular orbit approximation. The 75E staring geometry comprises approximately two-thirds of the total observation time spent collecting OD radar data from HUSIR each year. The remaining third of observation time is split approximately evenly between the 10S and 20S geometries. Although these geometries suffer from reduced sensitivity due to increased atmospheric attenuation and free space path loss for a given altitude, they allow HUSIR to view lower orbital inclinations down to approximately 20°.

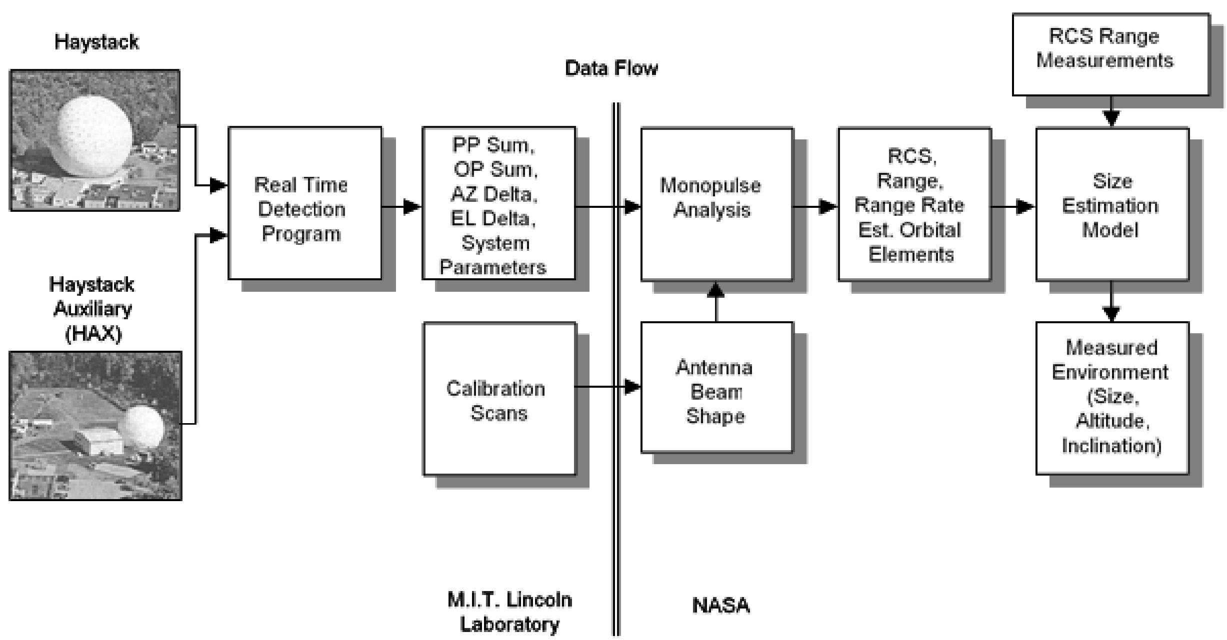

M.I.T. Lincoln Laboratory ***NASA Johnson Space Center***

Figure 3-1. An overview of the data collection and analysis.
Images reprinted with permission Courtesy of MIT/LL, Lexington, Massachusetts.

Figure 3-1 gives an overview of the data collection and analysis performed by MIT/LL and the NASA ODPO. At the radar, MIT/LL employs the Radar Open System Architecture (ROSA) control system to perform real time target detection. ROSA is programmed to record data in a buffer that is saved only when the integrated SNR exceeds a predetermined threshold in the PP channel. If the threshold continues to be exceeded, the buffer continues to record pulses. Additionally, several pulses from before and after the threshold was exceeded are recorded to minimize the loss of useful data and define the noise background.

Currently, MIT/LL is developing hardware to perform continuous recording of every pulse emitted by the radar during an observation. In this scheme, rather than performing real time detection, all data will be saved, and detection will be performed during post-processing. This will allow for new post-processing techniques to be applied that were previously too stressing for real time, like OP channel detection, use of multiple detection algorithms, interference rejection, and detection of transmitter drop out. It will also enable revisiting raw data with new or improved detection algorithms. Once implemented, MIT/LL will perform this post-processing to produce a file containing only PP channel detections, similar to what is currently received, for delivery to the NASA ODPO. MIT/LL will then archive the continuous record data collected during a FY for possible future use or as a data backup.

MIT/LL performs regular calibration scans in the form of calibration sphere tracks (.S files) and spiral scans (.R files) in addition to the debris mode observations. These are nominally performed at the beginning and end of debris data collects using a waveform code (WFC) combination of WFC-11 for tracking and WFC-1 for calibration measurements, as illustrated in Figure 3-2. Additional details regarding the calibration sphere tracks and spiral scans are discussed in Sections 3.3 and 3.4.

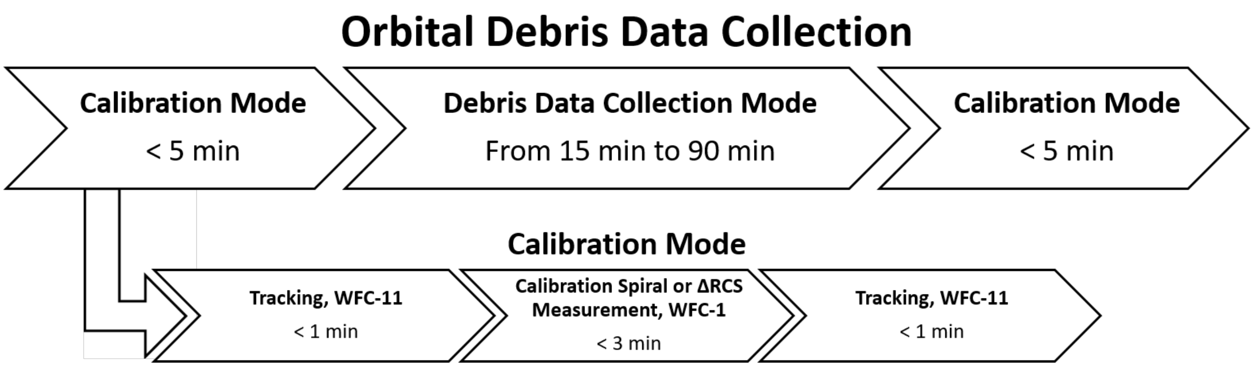

Figure 3-2. Orbital debris data collection and pre- and post-data collection timeline.MIT/LL conducts the object track using the narrow band WFC-11. They conduct the beam shape calibration spiral using the CW WFC-1. One or more calibration mode segments may be conducted before and after each data validation mode segment.

When performing 10 GHz debris observations, the RFI environment is continually monitored, and operators are instructed to switch to the 10.1 GHz waveform when RFI interrupts a data collection. Under these circumstances, operators must collect both 10 GHz and 10.1 GHz calibrations with the expectation that RFI will occur. The overhead of the current process adds additional incentive to a permanent switch to the 10.1 GHz waveform. It will simplify the collection process and increase debris collection uptime.

3.1 RADAR SIGNAL PROCESSING AT JOHNSON SPACE CENTER

The NASA ODPO performs radar signal processing at Johnson Space Center (JSC) using the in-house developed Debris Radar Automated Data Inspection System (DRADIS). DRADIS is a tested and validated software tool, in use since 2018, and has been used to process data from FY2014 to present. All radar data presented in this report was processed using the full operating capability (FOC) version 1.4.3 of DRADIS.

Using DRADIS to process data from MIT/LL requires setting several signal processing parameters. Table 3-1 lists these signal processing parameters, the stage of the processing that each parameter is associated with, and the values used to detect and measure the OD in the observations presented in this report.

Table 3-1: DRADIS Signal Processing Parameters

Processing Parameter	Value
Range Doppler Image	
FFT Size	Zero-padded to 16384 samples
Observation Length	2048 samples
Number of Range Gates	32
Weighting/Windowing	None/Rectangle
Detection	
Detector Type	Non-coherent Integration
Detection Channel	PP
Number of pulses integrated	16
Detection SNR Threshold	5.65 dB
Monopulse Threshold	11 dB
FFT Peak Interpolation	False
Measurement	
Measurement FFT Size	Zero-padded to 16384 samples
FFT Peak Interpolation	True
Monopulse Mode	Legacy
Matched Filter Least Squares Fit	False
Use Integrated Range	True
Validation	
Valid SNR Threshold	5.65 dB

In addition to DRADIS, several other post-processing techniques are employed to improve the quality and consistency of data from year-to-year. These include screening for and excising RFI and a secondary calibration verification using the properties of the sodium-potassium (NaK) OD family. A comprehensive, step-by-step process from the collection of data to the verification of the final detection list can be found in Section 3.1 of [3].

3.2 DRADIS PROCESSING

A high level overview of the operations performed by DRADIS during the processing of debris data files is shown in Figure 3-3. DRADIS employs a multi-pass approach consisting of a detection pass and two measurement passes. The detection pass consists of generating a range Doppler image (RDI) from the in-phase (I) and quadrature-phase (Q) samples and applying an SNR threshold to determine whether an object is present using the user-specified processing parameters – as shown in Table 3-1. Initial estimates of the Doppler frequency, SNR, and approximate sample offset in the range gate containing the detection are made during the detection pass and used as inputs to the first measurement pass. The first measurement pass occurs at the individual detection level and performs measurements such as range, range-rate, monopulse voltage ratios, monopulse angle offsets, and PP and OP RCS on a pulse-by-pulse basis.

The second measurement pass occurs at the detection group level and uses information from all pulses within a detection group to estimate the object's path through the beam and make estimates of the target's orbital elements and target parameters. These include the object's range and range-rate; PP and OP SNR; Doppler-derived orbit inclination; beam path-corrected PP and OP RCS; and NASA SEM-generated size estimate. Detailed descriptions of the detection and measurement passes can be found in Section 3.2 of [3].

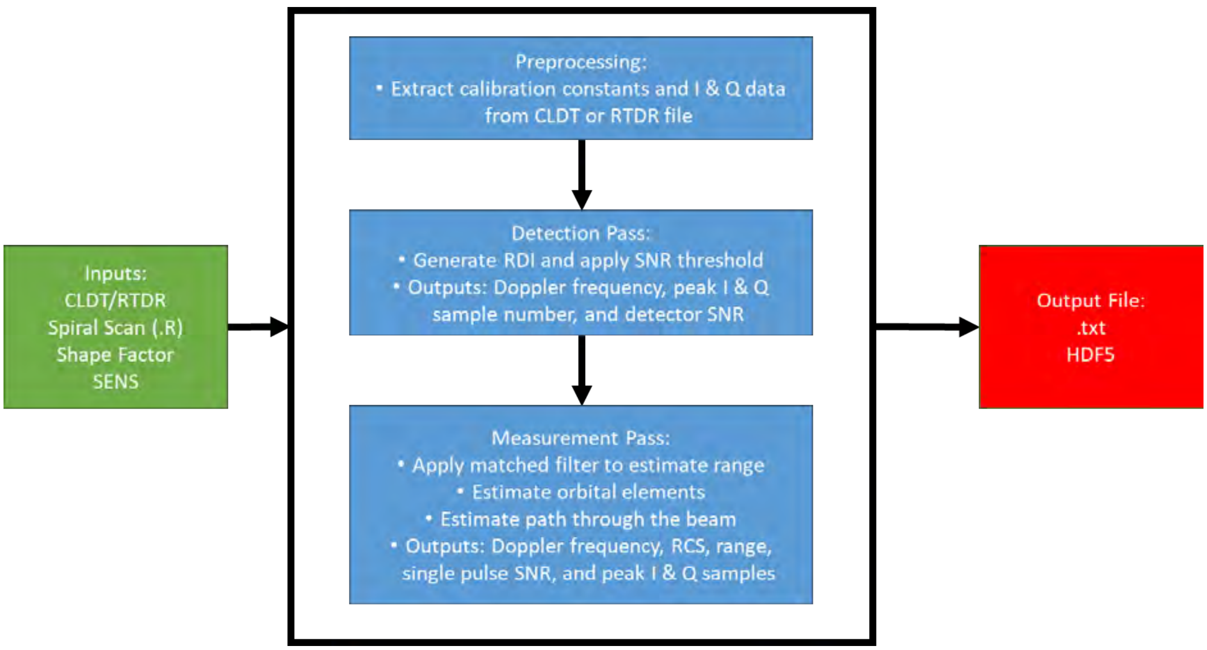

Figure 3-3. Overview of the radar data processing conducted by DRADIS.

3.3 SPHERE TRACK CALIBRATION

The operators at MIT/LL regularly perform end-to-end calibration of the radar system to minimize measurement errors. Several times a day the operators track and measure the RCS of known calibration spheres. These include calibration spheres with SSN object numbers: 900, 902, 1520, 1512, and 5398, as they pass through the radar field of view. A correction factor, known as the ΔRCS, is calculated from the difference of the measured RCS and the known RCS of the given sphere (in decibels), as shown in the following equation:

$$\Delta RCS = RCS_{measured} - RCS_{theoretical}$$

This process is carried out before every OD radar data collection and the ΔRCS is applied in post-processing to the collected data. Separate calibrations are performed for the 10 GHz and 10.1 GHz waveforms. Figure 3-4 shows histograms of the ΔRCS values measured for the 10 GHz and 10.1 GHz waveforms in CY2020. While the average ΔRCS is slightly lower at 10.1 GHz, the overall distribution is similar for both waveforms.

Only the PP channel can be calibrated using the sphere track method due to the scattering properties of the calibration objects, which are metallic spheres. MIT/LL periodically calibrates the magnitude and phase error of the OP channel relative to the PP channel by injecting a calibration signal into both the PP and OP channels.

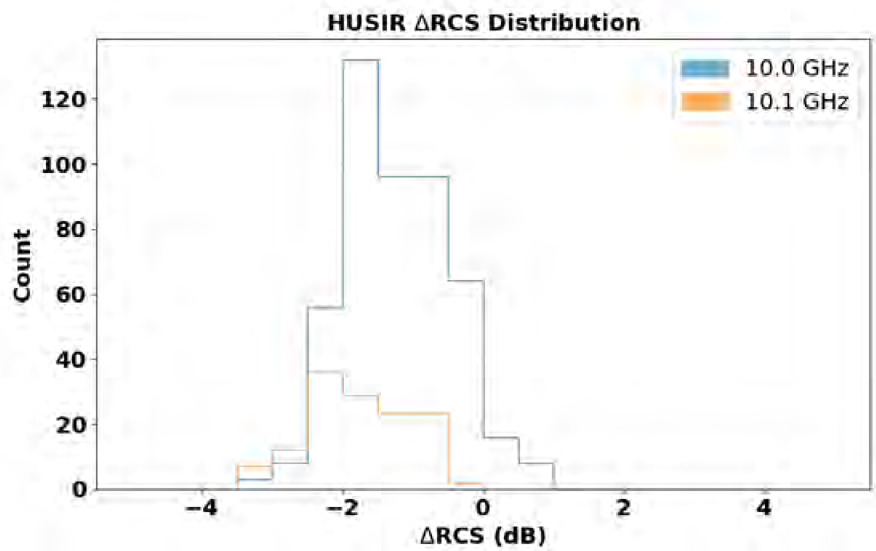

Figure 3-4. Histograms of ΔRCS values measured at 10 GHz and 10.1 GHz in CY2020.

3.4 SPIRAL SCAN CALIBRATION

To calibrate the antenna beam gain pattern, MIT/LL performs spiral scan calibrations before an OD radar data collection period. The spiral scan process involves tracking a calibration object and then performing a slow spiral centered on the object from boresight outward to the edge of the beam in such a way as to adequately sample the full two-sided, 3-dB beamwidth. This data is then used to fit a beam shape. Since it is easier to spiral around a stationary point relative to the radar, spiral scans on geostationary orbit (GEO) objects are preferable to those on LEO objects. Additionally, over the spiral scan calibration period a 3-axis-stabilized GEO object should provide a constant RCS. Figure 3-5 shows a DRADIS visualization of a spiral scan on a GEO target.

Only the PP channel is calibrated using the spiral scan method, since both GEO satellites and LEO calibration spheres are used as targets. The OP beam shape is assumed to be the same as the PP beam shape.

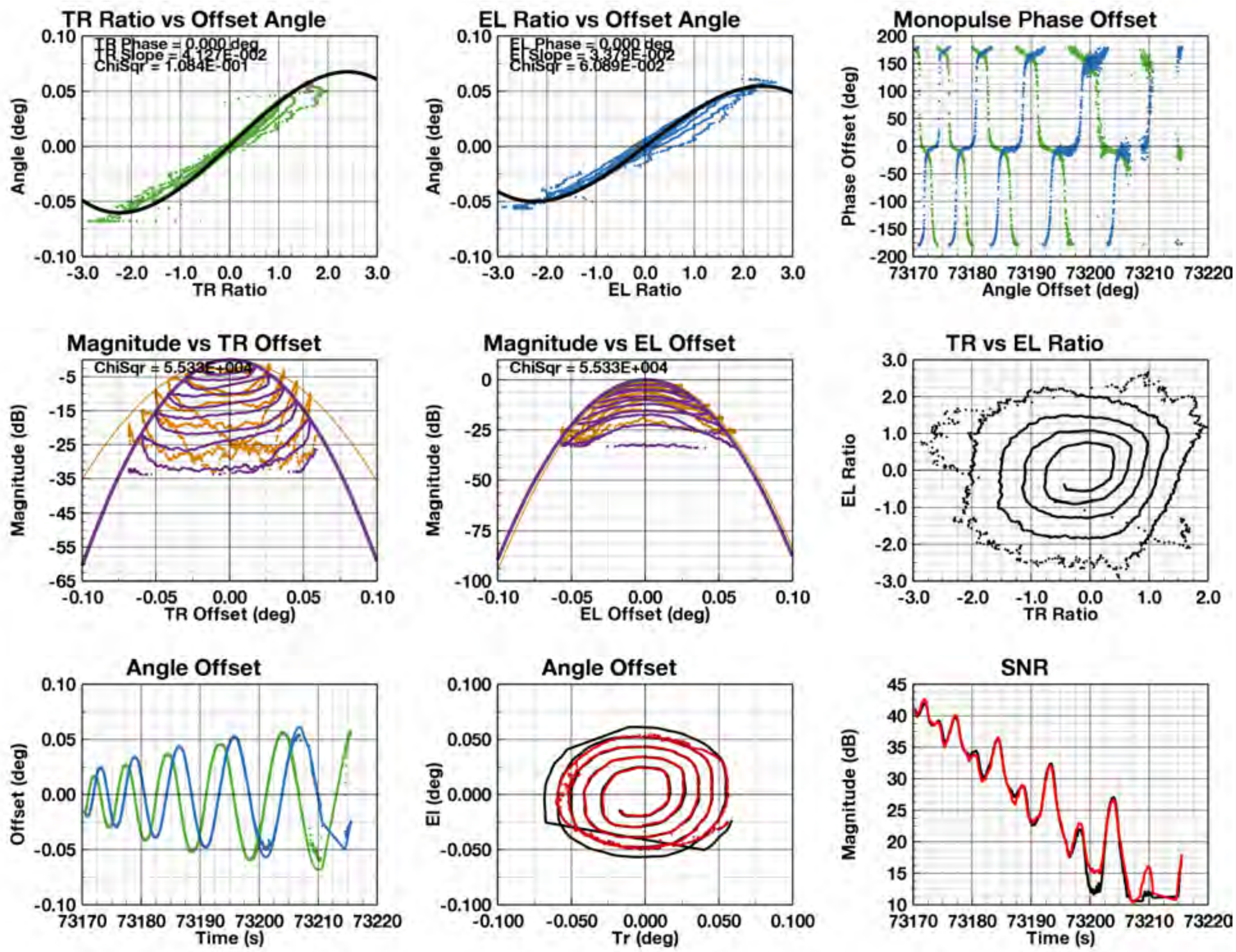

Figure 3-5. Data visualization in DRADIS of a spiral scan on a GEO satellite.

Separate spiral scan calibrations are performed for both the 10 GHz and 10.1 GHz waveforms. Figure 3-6 and Figure 3-7 show contour plots of polynomial fits to spiral scan data taken at 10 GHz and 10.1 GHz, respectively. These spiral scans were performed on SSN object number 23846 on 9 January 2020 during preliminary waveform testing. The results indicate that the beam pattern is similar at both frequencies. The fractional difference in beamwidth of the fitted beam patterns between the two scans was less than 1%.

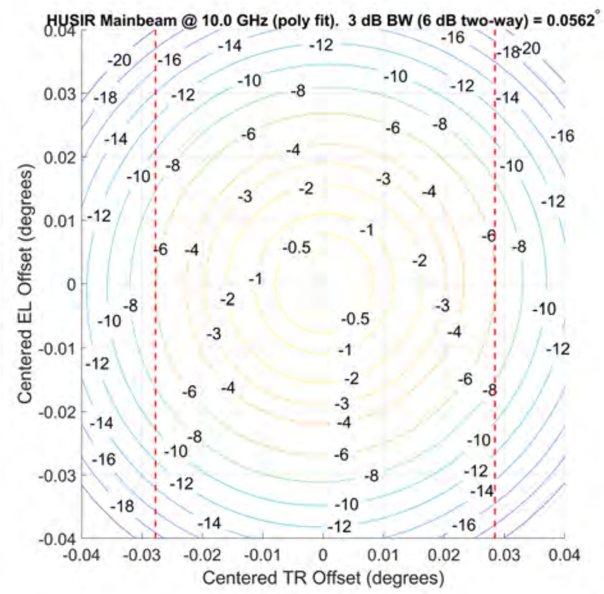

Figure 3-6. Contour plot of polynomial fit to spiral scan data taken at 10.0 GHz.

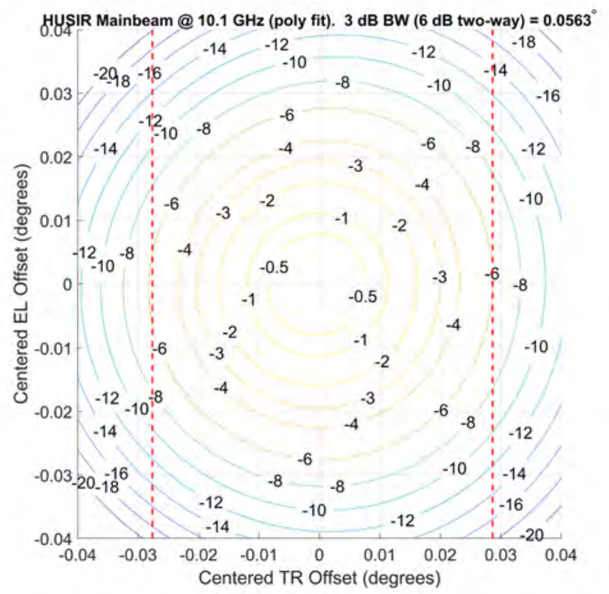

Figure 3-7. Contour plot of polynomial fit to spiral scan data taken at 10.1 GHz.

3.5 RFI REVIEW

During processing of the FY2014–2017 HUSIR data using DRADIS data visualization capabilities, a subset of signals characterized by wideband signatures was identified as RFI and not OD. Since then, mitigation techniques implemented by MIT/LL have reduced the proportion of data affected by this wideband RFI. The percentage of detections determined to be affected by RFI, however, has still increased significantly over the past several years, as shown in Figure 3-8. This is due to the appearance of a second form of RFI, characterized by a persistent narrowband signature, first identified in the CY2018 dataset. Previously implemented mitigation techniques were not effective against this narrowband RFI since this is thought to be some form of self-interference with other radio frequency (RF) systems at MIT/LL.

Due to the increased prevalence of this new form of RFI, the percentage of detections affected by RFI increased in CY2020 to 52.2%; over half of all detections were affected by RFI. When RFI is present in an observation, the detection rate increases relative to nominal detection rates for valid OD detections, and the 52.2% of detections, determined to be affected by RFI in CY2020, corresponds to about 38.3% of the total observation hours being affected, counted on a file-by-file basis. This too is an increase from the 25.5% of hours affected in CY2019 and 10.5% of hours affected in CY2018.

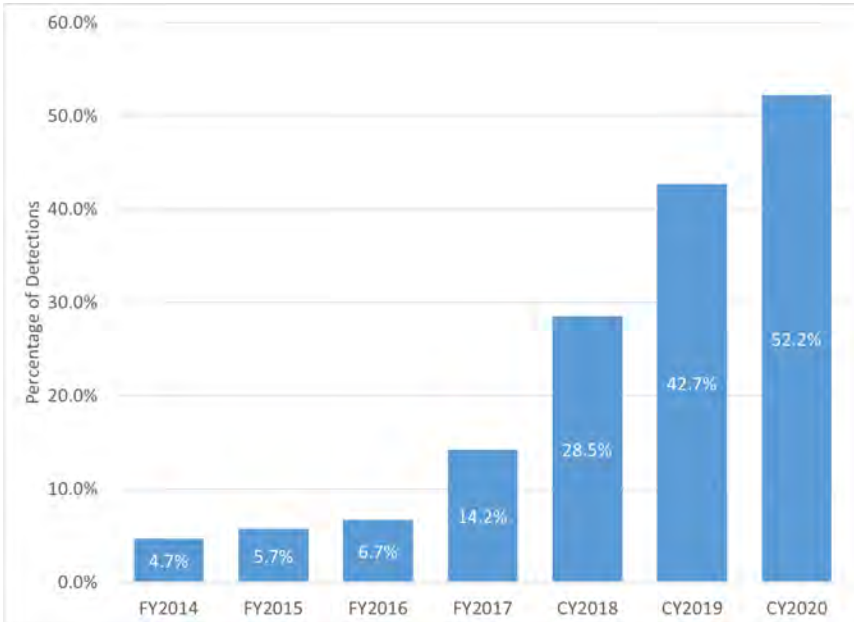

Figure 3-8. Percentage of detections affected by RFI.

As the prevalence of RFI in the data increases, it restricts the number of hours of clean data available for analysis. The experimental 10.1 GHz waveform was developed to move the center frequency away from the RFI-prone 10 GHz to a less noisy band. Of the data taken at 10.1 GHz, only 1.7% of hours were affected by any form of RFI: a significant improvement. Furthermore, all affected hours for the 10.1 GHz waveform were taken at a low elevation angle, 10°, which is a staring geometry inherently prone to the interception of stray terrestrial signals. Moving forward, it is of interest to switch to the new 10.1 GHz for all observations due to its exceptional RFI mitigation performance.

3.5.1 RFI: Wideband

The RFI previously identified in FY2014–2017, with its wideband signature, exhibits an approximately uniform distribution of measured range-rates. These signals may arise from the carriers or subcarriers of various communication systems or be due to harmonics of the frequencies employed in a communication system due to the sensitivity of the radar. Previously, the procedure for collecting radar data at MIT/LL was for the radar operator to cease debris data collection when repeated RFI contamination was observed. Now with the experimental 10.1 GHz waveform, instead of ceasing debris data collection all together, the radar operator switches waveforms and continues observing. The result of either procedure is the wideband RFI contamination mostly occurs on random days throughout the year at the end of datasets and appears as high rate “bursts” of RFI.

This RFI becomes easily identifiable in the dataset when range-rate is plotted as a function of time, usually day of year (DOY). Although OD detections can have range-rates in excess of ± 7 km/s in LEO, depending on the radar pointing, a significant number of these detections is unlikely since many debris objects have nearly circular orbits. Most detections for the primary observation geometry have range-rates in the ± 2 km/s range. The uniform distribution of range-rates of the RFI manifests as a vertical stripe in plots of range-rate versus time. Figure 3-9, in which range-rate has been plotted versus DOY for the 75E data, shows an example of such striping. Using this method, detections from files that are determined to contain RFI are removed from the detection list and the corresponding hours of observation are removed from the total number of hours observed.

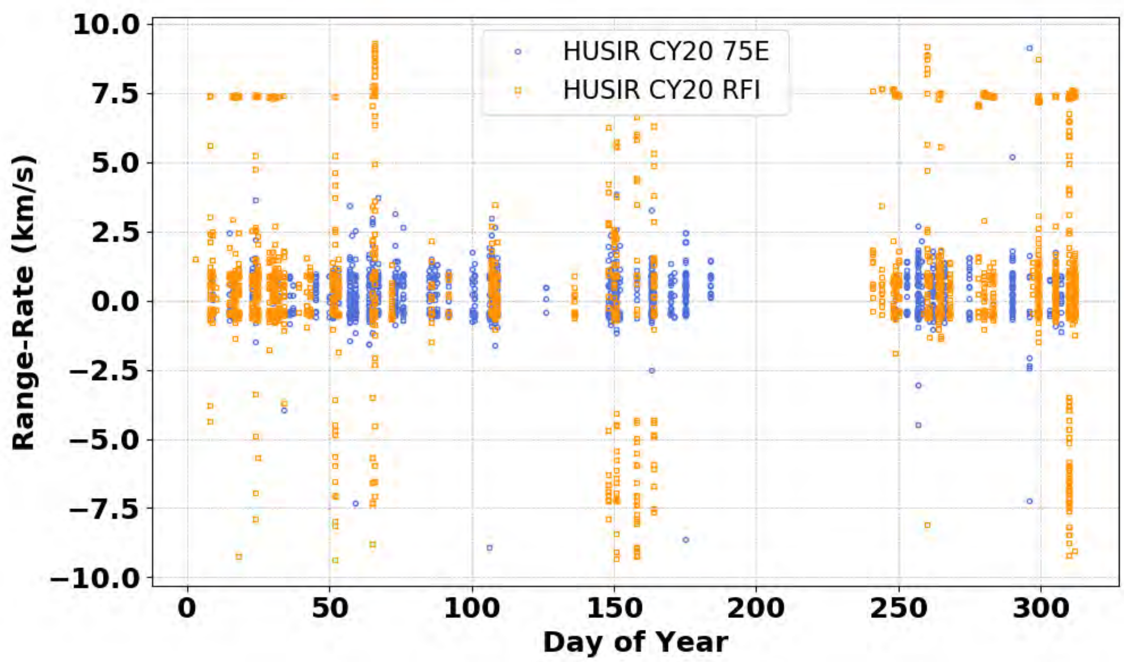

Figure 3-9. Range-rate versus DOY for CY2020 75E data taken at 10 GHz with wideband RFI identified.

3.5.2 RFI: Narrowband

Originally discovered during the processing of CY2018 data, a new type of RFI has become even more prevalent in the CY2020 data. This RFI persists across the entire range window at a single, fixed frequency. The RFI appears as a vertical stripe in plots of range versus range-rate because it occurs at one of a few discrete frequencies. The signal is typically present in every pulse within an affected file. After discussions with MIT/LL personnel, this new form of RFI is thought to be caused by electromagnetic coupling from other laboratory equipment at the radar site.

Since the observed SNR distribution for this type of RFI tends to be low (< 15 dB), the RFI signal is not always the highest SNR signal within a single pulse or group of pulses. This makes the narrowband RFI harder to detect in a range-rate versus DOY plot, since the range-rate of a detection group is pulled from the highest SNR pulse. Screening for this type of RFI involves plotting range versus range-rate for each pulse within the observation to discern the presence of a vertical striping feature. One such plot is shown in Figure 3-10, where the vertical stripe of magenta-purple data points near 7.5 km/s is clearly visible. Additionally, the count rate of 32.71 per hour is atypically high, another characteristic of observations affected by RFI. The average count rate measured at 75E in CY2020 was 19.57 per hour. The horizontal striping of gray points is an artifact related to the measurement of noise pulses at the beginning and end of detection groups. Since these points are invalid, they do not affect the measured quantities of valid debris detections.

Using this method to identify narrowband RFI, detections from files that are determined to contain RFI are removed from the detection list and the corresponding hours of observation are removed from the total number of hours observed.

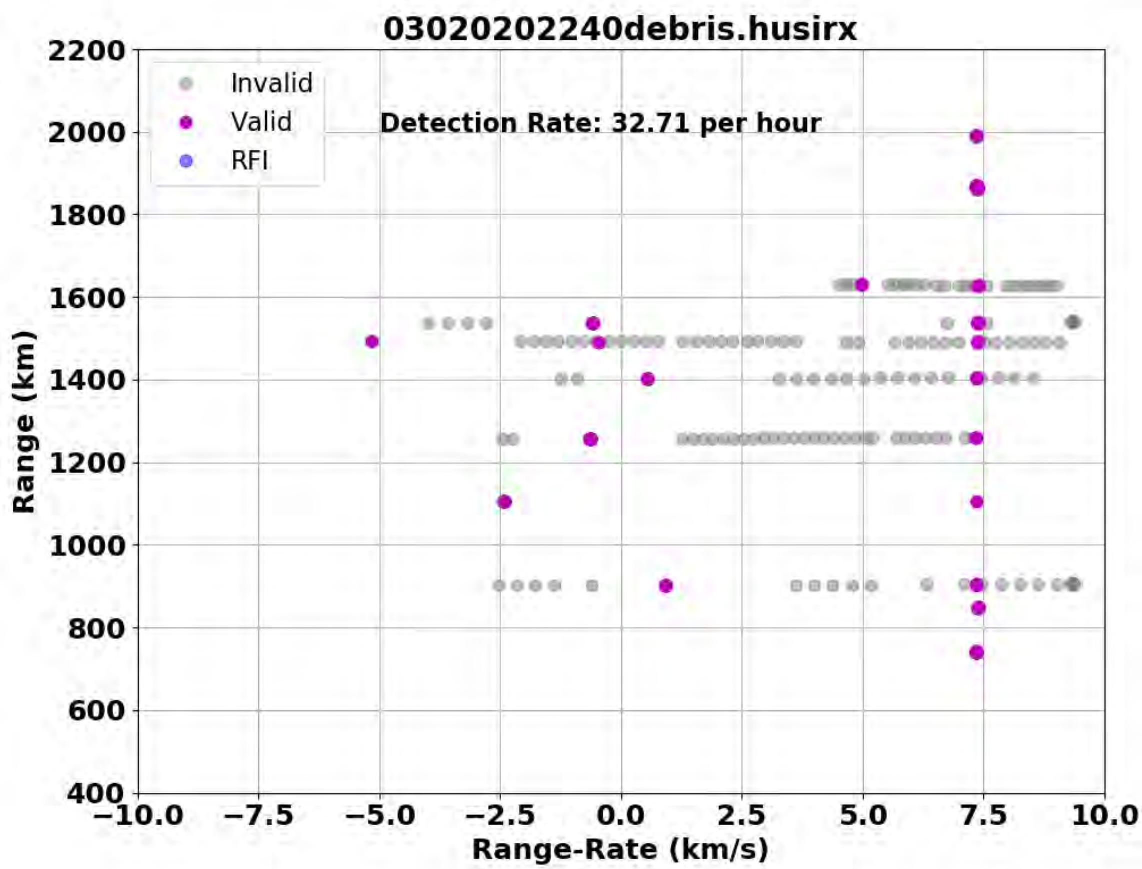

Figure 3-10. Example pulse-by-pulse range versus range-rate plot used for narrowband RFI identification. Note that "valid" indicates only that the measured SNR of the pulse was above the set threshold, not whether the pulse represents a debris object. Also note that while RFI is included in the legend, no pulses were identified as RFI by DRADIS in this file.

3.6 RADAR CALIBRATION USING NAK COOLANT DROPLETS

The NaK population of debris is an excellent OD radar calibration source shown to have stable count rates as far back as FY2000 [4] and exhibiting continued stability as recently as CY2019 [5, 6]. This liquid metallic coolant leaked from the ejected cores of the Soviet/Russian Radar Ocean Reconnaissance Satellites (RORSAT) and in microgravity, formed into spherical droplets under their own surface tension. Due to the low-velocity separation of these droplets from their parent bodies and the scattering properties of metallic spheres, this population can be separated easily from the rest of the OD population based on altitude, inclination, and polarization.

Figure 3-11 summarizes a model for the cumulative number of NaK particles as a function of the RCS at the HUSIR wavelength of 3 cm (10 GHz). This empirical RCS distribution is based on the work in [7]. The empirical RCS distribution exhibits an inflection point, the location of which is largely independent of the underlying size distribution model [7-9]. The location of the inflection point at –35 dBsm, indicated by the dashed black lines, is frequency dependent and is related to the RCS associated with the first peak in the Mie resonance regime. The presence of this inflection point at a value other than –35 dBsm is indicative of potential calibration issues including, but not limited to, data taken in the rain, hardware calibration errors or DSP timing offsets, and bad sphere-track calibrations. Although the empirical RCS distribution measured by the 10 GHz and 10.1 GHz waveforms in CY2020 is slightly different because of the different center frequencies, it is still close enough to be comparable. In fact, the difference in RCS between the first peak in the Mie resonance regime between 10 GHz and 10.1 GHz is only 0.086 dB, meaning the location of the inflection point is almost identical.

Figure 3-12 shows the measured RCS distribution of NaK in CY2020 75E data for both waveforms. While the expected inflection point can be seen, it is not as clearly visible as in previous years. Like CY2019, the number of hours for each waveform is low compared to CY2018 – which had a clearly visible inflection point. Due to the relatively large uncertainties in the count-rate for NaK at –35 dBsm, and the observed RCS values for objects transitioning between the lower- and higher-count-rate regimes straddling the reference calibration line, there is not sufficient evidence to indicate a calibration issue using the NaK population. We do, however, have a good comparison between the 10 GHz and 10.1 GHz waveform indicating the relative calibration between the two waveforms is consistent.

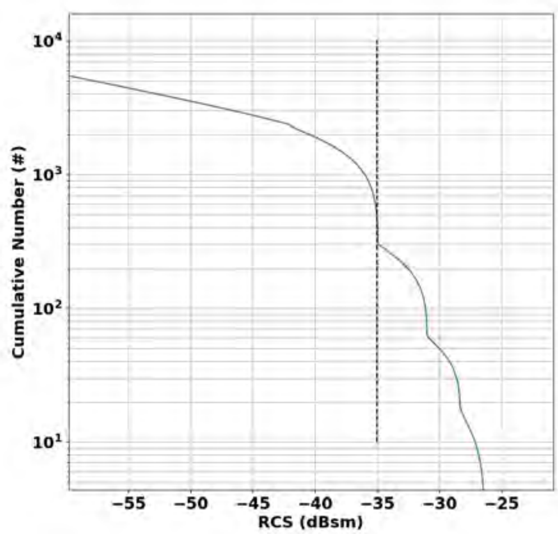

Figure 3-11. Empirical model of NaK RCS distribution.

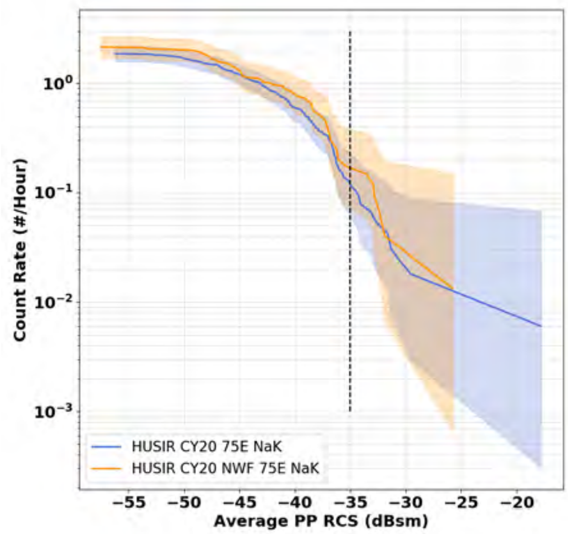

Figure 3-12. RCS distribution of NaK. The shaded regions represent the 2σ uncertainty bounds.

3.7 THE NASA SIZE ESTIMATION MODEL

Size estimates from radar data sources are reported using the NASA SEM, which relates the RCS of debris objects from the measured PP and OP channels, and a wavelength, to an empirically derived characteristic length. The SEM originated from an early 1990's study led by XonTech that utilized representative debris objects taken from two U.S. Department of Defense hypervelocity impact tests of satellites conducted at the Arnold Engineering Development Complex [1, 9, 10]. In addition to the representative objects from the impact tests, several debris-like objects were included in the sample to better represent the postulated debris environment at the time. The RCS values for the 39 debris objects were measured at an RCS radar range operated by the System Planning Corporation. RCS measurements of these objects were taken over four commonly used radar frequency bands (S band: 2.5647–3.9111 GHz; C band: 4.116–7.986 GHz; X band: 8.1544–12.7684 GHz; and Ku band: 12.924–17.538 GHz), with 8 frequency samples taken in the lowest frequency band and 16 frequency samples taken in the remaining three frequency bands. These radar frequency bands correspond to the frequency bands in use by OD radars. Measurements were taken from multiple, different orientations of the debris objects to understand the distribution of possible RCS values that each piece of debris would present to a radar as the tumbling debris passes through the radar beam [11-13].

The characteristic length is the average of the projected dimensions, or the dimensions along the shadow of a debris object. ODPO defines *x* as the longest projection dimension, *y* as the longest shadow dimension perpendicular to *x*, and *z* as the longest projection dimension orthogonal to both *x* and *y* [14]. As shown in Figure 3-13, the first axis was chosen to coincide with the largest dimension, the second axis to coincide with the largest dimension in a plane orthogonal to the first axis, and the third axis to be orthogonal to the plane defined by the first two axes. The characteristic length of an object is referred to interchangeably as size or diameter.

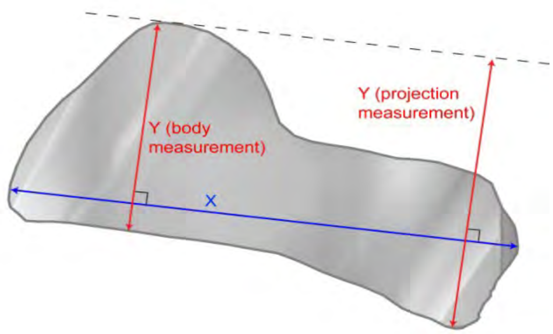

Figure 3-13. Illustration of body and projected measurement on complex shape used in determining characteristic length.

Radar data from sensors operating with different wavelengths may be compared by scaling the size by the wavelength, λ, of the measurement frequency and the RCS by the square of the wavelength. This results in a normalized size, diameter/ λ, and a normalized RCS, RCS/ λ^2. Combining all the measurements – different frequency and object orientations – onto a single plot results in the normalized RCS vs. normalized size shown in Figure 3-14. Each of the 2072 data points on this plot is a weighted average for a single debris object over the hundreds of different orientations at a single frequency. The data were weighted to account for the non-uniform sampling of the object orientations as the data were collected.

From the plot shown in Figure 3-14, a scaling curve – the solid black line – was developed, which is the mean of the measured RCS for each normalized size. The solid blue line shows the theoretical RCS for a sphere as a function of size. For debris sizes much smaller or larger than the radar wavelength, the scaling curve approaches the same result as the Rayleigh or optics regions, respectively, for the sphere. Between these two regimes is the Mie resonance region, where for the case of the sphere, there exists a one-to-many mapping between a given RCS value and the size of the sphere. In the case of the size estimation model; however, there is a one-to-one relationship between a given RCS and the size of the object, as shown in Figure 3-14.

For additional details on the piecewise function definition of the SEM or scaling curve from Figure 3-14, see [15].

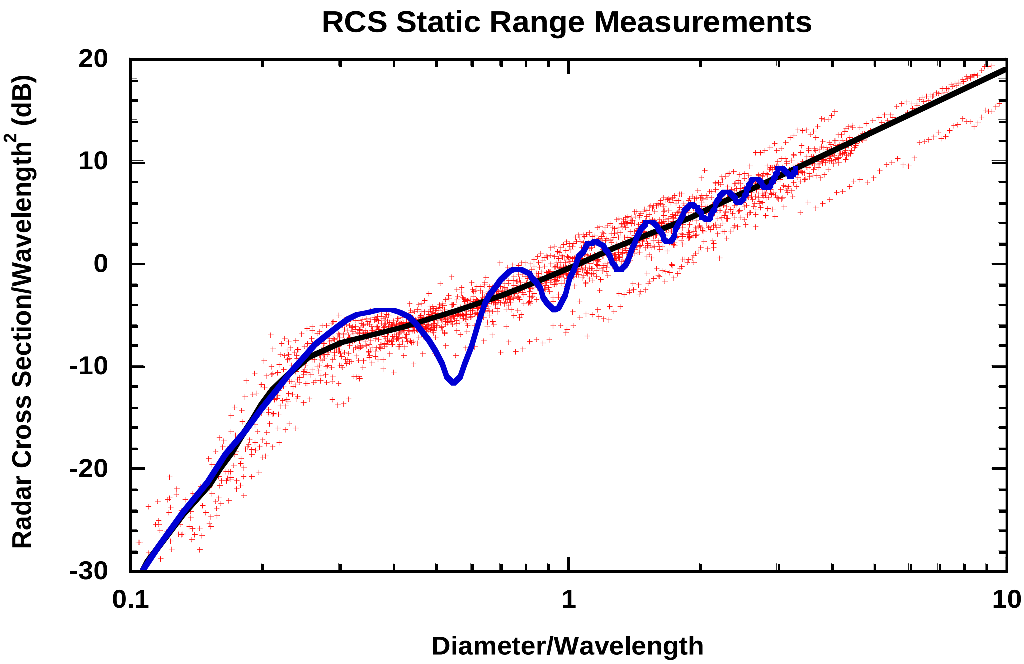

Figure 3-14. Results of RCS-to-size measurements on 39 representative debris objects.
The oscillating line is the RCS for a spherical conductor
while the smooth line is the polynomial fit to the data.

4.0 Results

4.1 DATA COLLECTION OVERVIEW

Most data in CY2020 was collected at 75E. The 75E pointing provides enough Doppler discrimination to estimate some orbital parameters of the detected debris objects, such as inclination calculated by using a circular orbit approximation. In this configuration, detected objects are in orbits with inclinations approximately equal to or greater than the latitude of the radar. Observations were also performed at 10S and 20S. Although the lower-elevation pointing geometries increase the slant range for a given altitude, which reduces sensitivity, it allows the radar to measure debris in orbits as low as 20° inclination. Table 4-1 shows the minimum and maximum observable ranges and corresponding orbital altitudes for each observation geometry.

Table 4-1. Minimum and Maximum Observable Ranges and Corresponding Orbital Altitudes for Observation Geometry

Pointing	Minimum Range	Maximum Range	Minimum Orbital Altitude	Maximum Orbital Altitude
75° East	415 km	2232 km	392 km	2166 km
20° South	835 km	2654 km	325 km	1321 km
10° South	1255 km	3074 km	327 km	1168 km

Table 4-2 shows the number of observation hours at 75E, 20S, and 10S pointings and the total number of detections in each configuration. Observation hours represent the total number of hours remaining after the removal of observation windows that were determined to be contaminated with RFI. The number of detections represents the total number of events for which there were three or more pulses with a single-pulse SNR greater than 5.65 dB, where at least one is in the two-way, 6-dB beamwidth (one-way, two-sided 3-dB beamwidth). A table showing the total number of hours received from MIT/LL is provided in Appendix A.

Table 4-2: Data Collection Summary Reflecting the Final Curated Data Set

Waveform	75° East		20° South		10° South	
	Hours of Observation	Number of Detections	Hours of Observation	Number of Detections	Hours of Observation	Number of Detections
10.0 GHz	82.9	1599	44.3	559	39.0	230
10.1 GHz	37.4	755	17.7	240	16.0	117

4.2 RADAR MEASUREMENTS

Most observations performed in CY2020 were taken using the 75E pointing. In this configuration, radar measurements of the OD environment are obtained with a range window from 415 km to 2232 km. This corresponds to orbit altitudes between 392 km and 2166 km.

This section uses the 75E data as an example to represent the types of information available in the dataset. A comprehensive set of plots for all observation geometries and waveforms are presented in Appendices C through H. There, range versus range-rate, range versus RCS, altitude versus inclination, cumulative SEM size distributions, cumulative PP SNR distributions, cumulative RCS distributions, and polarization distributions are presented for each pointing direction. Additionally, cumulative surface area flux versus altitude and inclination are presented for the 75E pointing.

4.2.1 Range Versus Range-Rate

Two of the fundamental measurements made by the radar are range and range-rate. Range is the distance from the radar to the target and is calculated from the time it takes the transmitted signal to travel to and return from the target. Range-rate is a measurement of the velocity component of the target along a line connecting the radar to the target and is calculated from the Doppler shift of the received signal. Figure 4-1 presents the range plotted against the range-rate for the 75E data from 2020, with the 10.1 GHz overlaid on the 10 GHz data. Although detections with range-rates as high as ± 7 km/s are present in the data, most detected objects in the 75E pointing have range-rates between ± 2 km/s, as seen in Figure 4-1. Note that the plot is limited to ± 4 km/s.

A horizontal feature can be seen along the bottom of the figure at a range of 415 km. This corresponds to the bottom edge of the range window for 75E. Since this represents the lowest measurable range, any reflections from objects that are slightly below the range window will have a measured range of 415 km. When comparing the 10.1 GHz data to the 10 GHz data, we see the same clusters of points corresponding to the various debris families, indicating comparable measurements between waveforms.

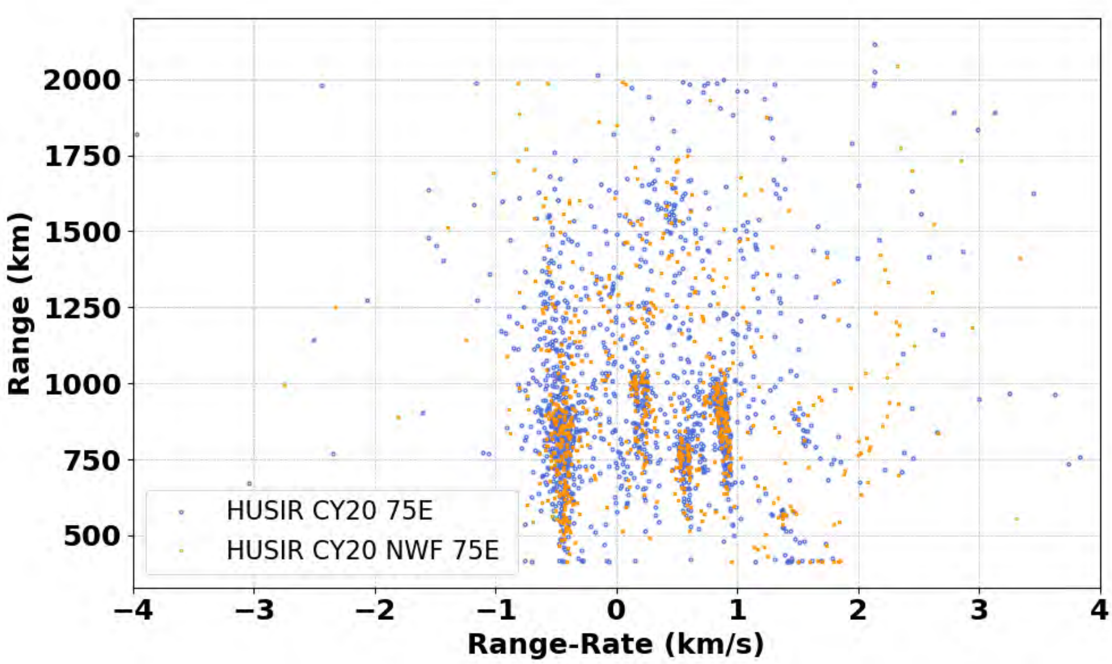

Figure 4-1. Range versus range-rate for the HUSIR 75E data from 2020.

4.2.2 Altitude Versus Inclination

One can estimate an object's inclination and orbital altitude, with a circular orbit approximation, using measurements of range and range-rate. All presentations of inclination in this report, unless otherwise indicated, are calculated in this way, and are referred to as Doppler inclinations. The 75E observation geometry has been the preferred observation geometry used by the NASA ODPO for many years because it represents a good compromise between having sufficient Doppler discrimination to estimate Doppler inclination valid to within a degree, for near circular orbits, while minimizing loss of sensitivity at a given altitude that occurs for lower-elevation observations [4]. Figure 4-2 shows the altitude versus Doppler inclination for the HUSIR 75E data from 2020, with the 10.1 GHz overlaid on the 10 GHz data. When represented in this way, distinct families of debris can be isolated and studied independently. Again, we see comparable results between the two waveforms used.

Of interest in CY2020 are two new clusters that appear at about 53° inclination: one at 550 km altitude and the other at 392 km, the altitude corresponding to the lower-range window limit. Note that Doppler inclination estimates for detections at or below the range window limit will exhibit some spread due to error in the measured range. A second fragmentation of a *Fregat* upper stage debris object, previously identified in the catalog as "SL-23 DEB," (International Designator 2011-037B) occurred near this inclination in 2020. Additionally, this is the operational inclination of the Space Exploration Technologies Corp. (SpaceX) Starlink satellite constellation, with an operational altitude of 550 km. Starlink satellites also have a "parking orbit" after launch of about 350 km, which may manifest as 392 km in the data due to HUSIR's range window. The relative contributions of these two factors is discussed in section 4.4.

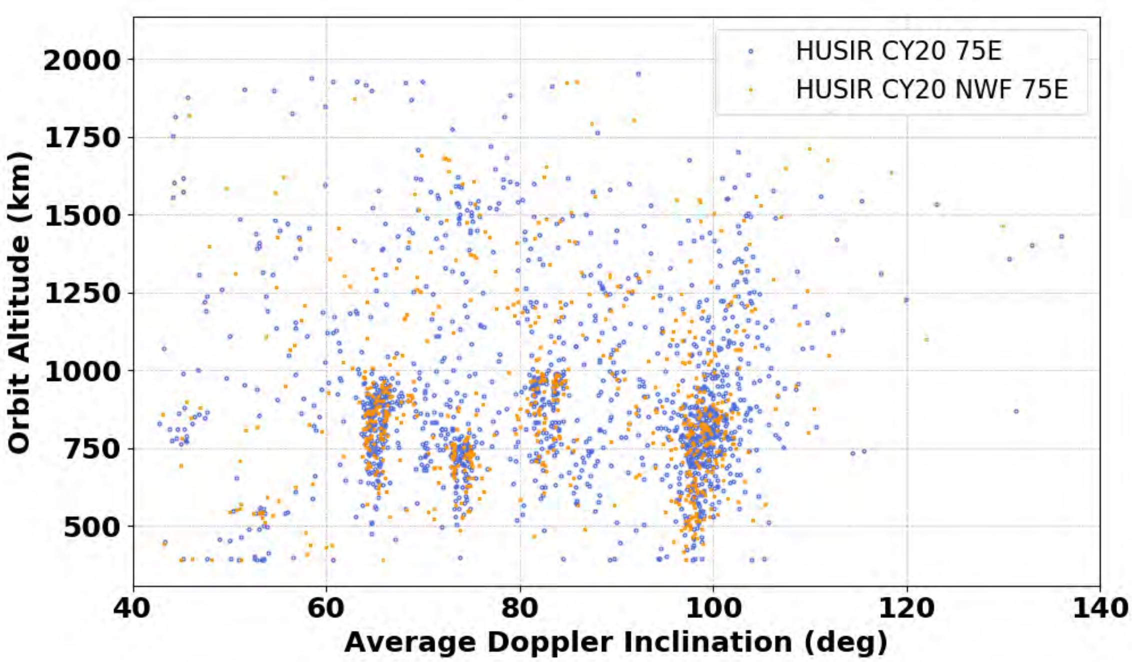

Figure 4-2. Altitude versus Doppler inclination for the HUSIR 75E data from 2020.

4.2.3 Range Versus Total RCS

Another key measurement made by the radar, in addition to range and range-rate, is that of RCS. Figure 4-3 shows the range versus total RCS for the HUSIR 75E data in 2020, with the 10.1 GHz overlaid on the 10 GHz data. Additionally, a black dashed line is shown that represents the theoretical RCS of an object with a single-pulse SNR of 5.65 dB as a function of range. This curve is calculated using the average sensitivity of HUSIR for 2020. Although the RCS of the same object measured by these two waveforms is slightly different because of the different center frequency, it is still close enough to be comparable, less than 0.2 dB difference in the Rayleigh scattering region. Figure 4-4 shows the corresponding orbit altitude versus SEM size plot with the corresponding single-pulse SNR curve in this space. Using SEM size provides a better comparison between the 10 GHz and 10.1 GHz data since it accounts for the slight difference in frequency. Alternately, normalizing the RCS by the square of the wavelength could be used as well.

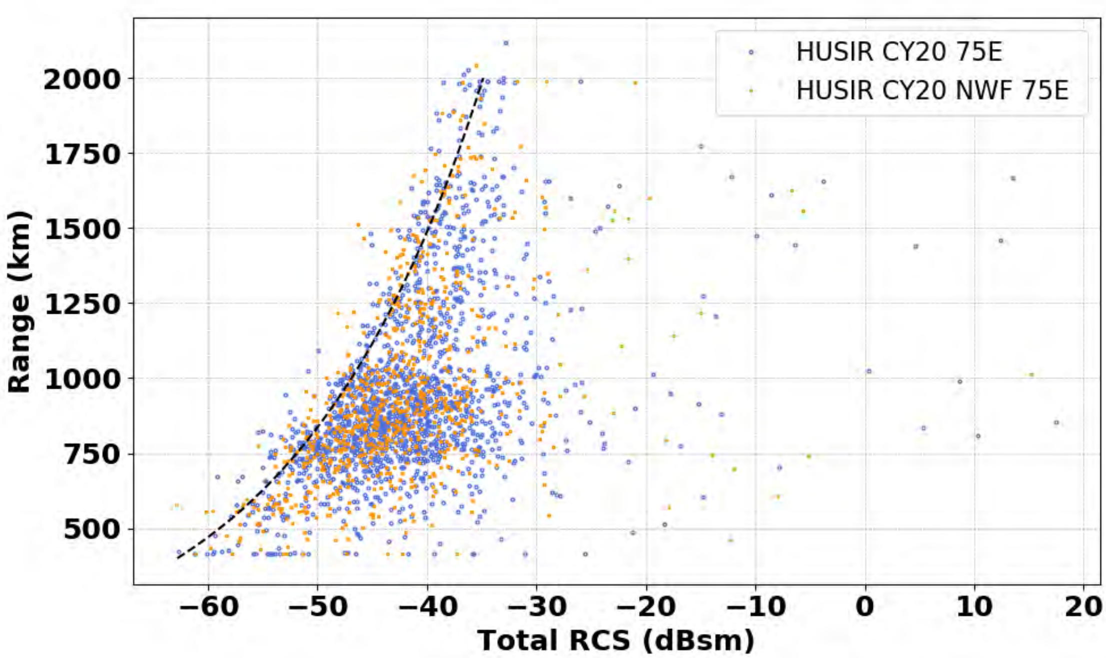

Figure 4-3. Range versus total RCS for the HUSIR 75E data from 2020.

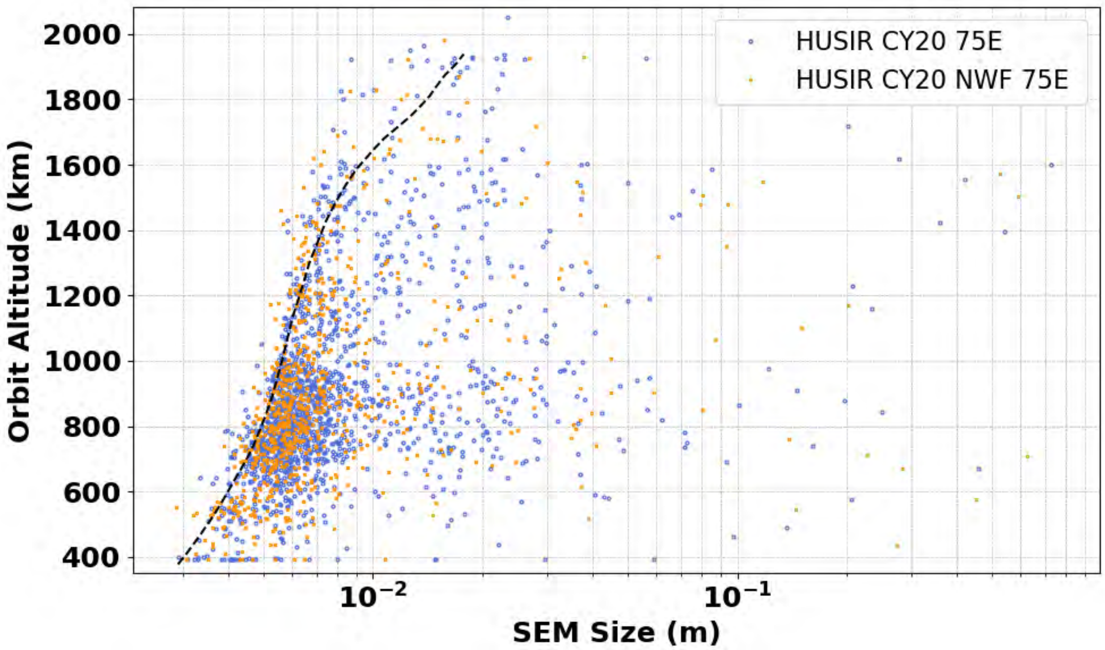

Figure 4-4. Orbit altitude versus SEM size for the HUSIR 75E data from 2020.

4.2.4 Polarization Distribution

The HUSIR radar transmits right-hand, circularly-polarized waveforms and receives both PP- and OP-channel radar returns. The polarization (P) is defined as:

$$P = \frac{RCS_{PP} - RCS_{OP}}{RCS_{PP} + RCS_{OP}}$$

By this definition, the polarization of a perfectly conducting sphere would be + 1. A perfect dipole would have a polarization of zero. Figure 4-5 shows the polarization distribution of the CY2020 75E data for both waveforms. Since the radar sensitivity is different for each waveform, the polarization distribution is presented down to a limiting size of 5.62 mm and under 1000 km altitude to obtain comparable results.

As was seen in previous years, the 10 GHz polarization distribution is approximately flat from 0 to 0.75. The 10.1 GHz distribution exhibits more variation in this region, although the uncertainties overlap for many of the polarization bins – indicating no statistical difference for the respective bins. The prevalence of sphere-like populations such as NaK causes the distribution to increase from 0.75 and peak at + 1, although the peak for the 10.1 GHz waveform is sharper. This may be related to the extra sensitivity of the 10.1 GHz data, as sensitivity differences has been known to shift the location of this polarization peak. Since the theoretical OP RCS for metallic spherical objects is zero, when measurements are performed on the OP channel it is a measurement of the OP channel noise floor (for lower SNR detections), some value above zero. A radar with higher sensitivity will have a lower noise floor and thus measure a higher polarization for the same sized sphere. As the sensitivity of a radar decreases, the polarization distribution of a family of spheres will spread out.

Below zero, the polarization distribution begins to fall off quickly. Since the detection scheme employed by the MIT/LL ROSA hardware performs detection using the PP channel, there may be a population of debris with higher OP signatures that remains undetected unless their PP signature is sufficiently strong. The largest difference between the two waveforms is in this region, specifically from - 0.3 to + 0.2, where the 10.1 GHz count rate is significantly lower than the 10 GHz count rate. This may be due to the low number of hours for the 10.1 GHz waveform, as there are no detections with a polarization less than - 0.7 in this dataset. It should be noted that with the count rates and number of hours for the 10 GHz, there are about four detections or less in the lower polarization bins, and one detection is within the uncertainties. Since there is less than half the hours with the 10.1 GHz data set, it is not too surprising that no objects with these polarizations were seen.

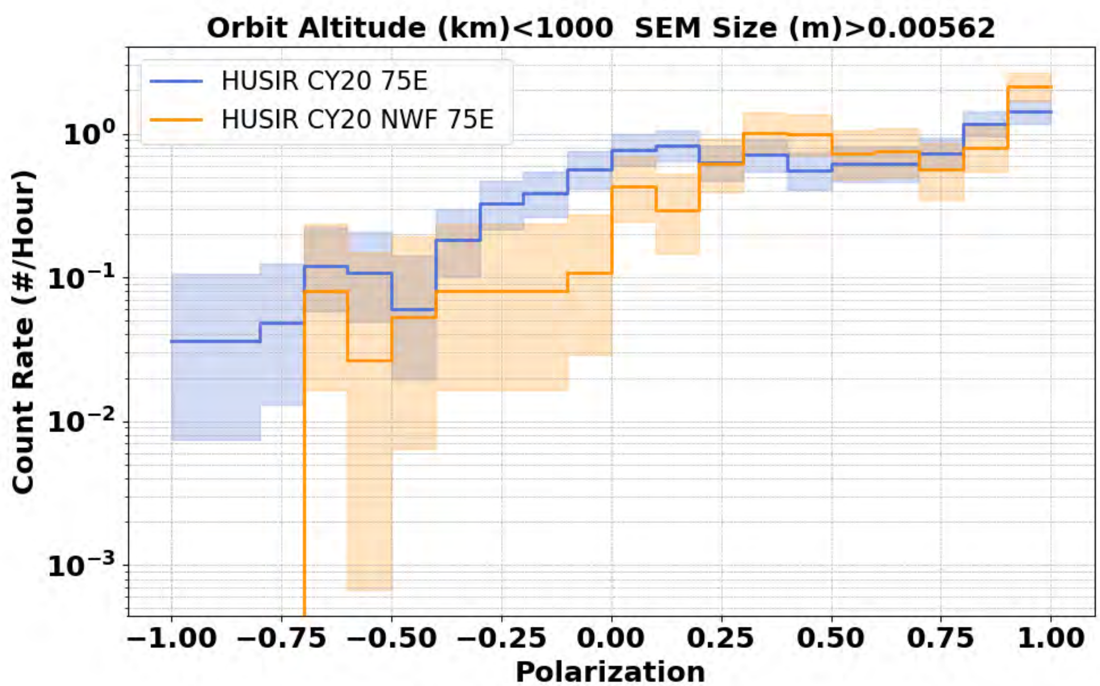

Figure 4-5. Polarization distribution for the HUSIR 75E data from 2020, limited to 5.62 mm and 1000 km altitude. The shaded regions represent the 2σ uncertainty bounds.

4.2.5 Comparison of Derived Parameters for Cataloged Objects

When collecting data in beam park mode, some objects that have been cataloged by the SSN pass through the HUSIR field of view. By correlating detections to the SSN catalog, comparisons between the catalog-derived parameters and the HUSIR-derived parameters can be made to help validate measurement results. It must be noted, however, that measurements made to maintain the SSN catalog are performed with different sensors for different purposes. The SSN focuses on obtaining accurate measurements of position and velocity that can be used for orbit determination, with less interest in the actual size of the objects. For OD measurements, the HUSIR data is being used statistically to characterize the debris environment and the exact size or complete orbital elements of an individual object is not critical so long as the distribution of sizes or orbits is representative of the environment.

To correlate detections to the SSN catalog, a two-stage approach is used; a preliminary correlation stage and a second stage, which gathers additional statistics on the preliminary correlation using multiple TLEs. The first stage reviews each detection and checks for a correlation with each object in the SSN catalog. It pulls the closest two-line element set (TLE) in time to the detection for each object, propagates the TLE to the time of detection, and computes the predicted range, range-rate, azimuth offset, and elevation offset expected at that time. If the difference in the TLE-predicted values relative to the measured values are within a certain tolerance, a correlation is declared. The tolerances used for CY2020 were ± 2 km in range, ± 200 m/s in range-rate, and ± 2° in azimuth and elevation.

In the second stage, each candidate correlation identified in the first stage is reviewed using all available TLEs for the object in a ± 5-day period. To account for potential timing errors, the TLEs are propagated to the time of closest approach to the boresight of the radar, as predicted by the individual TLE, rather than the time of detection measured by the radar. Once all TLEs have been propagated to their respective times of closest approach, statistics on the minimum, maximum, and mean predicted parameters are gathered. Within the detection list are fields to indicate whether the correlation was within the uncertainties in azimuth, elevation, range, and range-rate that are added as part of the second-stage of the correlation process.

Comparisons of the HUSIR-derived size and SSN-reported size for HUSIR 75E detections collected in CY2020, which correlate to cataloged objects, are shown in Figure 4-6 and Figure 4-7. The main lobe detections roughly follow the one-to-one dashed line, indicating a general agreement in measured sizes. Three additional lines that correspond to the first (- 41 dB), second (- 49 dB), and third (- 55 dB) sidelobes of HUSIR also are shown in Figure 4-6. The measured RCS from different sensors can vary based on the aspect angle presented to the radar at the time of measurement and the RCS history measured by the SSN. In general, if a detection is near the one-to-one line, it is well above the sidelobe levels and classified as a main lobe detection. For main lobe detections, the two data sources agree for larger objects. For small objects, sizes calculated by HUSIR with the 10 GHz waveform are smaller than those calculated by the SSN. This is consistent with previous results in [4] where it was concluded that SSN sensors, specifically the Eglin radar (AN/FPS-85), overestimate the size of smaller debris fragments due to the way in which the average RCS from multiple pulses is calculated. This effect is less prominent in the 10.1 GHz catalog comparisons but is likely due to having relatively fewer datapoints.

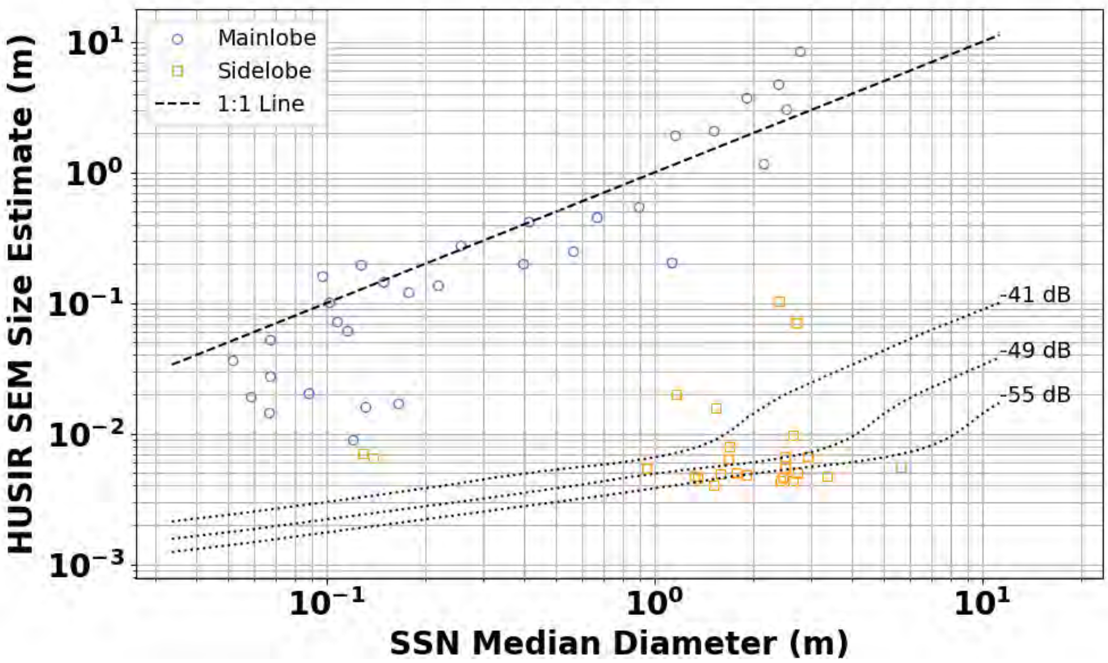

Figure 4-6. Comparison of the HUSIR-derived size and SSN-reported size HUSIR 75E detections collected in CY2020 with the 10 GHz waveform that correlate to cataloged objects.

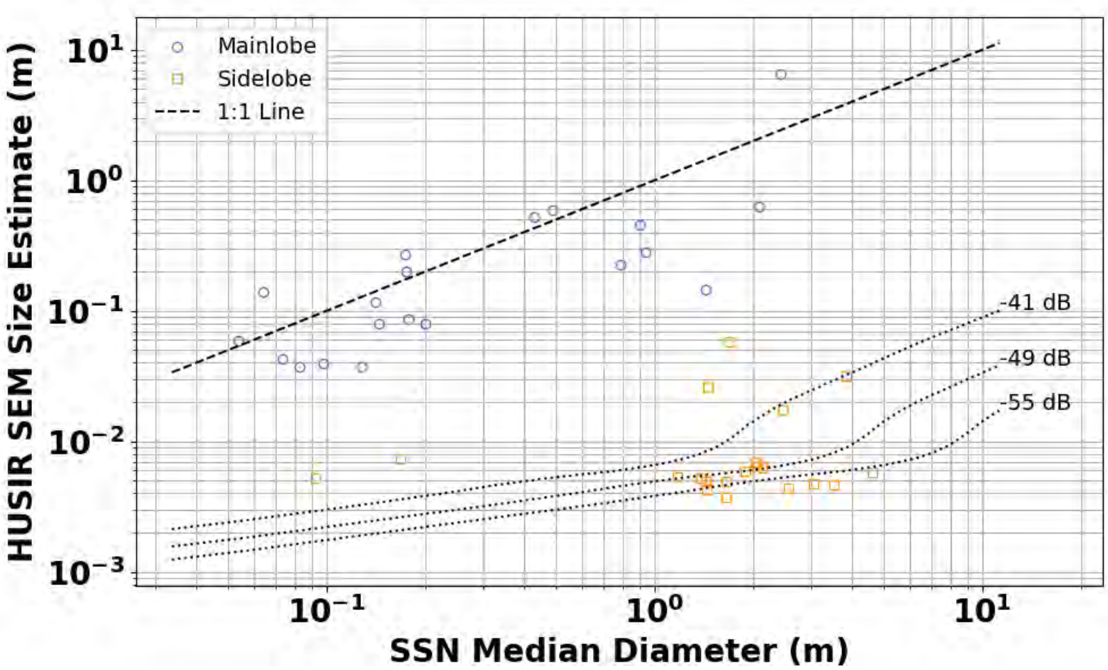

Figure 4-7. Comparison of the HUSIR-derived size and SSN-reported size HUSIR 75E detections collected in CY2020 with the 10.1 GHz waveform that correlate to cataloged objects.

Figure 4-8 compares the Doppler inclination derived from HUSIR data of main lobe detections, both waveforms, with the cataloged inclination for correlated targets in the CY2020 75E data. Most points lie on or near the dashed line that represents a one-to-one match of the SSN catalog inclination values and the Doppler inclination values. Figure 4-9 compares the Doppler inclination derived from HUSIR data with the Doppler inclination for correlated targets calculated from the TLE-predicted range and range-rate. The latter technique of comparing the two datasets using Doppler inclination is a better method for analysis purposes. In this instance, there is only one point where the two results do not agree, showing that most of the difference observed in Figure 4-8 is likely due to the Doppler inclination calculation, *i.e.*, approximating the objects as having a circular orbit. The TLE-predicted range and range-rate represent averages of these values as predicted from multiple TLEs. Occasionally, one or more TLEs produce estimates that are out of family with the majority. This can be either real and related to changes in the orbit of the object, or just the result of a poor measurement. The latter can be identified as a deviation from the trend of previous TLEs, which is then corrected by subsequent TLEs. When these out-of-family predictions occur, they skew the average, which can result in large deviations of the SSN Doppler Inclination from the HUSIR Doppler Inclination, like the outlier seen in Figure 4-9. It is of interest to incorporate some form of outlier rejection in the multi-TLE prediction process to prevent these out-of-family predictions when possible.

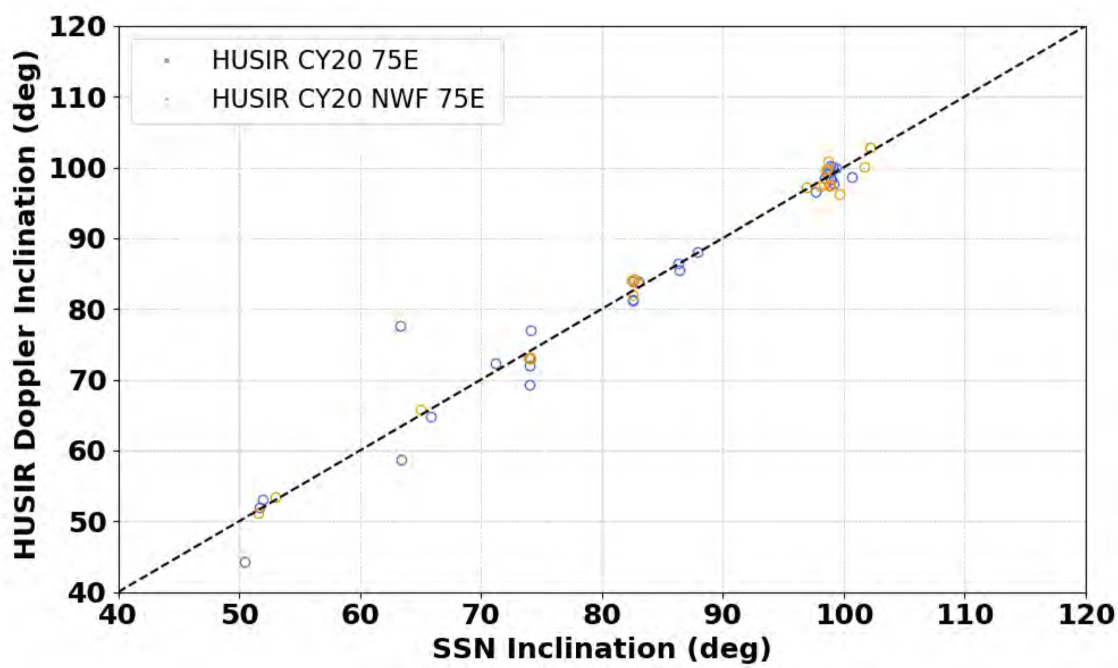

Figure 4-8. Comparison of the Doppler inclination derived from HUSIR data with the cataloged inclination for correlated targets in the CY2020 75E data.

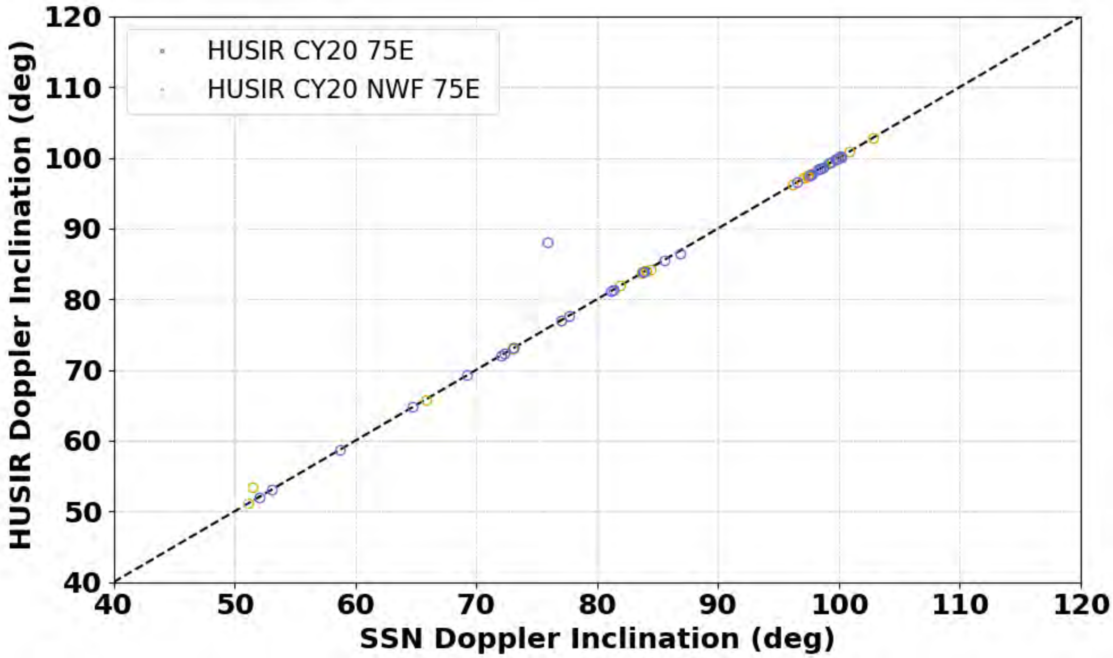

Figure 4-9. Comparison of the Doppler inclination derived from HUSIR data with the Doppler inclination for correlated targets calculated from the TLE-predicted range and range-rate.

4.3 ENVIRONMENT CHARACTERIZATION SUMMARY

The radar data presented here is meant to provide a broad overview of the state of the debris environment in low Earth orbit. Since the radar sensitivity changes from year-to-year, flux charts presented in this section, which compare many years of data, are typically presented with the cumulative flux down to a limiting size and an upper bound on altitude. Each subsection will first compare the CY2020, 10 GHz data to previous years of data to identify new features in the data or environment. Then the 10.1 GHz data will be compared to the 10 GHz data to verify that comparable results were obtained.

4.3.1 SEM-size Cumulative Distribution

While total count rate of debris can change each year due to changes in radar sensitivity, the distributions of these measured sizes should remain largely the same. Any large changes from year-to-year are indicative of a significant change in the OD environment.

Figure 4-10 compares the cumulative size distributions for the CY2018, CY2019, and CY2020 10 GHz 75E datasets. The shaded regions represent the 2σ-Poisson uncertainties. Cumulative count rates are comparable across all datasets down to a limiting size. The CY2018 and CY2019 distributions roll off sooner than the CY2020 datasets at smaller sizes. This is because HUSIR was operating at a higher power, on average, than in the previous two years. Between 1 cm and 2 cm, the CY2020 distribution is slightly elevated, although still within the confidence intervals.

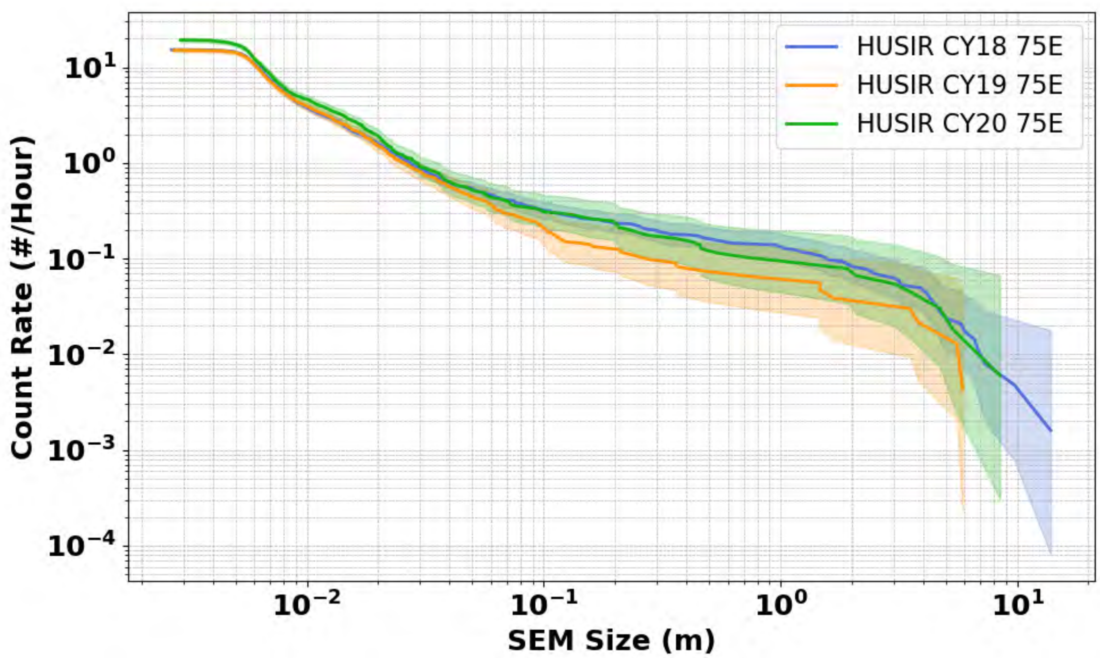

Figure 4-10. SEM-size cumulative distribution for all 10 GHz, 75E data, by year.

Figure 4-11 compares the cumulative size distributions for the CY2020, 10 GHz and 10.1 GHz, 75E datasets. The shaded regions represent the 2σ-Poisson uncertainties. The cumulative count rate between the two waveforms is within confidence intervals at all sizes. Of interest is the 10.1 GHz distribution more closely matches the prior years' data in the previously mentioned 1 cm to 2 cm region.

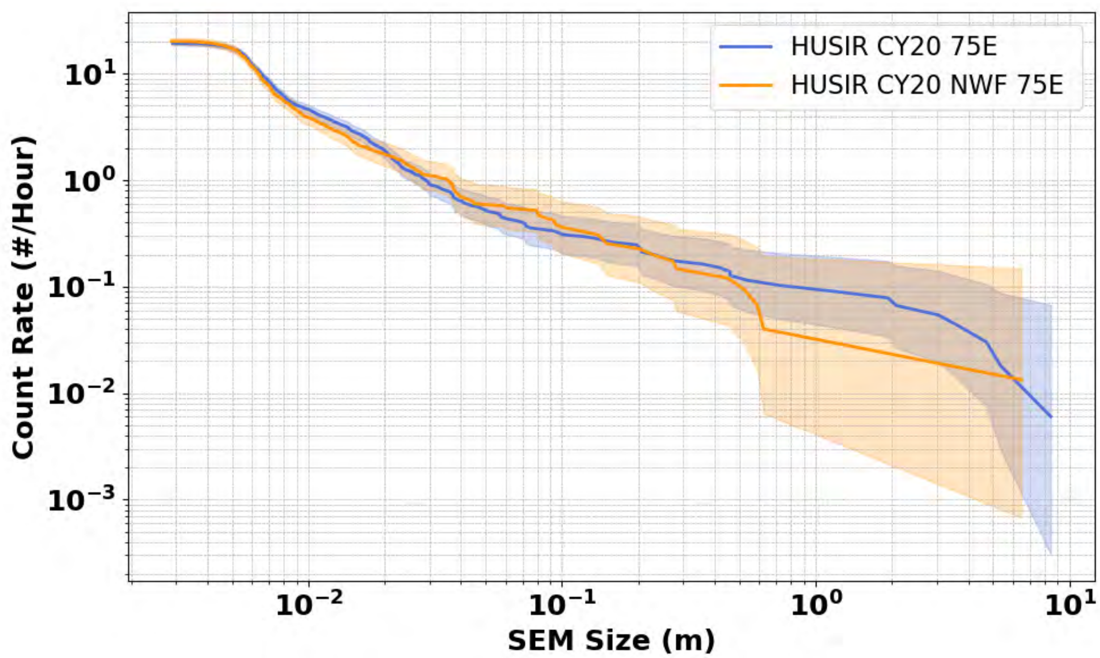

Figure 4-11. SEM-size cumulative distribution for all CY2020, 75E data.

4.3.2 Flux Versus Altitude

Flux is defined as the number of detections through the lateral surface area of the radar beam, considering the 3 dB beamwidth of the main beam only, within a given period. Total flux is the flux of all objects regardless of size, where size is estimated using the NASA SEM, as described in Section 3.7. To aid in comparing different years, cumulative flux to a limiting size is shown. This represents the flux of objects with a size equal to or greater than the chosen limiting size. For all years, cumulative flux is presented to limiting sizes of 5.62 mm and 1 cm, depending upon altitude.

It should be noted that during the analysis of the CY2019 data, a large, low-altitude flux increase was observed, which was determined to be correlated to the Anti-Satellite (ASAT) test performed against the Microsat-R satellite in CY2019. Methods developed in [5] were used to remove detections correlated to this fragmentation event from the rest of the CY2019 data. The CY2019 data presented in this report represents the dataset excised of Microsat-R fragment detections. This allows for a better comparison to previous years in the low altitude regime.

Figure 4-12 shows the cumulative flux versus altitude limited to 1 cm for all 10 GHz, 75E observations, by year. The shaded regions represent the 2σ-Poisson uncertainties. We see generally good agreement between the different years. There is a slight increase from 1150 km to 1250 km, which may be related to the fragmentation of the METEOR 3-5 rocket body (R/B), SSN catalog number 21656, in a 1172 km × 1210 km, 82.6° inclination orbit on

12 February 2020. Analysis in Section 4.4 has shown the May 2020 fragmentation of SL-23 DEB to be another likely candidate.

Figure 4-13 shows the cumulative flux versus altitude limited to 5.62 mm for all 10 GHz, 75E observations, by year. We see a slight increase from 550 km to 600 km and from 700 km to 750 km. These increases are also present in the flux limited to 1 cm-SEM sizes and larger. SpaceX has deployed 833 Starlink satellites to 550 km altitude, 53° inclination orbits in CY2020, making the constellation a possible source candidate for the 550 km to 600 km flux increase. There were three correlations to Starlink satellites in the data, all of which were around 550 km in altitude. It is possible that more Starlink satellites were detected, but due to the way the orbits of these satellites are raised, the actual orbits may have deviated from the TLE predictions sufficiently to prevent TLE correlation.

An interesting feature to note is the absence of the low altitude flux increase seen in the CY2019 data that was shown likely to be caused by the Microsat-R ASAT test. It should be noted that even with detections flagged as correlated to Microsat-R removed, the CY2019 flux still is slightly elevated in some altitude bins relative to CY2018 and CY2020. Possible explanations for this, previously presented, included residual Microsat-R fragments that were not flagged during the identification process or debris related to the ORBCOMM FM-16 fragmentation, which occurred in CY2019. Except for the 550 km to 600 km altitude bin, the low altitude flux has returned to nominal levels measured in CY2018, indicating that the effects of the ASAT test on the small particle environment in LEO was only short term.

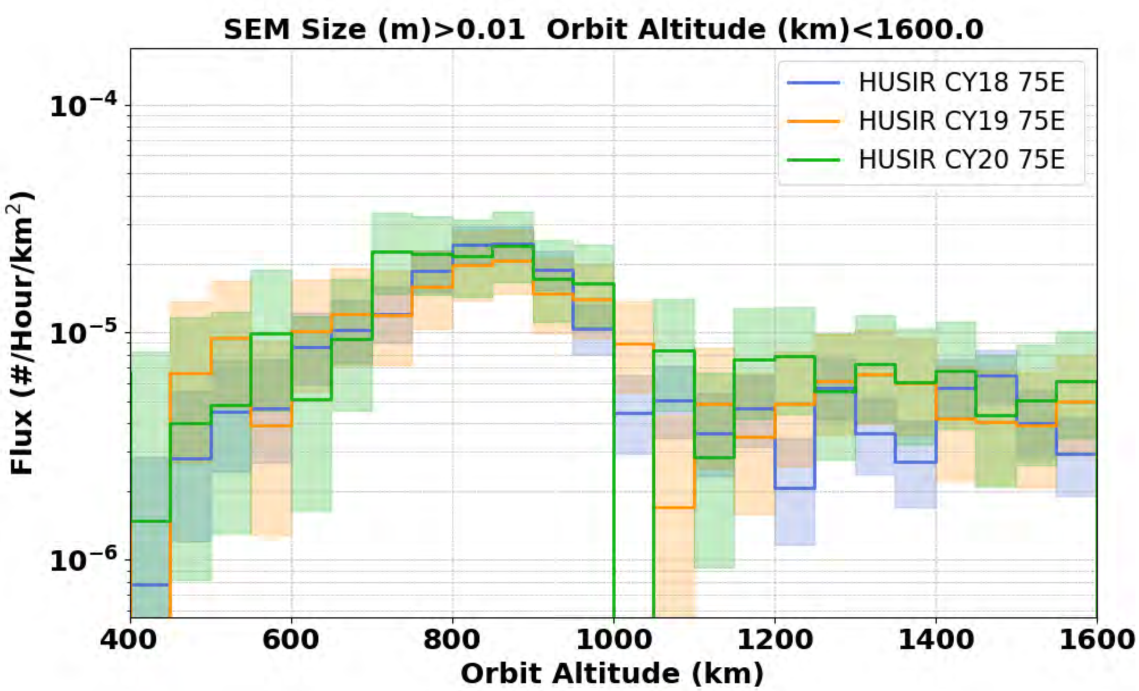

Figure 4-12. Cumulative surface area flux versus altitude limited to 1 cm for all 10 GHz, 75E data, by year.
The shaded regions represent the 2σ uncertainty bounds.

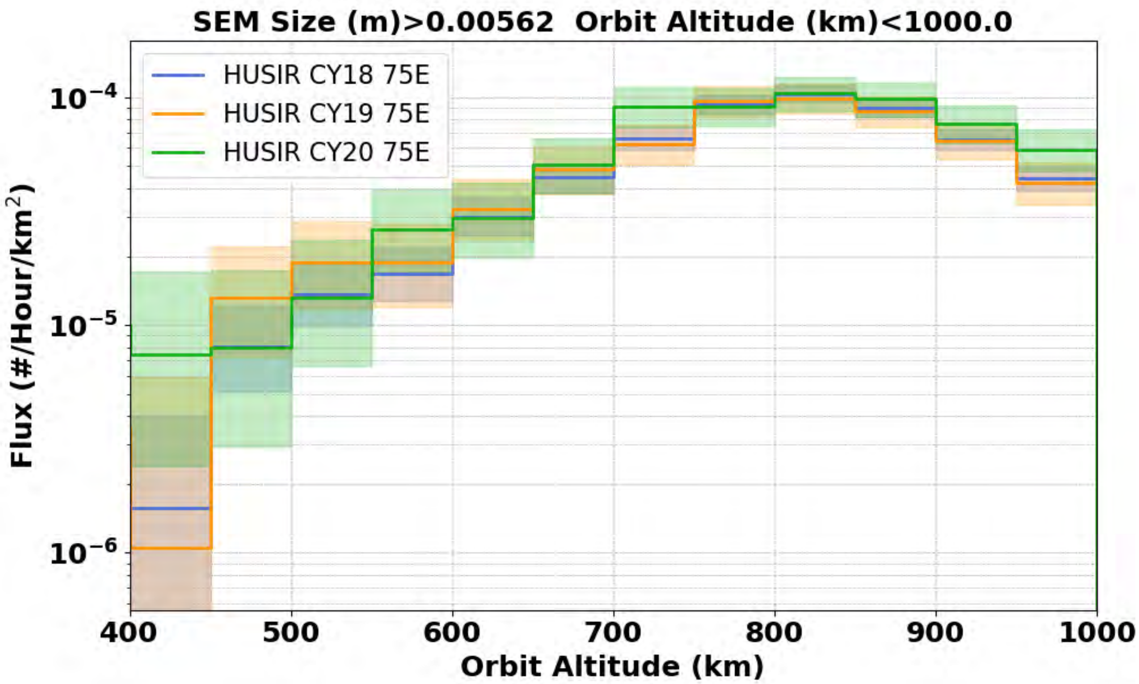

Figure 4-13. Cumulative surface area flux versus altitude limited to 5.62 mm for all 10 GHz, 75E data, by year.
The shaded regions represent the 2σ uncertainty bounds.

Figure 4-14 shows the cumulative flux versus altitude, limited to 1 cm for the 10 GHz and 10.1 GHz, 75E observations. The confidence intervals of the CY2020, 10.1 GHz data are large, due to the low number of hours. In fact, no detections of objects greater than 1 cm were made between 450 km and 500 km or between 1200 km and 1250 km. No detections were made for objects 1 cm and larger for the 10 GHz data for altitudes between 1000 km and 1050 km. Measurements made with both waveforms are within their respective confidence intervals at all other altitudes.

Figure 4-15 shows the cumulative flux versus altitude limited to 5.62 mm for the 10 GHz and 10.1 GHz, 75E observations. With a smaller size filter, the number of detections is larger, allowing for reduced uncertainties and a better comparison. Except for a slightly higher 500 km to 550 km altitude bin, we see good agreement between waveforms. It is possible that some 10.1 GHz observations were taken close to the time of an on-orbit event, whose count rate when measured would have a strong time dependence until the values of right ascension of the ascending node (RAAN) have randomized. Another possibility is that observations were taken near the time of a large deployment of satellites or during the orbit raising process, in which Starlink satellites slowly raise the altitude of their orbits in a linear fashion from the 350 km parking orbit to the 550 km-altitude operational orbit.

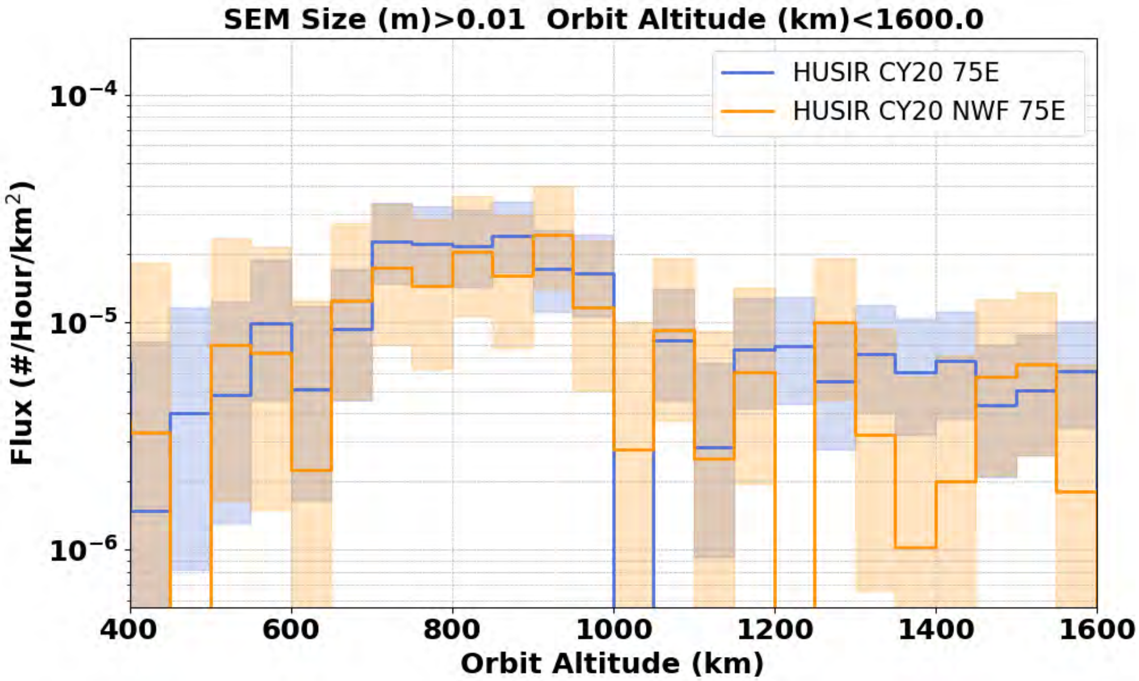

Figure 4-14. Cumulative surface area flux versus altitude limited to 1 cm for all CY2020, 75E data. The shaded regions represent the 2σ uncertainty bounds.

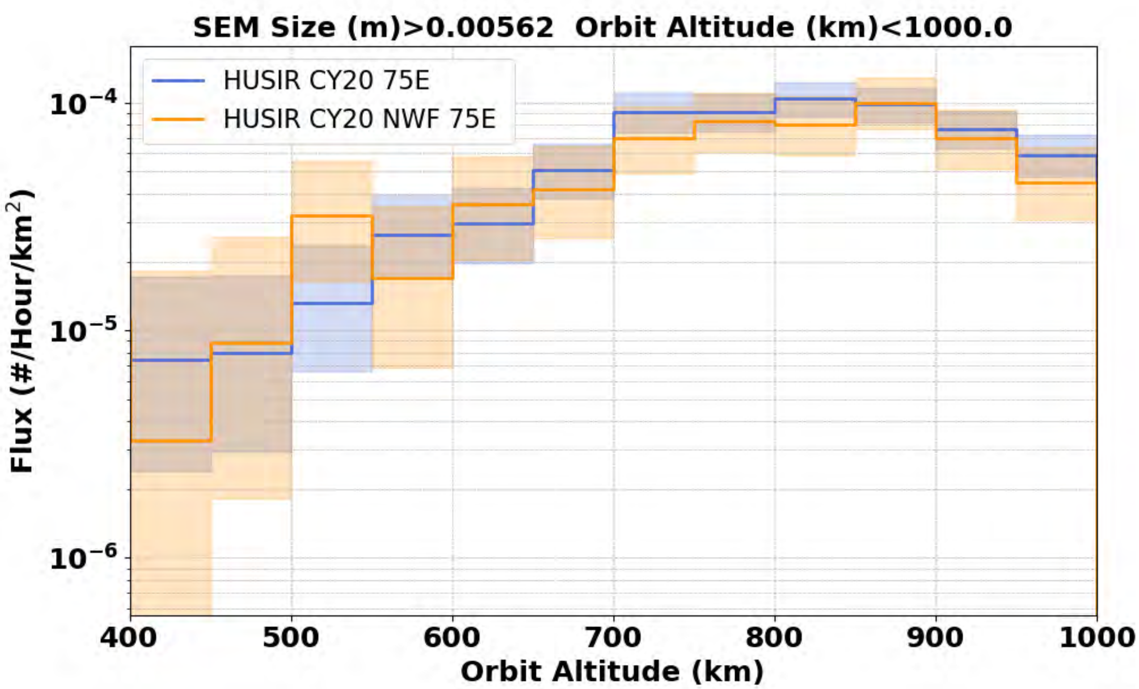

Figure 4-15. Cumulative surface area flux versus altitude limited to 5.62 mm for all CY2020, 75E data.The shaded regions represent the 2σ uncertainty bounds.

4.3.3 Flux Versus Inclination

In addition to flux versus altitude, examining flux versus inclination gives more insight to the distinct populations/families of debris. Flux is defined in the same fashion as in previous sections, except that the beam area is the total surface area of the beam from the minimum observable altitude to the maximum observable altitude since each altitude bin can measure debris at all inclinations observable to the radar in the 75E geometry. The fluxes presented in this section are to limiting sizes of 5.62 mm and 1 cm and will use 2°-sized bins.

Figure 4-16 shows cumulative surface area flux versus inclination limited to 1 cm for all 10 GHz, 75E data, by year. There is general agreement between the years. Of interest is the persistence of an increase seen in the 44° to 46° bin originating in CY2019, with the flux in CY2020 exceeding that of CY2019 for sizes limited to 1 cm and larger. The persistence of this increase is consistent with a candidate parent body proposed in [5], ORBCOMM FM-16, SSN catalog number 25417. On 22 December 2018, the ORBCOMM FM-16 spacecraft experienced a debris generating event in a 783 × 782 km, 45° orbit [16]. At this altitude, the orbits of these fragments would decay slowly, potentially staying on orbit for decades [17].

Figure 4-17 shows cumulative surface area flux versus inclination limited to 5.62 mm for all 10 GHz, 75E data, by year. There is an increase from 72° to 76° inclination that has been determined to be related to the 700 km to 750 km altitude flux increase identified in Section 4.3.2. There is also an increase from 88° to 90° inclination that has been determined to be related to the 550 km to 600 km-altitude flux increase. Although space traffic related to Starlink satellites has increased the flux in this latter altitude bin, the 88° to 90° inclination flux increase is the major contributor to the flux increase in the 550 km- to 600 km-bin. It is interesting to note, when limiting the flux to SEM sizes 5.62 mm and larger, the flux in the 44° to 46° inclination bins for CY2020 and CY2019 HUSIR data are indistinguishable.

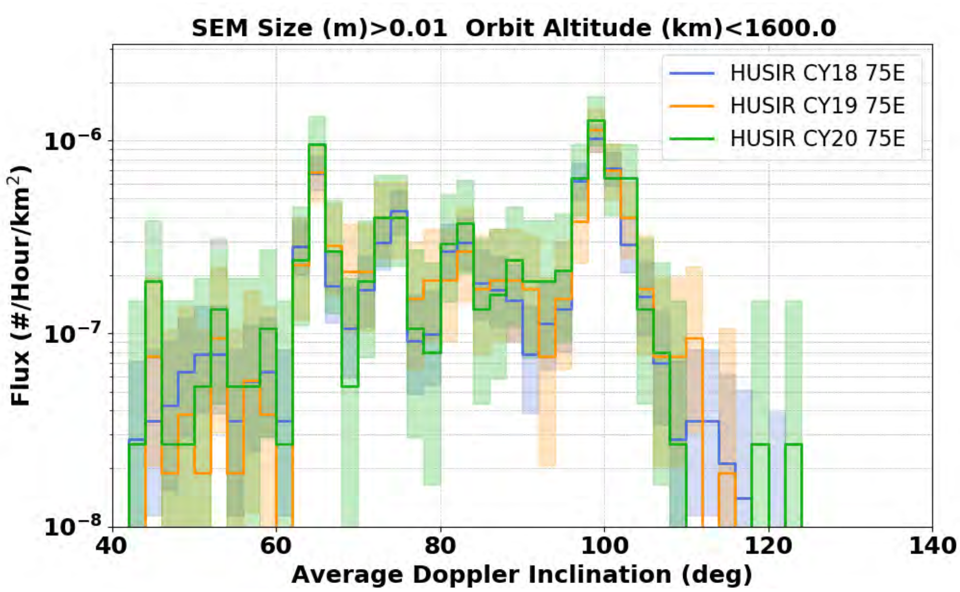

Figure 4-16. Cumulative surface area flux versus inclination limited to 1 cm for all 10 GHz, 75E data, by year.
The shaded regions represent the 2σ uncertainty bounds.

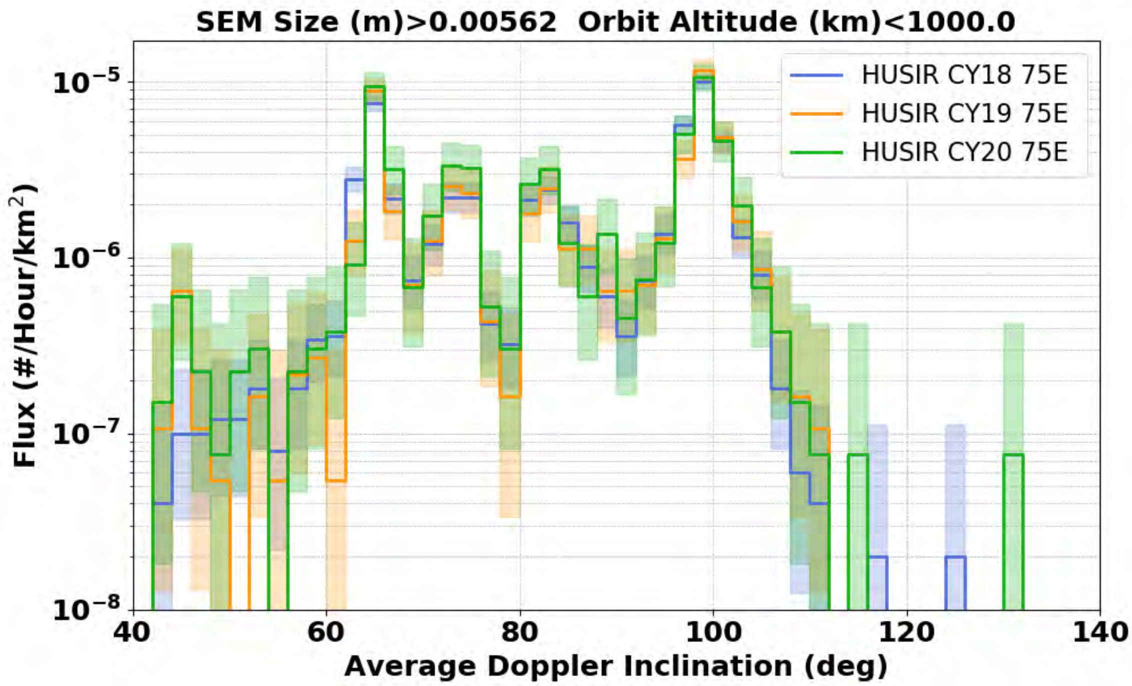

Figure 4-17. Cumulative surface area flux versus inclination limited to 5.62 mm for all 10 GHz, 75E data, by year.
The shaded regions represent the 2σ uncertainty bounds.

Figure 4-18 shows cumulative surface area flux versus inclination limited to SEM sizes 1 cm and larger for all CY2020, 75E data. Due to the low number of observation hours in these datasets, there are several inclination bins for which there were no detections. For all bins with data, there is a good comparison between the 10 GHz and 10.1 GHz data – within the uncertainties between the datasets. Figure 4-19 shows cumulative surface area flux versus inclination limited to SEM sizes 5.62 mm and larger for all CY2020, 75E data. Again, there is good agreement between data taken with the two different waveforms. To within the counting uncertainties, analysis thus far has shown that the 10 GHz data and 10.1 GHz data produce comparable results.

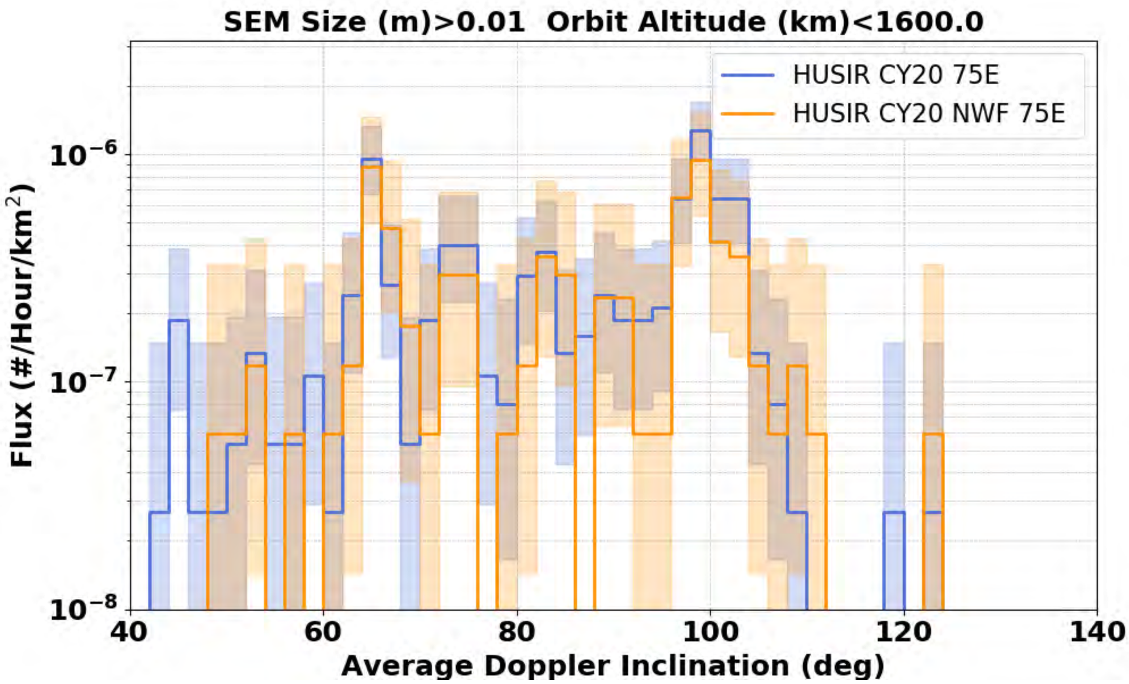

Figure 4-18. Cumulative surface area flux versus inclination limited to 1 cm for all CY2020, 75E data.The shaded regions represent the 2σ uncertainty bounds.

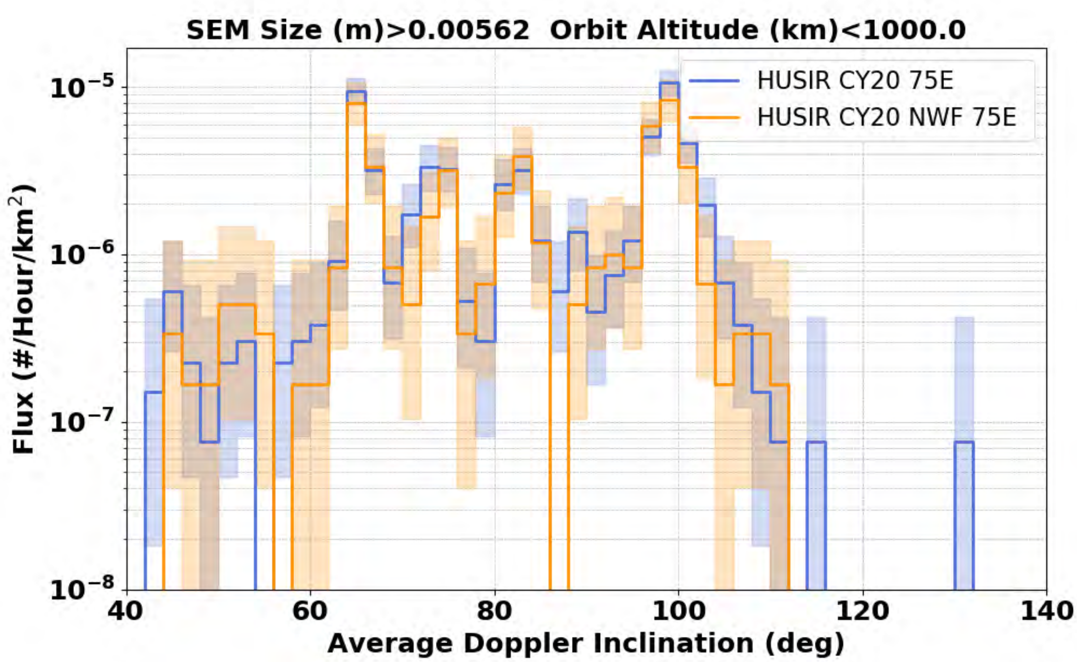

Figure 4-19. Cumulative surface area flux versus inclination limited to 5.62 mm for all CY2020, 75E data.The shaded regions represent the 2σ uncertainty bounds.

4.4 BREAKUP IDENTIFICATION

To better understand the source of measured flux increases, it is useful to examine debris-generating events that occurred near or during the timeframe of the data collected and analyzed in this report. In CY2020 there were 5 known breakups that collectively resulted in a total of 692 cataloged objects, of which 548 remain on orbit as of 6 February 2022. Table 4-3 shows all known breakups that occurred during CY2020. Of the 5 breakups in CY2020, SL-23 DEB has the most objects related to the parent body, with 334 objects cataloged. As of 6 February 2022, with 293 objects, debris related to SL-23 DEB constitutes the eighth largest cloud of cataloged objects still on orbit.

Table 4-3. All Known Breakups that Occurred in CY2020, as of 6 February 2022

SATELLITE NAME	BREAKUP DATE	APOGEE (KM)	PERIGEE (KM)	INCLINATION (DEG)	DEBRIS CATALOGED
COSMOS 2535	9-Jan-20	645	607	97.9	18
METEOR 3-5 R/B	12-Feb-20	1206	1186	82.56	112
SL-23 DEB	8-May-20	3606	422	51.5	334*
H-2A DEB	12-Jul-20	643	595	97.9	87
RESURS O1	27-Aug-20	660	633	97.9	141
*This includes only fragments from the second fragmentation event.					

In CY2019, a low-altitude flux increase prompted development of an improved method to correlate HUSIR detections to a breakup cloud. This is done by simulating a model cloud using NASA's Standard Satellite Breakup Model (SSBM). The SSBM is described in detail in [18]. Once generated, the resulting modeled fragments are propagated to the HUSIR observation window times to determine the range/range-rate distribution of the modeled cloud, and whether there were cloud observation opportunities for HUSIR during those time windows. To correlate HUSIR detections with the modeled clouds, the density-based, spatial clustering of applications with noise (DBSCAN) [19, 20] clustering algorithm is employed and applied to a combination of the modeled cloud and HUSIR data. HUSIR detections that are clustered with the modeled cloud data by the clustering algorithm are flagged as being correlated to the breakup. Additional details of this process can be found in Section 4.4.1 of [5].

This method was used to successfully identify fragments correlated to the ASAT test against Microsat-R, and to show that these correlated detections were the source of the low-altitude flux increase seen in CY2019 HUSIR data. Due to the number of generated fragments, the inclination, and the eccentricity of the SL-23 DEB fragmentation, it is of interest to perform a similar analysis for this breakup in CY2020.

4.4.1 SL-23 DEB

On 8 May 2020 between 0402 Greenwich Mean Time (GMT) and 0551 GMT, a debris object identified as SL-23 DEB, associated with the launch of Russia's *Spektr-R* radio astronomy satellite, experienced a second fragmentation [21]. The object had experienced a prior breakup event in August 2015. The causes of both fragmentation events are unknown. At the time of the second event, the parent body was in a 3606 km × 422 km altitude, 51.5° inclination orbit. The maximum change in inclination was 0.21°. A total of 24 fragments were initially tracked from the first fragmentation, but none were confirmed or entered the catalog at that time. A total of 334 objects related to the second SL-23 DEB fragmentation have been cataloged, with 293 remaining on orbit as of 6 February 2022.

Unfortunately, a precise breakup time for the May 2020 event is not currently available. Furthermore, the breakup time window is on the order of the period of the orbit of the parent body, meaning the breakup could have happened at any point within the orbit. As an initial investigation into the effect of the true anomaly of the breakup on the resulting range and range-rate distribution that HUSIR may have observed, four clouds were modeled using the SSBM with the fragmentation occurring at true anomalies of 0°, 90°, 180°, and 270°. The generated fragments were then propagated to the HUSIR CY2020 observation windows to determine the range and range-rate distribution of the modeled cloud, and whether there were observation opportunities for HUSIR during those time windows. Propagation was performed using a long-term, orbital element propagator that includes Sun-Moon, J2, J3, J4 and drag perturbations. Figure 4-20 shows the range and range-rate distributions of each of the modeled clouds, with HUSIR 10 GHz and 10.1 GHz data overlaid on each. This figure shows that the location of the breakup in true anomaly has a significant effect on the structure of the resulting cloud. Note that the range window of HUSIR extends only to 2232 km. While the fragments of the modeled cloud extend in excess of 6000 km in range, HUSIR would only measure the portion of the cloud below 2232 km.

Uncertainty in the breakup time complicates the correlation of HUSIR detections on a DOY-by-DOY basis, as was done with Microsat-R in CY2019. As an example, Figure 4-21 shows the modeled clouds and HUSIR data limited to observations made on DOY 266 and within the HUSIR range window. Attempting to identify HUSIR detections that are clustered with the modeled cloud for correlation purposes would produce vastly different results for each of the four clouds shown.

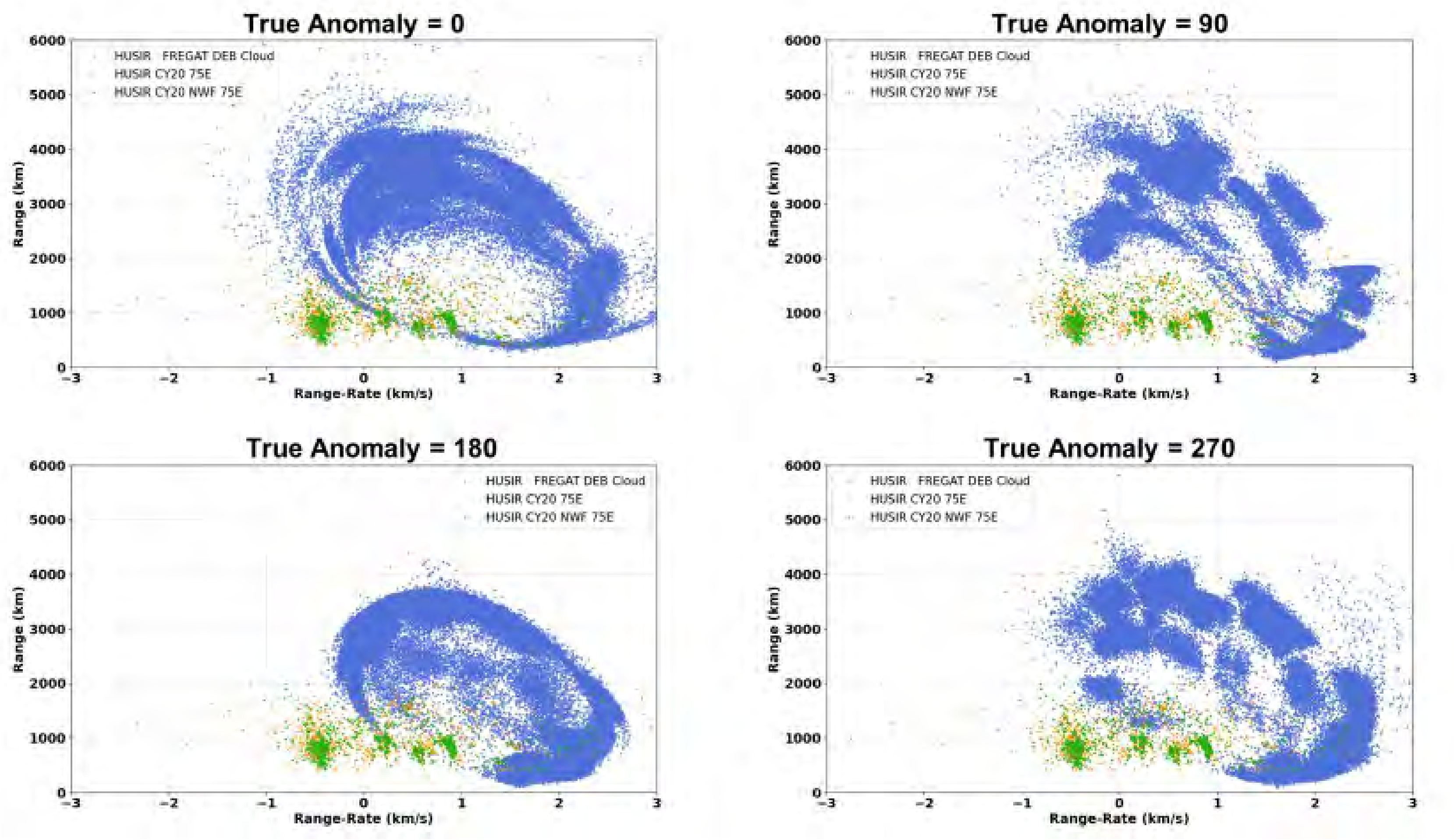

Figure 4-20. Modeled SL-23 DEB (*Fregat*) cloud in range/range-rate space comparing the effect of true anomaly at the time of the breakup on cloud distribution.
HUSIR 10 GHz and 10.1 GHz data is overlaid on each cloud.

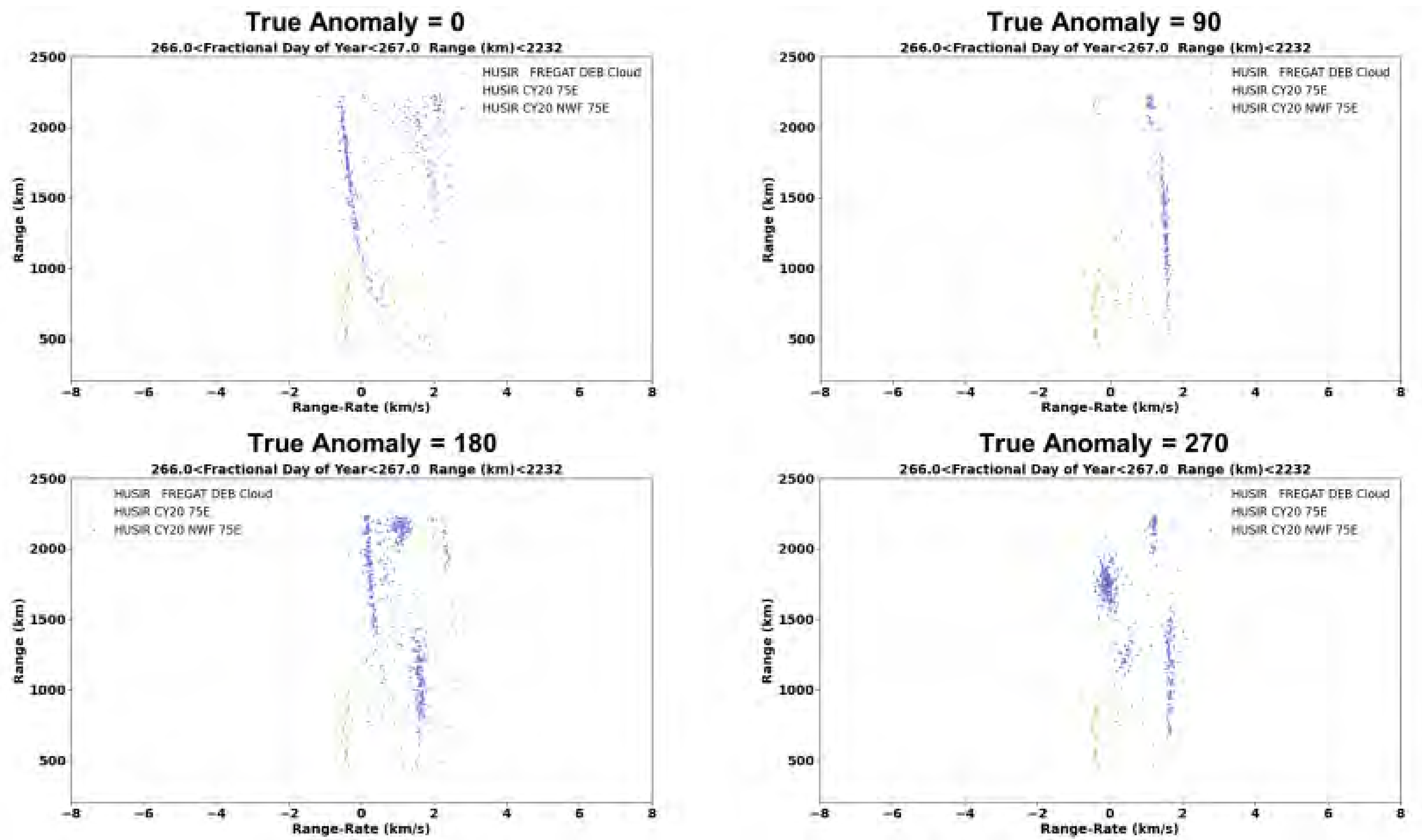

Figure 4-21. Modeled SL-23 DEB (*Fregat*) cloud in range/range-rate space comparing the effect of true anomaly at the time of the breakup on cloud distribution.
HUSIR 10 GHz and 10.1 GHz data is overlaid on each cloud. Data and cloud are limited to DOY 266 observations.

To flag individual detections like was done for Microsat-R, a better estimate of the time of breakup is needed. Future work on determining the breakup time of the event will focus on propagating a set of cataloged fragments and the parent body backwards in time to find the time that minimizes the miss distance between them. A similar technique is used by the United States Space Force's 18th Space Control Squadron using a spacecraft conjunction assessment software and is described in [22].

Although individual HUSIR detections are unable to be correlated with the SL-23 DEB cloud at this time, further analysis of the modeled clouds at additional true anomalies does provide insight into the altitude and inclination regions affected by the cloud. To understand the possible contributions of the cloud to the OD flux in different altitude and inclination regions, modeled clouds were generated for true anomalies ranging from 0° to 360° in five degree increments, resulting in 74 different clouds. Although the cloud shapes in range and range-rate are all very different, when one examines the resulting altitude and inclination flux distributions of the clouds, similarities are present for all values of true anomaly. Figure 4-22 shows the count density, essentially flux without time, for all 74 modeled clouds. The top row shows the count density versus altitude and Doppler inclination for all fragments in each of the clouds. The bottom row shows the count density versus altitude and Doppler inclination limited to the range window of HUSIR and the corresponding sensitivity of 2 cm at that range. Note that although the horizontal axis of the total count density versus altitude only extends to the range window of HUSIR for clarity, the total count density versus Doppler inclination contains all modeled fragments including those above the range window.

Although not labeled for specific values of true anomaly, the family of curves shows the expected range of count density values in each of the altitude and inclination bins. The count density versus altitude charts shows that independent of true anomaly for the breakup, there are peaks at 400 km to 450 km, 500 km to 600 km, 1100 km to 1200 km, and 1700 km to 1800 km. These altitude regions were the same ones previously identified as having increased flux in the HUSIR observations for CY2020.

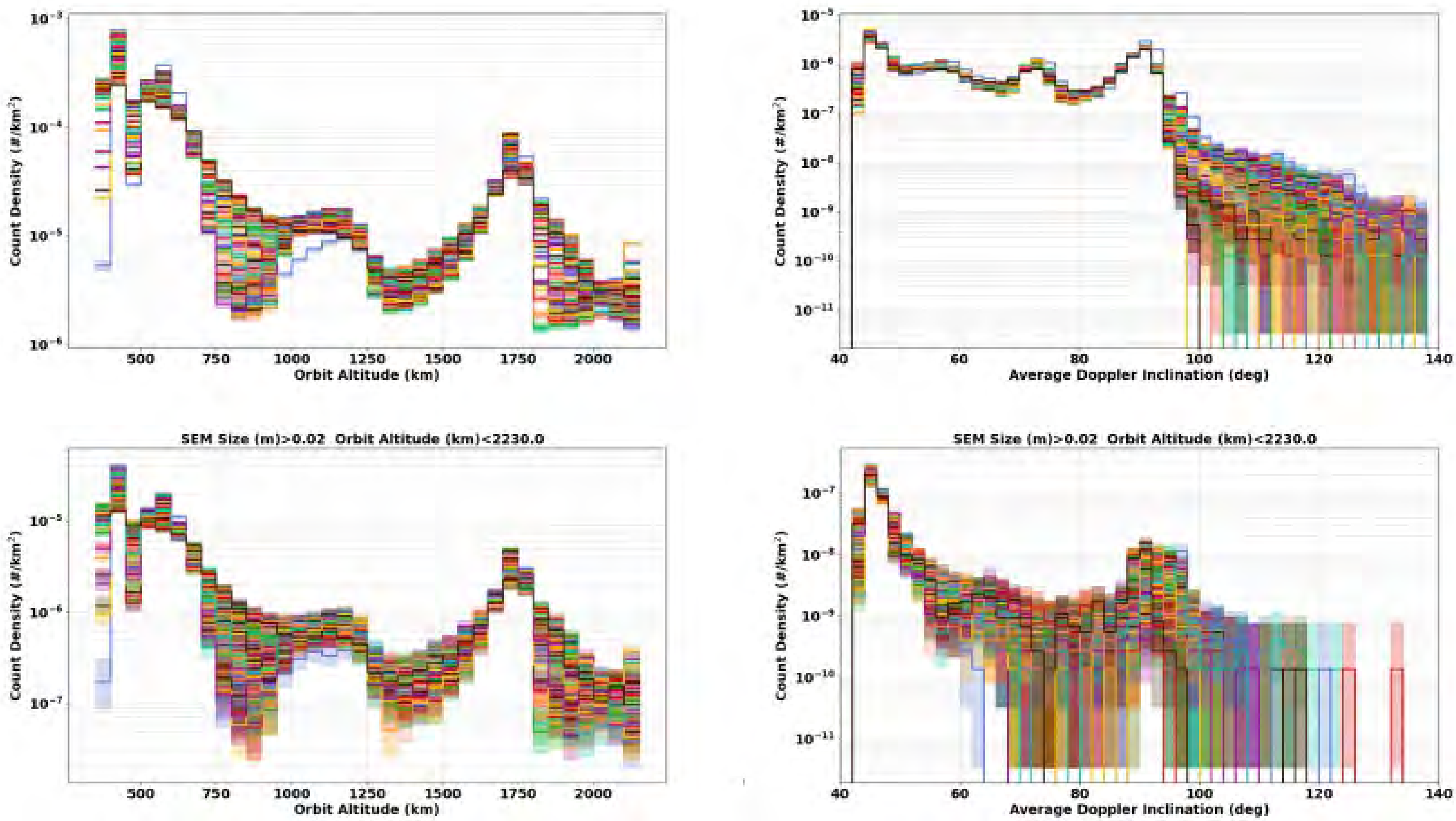

Figure 4-22. Count density in altitude and inclination for 74 modeled SL-23 DEB fragment clouds. Top row shows the total count density, while the bottom shows count density limited to the range window of HUSIR and sensitivity at that range.

In examining the count density versus Doppler inclination charts, it is important to remember that Doppler inclination is calculated using a circular orbit assumption. For measurements of debris in eccentric orbits, the non-zero eccentricity aliases the Doppler inclination away from the true inclination, resulting in the Doppler inclination spread seen in Figure 4-22. In the count density versus Doppler inclination plot shown in the upper right corner of the figure, there are peaks from 44° to 46°, 70° to 76°, and 88° to 98° independent of the true anomaly for the breakup event. In fact, the inclination distributions show significantly less variation than the altitude distributions below 100° inclination. When limiting to the range window and SEM size sensitivity of HUSIR at that range, the variation of the intermediate inclination peaks increases, but the 44° to 46° and 88° to 98° peaks remain consistent. Although, there is no peak in the 50° to 54° Doppler inclination bins, in all cases the distribution of cloud fragments is still significant in that inclination region showing the May 2020 SL-23 DEB fragmentation to be a likely contributor to the flux increases measured in those bins.

For all values of true anomaly for the modeled breakup predictions, the altitude and Doppler inclination distributions consistently predict peak or significantly elevated count densities in altitude and inclination regions measured to have flux increases by HUSIR in CY2020. This indicates the SL-23 DEB fragmentation is likely a major contributor to the flux increases in HUSIR CY2020 data. Once an accurate breakup time is determined, correlation of HUSIR detections to the modeled cloud, similar to that done with Microsat-R, will provide a quantitative measure of the relative effect of this breakup. This is particularly of interest in the 44° to 46°inclination bin in which ORBCOMM FM-16 debris is expected to persist for some time and in the 50° to 54° inclination bins in which there is and will continue to be much traffic from the Starlink satellite constellation.

4.5 HUSIR OBSERVATIONS VS. ORDEM 3.1 PREDICTIONS

HUSIR CY2020 data is compared against the Orbital Debris Engineering Model (ORDEM) 3.1 predictions in this section to assess the current environment against model expectations. Comparisons are made between the cumulative flux distribution as a function of SEM-size, and the surface area flux distribution as a function of altitude.

The cumulative flux distribution as a function of SEM-size for altitudes below 1000 km is shown in Figure 4-23 for both the ORDEM 3.1 model predictions and the HUSIR data. The blue-shaded regions represent the Poisson, 2σ uncertainties in the HUSIR measured counts. In general, the model predictions and data compare well – within the 2σ uncertainties – for SEM sizes greater than approximately 6 mm. For smaller-sized OD objects, the data indicates a higher cumulative flux than the model. The deviation between the model and measured data for OD objects with SEM sizes smaller than approximately 6 mm is higher in 2020 than in 2019. Note that the slope change, which shows up in the measured data for objects with an SEM size less than 8 mm, is likely the result of a signal processing change made to HUSIR data processing for the FY2014 – FY2017 HUSIR measurements. For data processed in this time frame, which was used to build the ORDEM 3.1 model, the monopulse voltage ratio was phase-clamped as discussed in [23]. The phase-clamping, as determined later, was shown to bias some of the objects observed in the medium-to-low SNR regime to slightly larger SEM sizes. The total number of detections remained the same, but the shape of the cumulative size curve was affected in the < 1 cm SEM-size regime. This has been discussed in prior radar reports [5, 23].

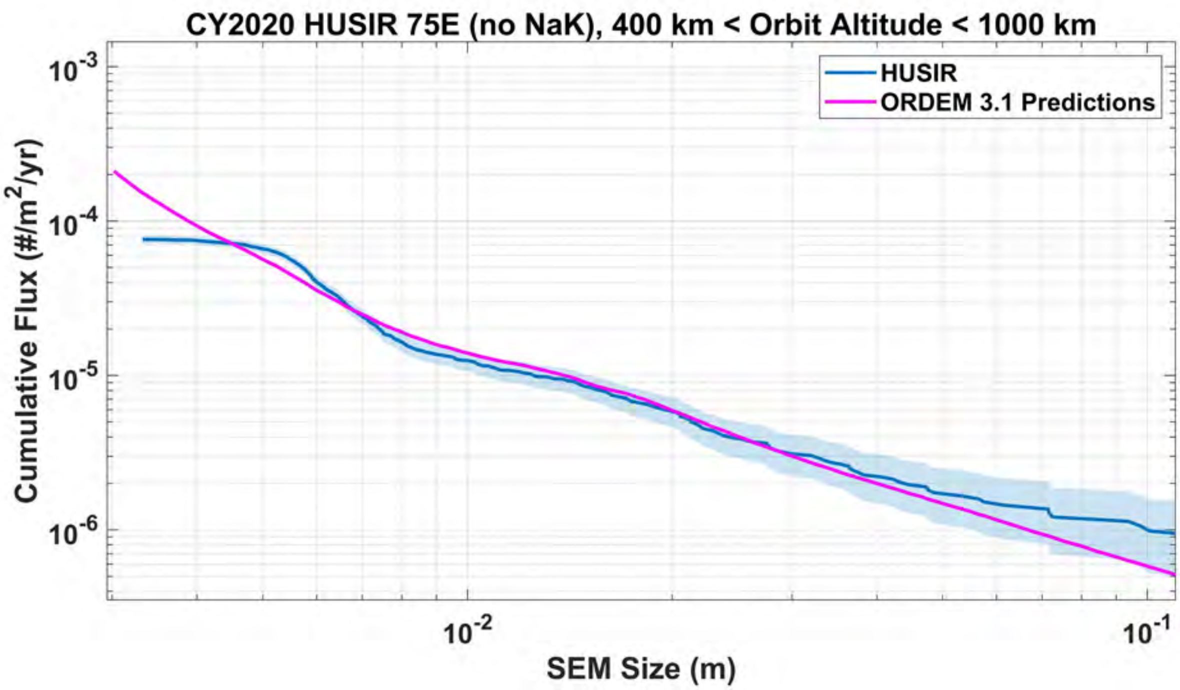

Figure 4-23. Cumulative flux versus SEM size for objects detected with altitudes between 400 km and 1000 km.
The shaded blue region represents Poisson, 2σ uncertainties.

The surface area flux distribution as a function of altitude for both the HUSIR data and ORDEM 3.1 model predictions is shown in Figure 4-24. As described in the plot, the curves are limited to OD with SEM-sizes that are 5.5 mm and larger. This places an altitude constraint on the HUSIR data of approximately 1000 km and below, and the comparison between data and therefore, model predictions are limited to this altitude. As shown in Figure 4-24, both the model and data compare well for many altitudes. Starting at altitudes of 700 km and above, the data indicates a statistically significant, higher flux than the model predictions. The higher flux at 600 km to 950 km, relative to the model predictions, has been noted for several years of observation [5]. The increased flux in the 700 km to 750 km bin, which was discussed in Sections 4.3.2 and 4.4; however, is now comparable to the flux at 750 km to 800 km, and 800 km to 850 km as indicated from HUSIR measurements. The flux increase in the 400 km to 600 km altitude region, observed in CY2019, is not present in a statistically significant way in the CY2020 HUSIR data. The effects of the Microsat-R breakup, which was identified as the most likely contributor to the increased flux observed in 2019, appears to be largely indistinguishable from the background OD environment in 2020.

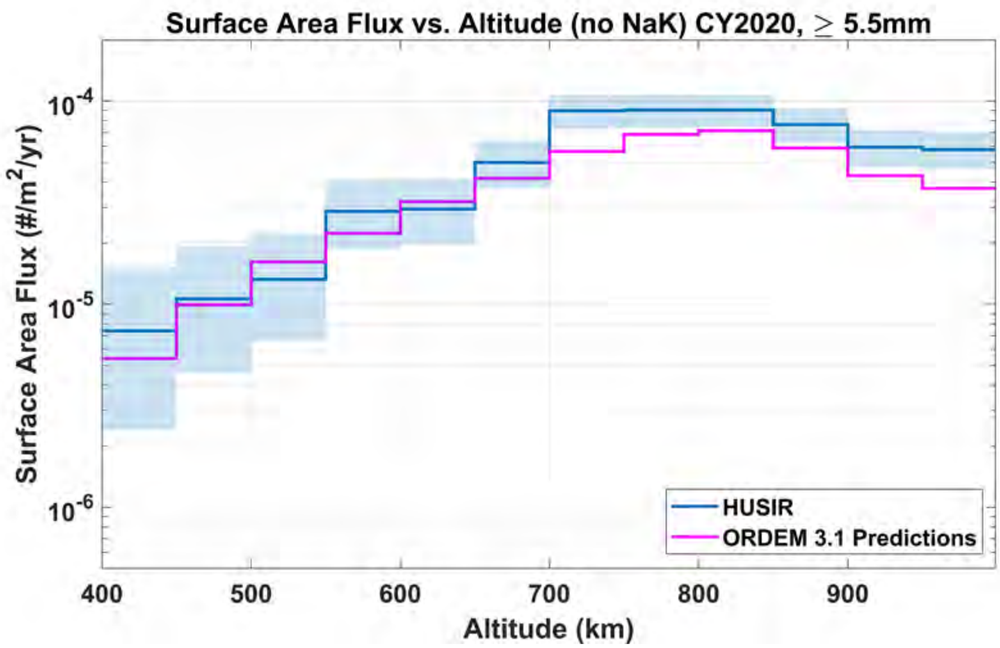

Figure 4-24. Surface area flux versus altitude for objects detected with SEM sizes 5.5 mm and larger. The shaded blue region represents Poisson, 2σ uncertainties.

Restricting the limiting SEM size to 1 cm enables comparison of HUSIR data to the ORDEM 3.1 model to altitudes of approximately 1600 km. Figure 4-25 shows the surface area flux as a function of altitude with OD objects limited to 1 cm and larger. Based on the agreement between the HUSIR data and model shown in Figure 4-23 at cumulative sizes of 1 cm, the good agreement in the surface area flux distribution in Figure 4-25 at many altitudes is expected. For altitudes less than approximately 1150 km – and aside from a data gap at 1000–1050 km – the model predictions are within the Poisson, 2σ uncertainties of the measured data. Starting at approximately 1150 km, there are several altitude bins that have measured flux that is higher than the model. The surface area flux in these altitude bins is significantly less than the flux at lower altitudes; however, which is the likely reason that in comparisons of the HUSIR data and model predictions on just a cumulative SEM size basis, there is no difference observed in the 1 cm and larger population. The higher measured flux at these altitudes was also noted in 2019, where flux in the 1200 km to 1400 km altitude region was noted as elevated relative to ORDEM 3.1 predictions [5]. In 2020, the HUSIR data continues the trend observed in 2019, and extends the altitudes where the deviation starts to 1150 km.

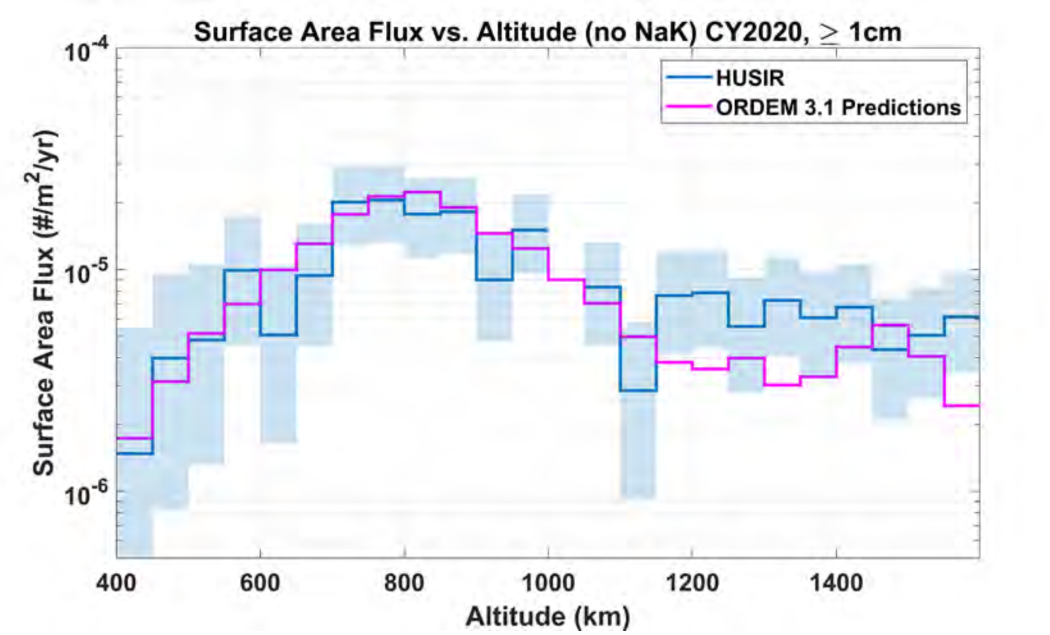

Figure 4-25. Surface area flux versus altitude for objects detected with SEM sizes 1 cm and larger. The shaded blue region represents Poisson, 2σ uncertainties.

5.0 Summary

The LEO environment as observed by HUSIR in CY2020 and measurements from the radar were discussed and analyzed. Data taken with the new waveform developed for RFI mitigation was compared to data taken with the legacy waveform in the same year to validate and determine whether a permanent waveform change would affect the quality of data collected.

A total of 342 observation hours were processed and analyzed from HUSIR at 75E-, 20S-, and 10S-pointing geometries and both the 10 GHz and 10.1 GHz waveforms. Approximately 237 hours met requirements for analysis following the RFI removal process. Detected objects were measured for RCS, range, and range-rate and polarization. This data was analyzed to produce orbital altitude and inclination, size, and flux distributions.

An experimental waveform with a center frequency of 10.1 GHz developed for the mitigation of RFI was discussed. The effects of the center frequency change on the radar performance and calibration were analyzed. Test measurement taken between April and June 2020 showed an average of 0.4 dB increase in sensitivity of the 10.1 GHz waveform over that of the 10 GHz waveform. Spiral scans performed during preliminary waveform testing indicated a similar beam pattern between the two frequencies. The fractional difference in beamwidth of polynomial fits to the two scans was less than 1%. Overall, a change of the center frequency to 10.1 GHz does not negatively affect the sensitivity or beam pattern of the radar.

The identification and removal of RFI from the dataset was discussed. The percentage of detections determined to be RFI has risen exponentially since first discovered in the FY2014 data. In CY2020, 52.2% of all detections in the 10 GHz data were determined to be affected by RFI: over half of all detections. This corresponds to 38.3% of the total observation hours in the 10 GHz data being affected by RFI. Of the data taken at 10.1 GHz, only 1.7% of hours were affected by any form of RFI. All affected hours for the new waveform were taken at a low elevation angle, 10°, which is a staring geometry inherently prone to the interception of stray terrestrial signals. The new 10.1 GHz waveform has proven to effectively mitigate RFI.

Cumulative size distributions for CY2018, CY2019, and CY2020 were compared. These comparisons between years provide a broad overview of the state of the OD environment in LEO. Cumulative count rates were comparable across all datasets down to a limiting size, with the CY2018 and CY2019 distributions rolling off sooner than the CY2020 datasets at smaller sizes. Cumulative size distributions of the 10 GHz and 10.1 GHz, CY2020, 75E data were compared. The cumulative count rate between the two waveforms was within confidence intervals at all sizes.

Surface area flux versus altitude and surface area flux versus inclination for CY2018, CY2019, and CY2020 were compared. Slight flux increases from 550 km to 600 km, from 700 km to 750 km, and from 1150 km to 1250 km were identified. The METEOR 3-5 R/B fragmentation was discussed as a possible contributing source to the 1150 km to 1250 km flux increase. Many Starlink satellites were launched in CY2020. Although the orbit-raising profile of Starlink satellites has complicated the correlation of detections to the constellation using TLEs, traffic related to the Starlink constellation has increased the 52° to 54° inclination flux and the 550 km to 600 km altitude flux. However, the main component of the 550 km to 600 km flux increase was determined to be related to an 88° to 90° inclination flux increase. Increased flux in the 72° to 76° inclination bin was determined to be related to the 700 km to 750 km altitude flux increase. The 44° to 46° inclination flux increase identified in CY2019 has persisted into CY2020, bolstering the candidate source as being ORBCOM FM-16, although fragments from the new SL-23 DEB fragmentation may also be a new source in the region. The low altitude flux has returned to nominal levels from the increase observed in CY2019. This indicates the Microsat-R ASAT test likely made only a short-term contribution to the small debris environment in LEO.

Surface area flux versus altitude and surface area flux versus inclination for 10 GHz and 10.1 GHz data were compared. For all inclination bins where detections were made by both waveforms, there was good agreement between the two waveforms. Flux versus altitude showed good agreement with a slightly higher flux in 500 km to 550 km altitude bin measured by the 10.1 GHz waveform, although still within overlapping uncertainties. To within the counting uncertainties, analysis thus far has shown that the 10 GHz data and 10.1 GHz data produce comparable results.

The second fragmentation of SL-23 DEB was investigated as a possible contributing source to increased flux observed in some of the altitude and inclination bins. Lacking a precise breakup time, many debris clouds were modeled with the breakup occurring at multiple true anomalies. It was shown that although the shape of the cloud in range, range-rate, and time is dependent on the time of breakup, when averaged to produce altitude and Doppler inclination flux, all values of true anomaly predicted peak flux for the cloud in many altitudes and inclinations for which increased flux was measured in CY2020. This indicates the event is likely a significant contributor to flux increases observed. Future work to determine an accurate breakup time is of interest to provide a quantitative measure of the relative effect of this breakup in altitude and inclination bins related to the ORBCOMM FM-16 breakup and Starlink satellite constellation.

This report presented key results from the curated CY2020, HUSIR radar measurements of the OD environment. HUSIR data has been the primary source of information for the development of NASA’s OD models down to a limiting size in LEO. Continued monitoring of the environment in the size ranges efficiently measured by HUSIR is needed to continue updating, validating, and refining these models.

6.0 References

1) Stansbery, E., Tracy, T., *et al*., “Characterization of the Orbital Debris Environment using the Haystack Radar, Appendix A,” JSC-32213, 1993.

2) Horstman, M. F. and Papanyan, V.O., *et al*, Haystack and HAX Radar Measurements of the Orbital Debris Environment: 2006 – 2012, NASA/TP-2014-217391, NASA Johnson Space Center, Houston, TX, USA, 2014.

3) Murray, J., Blackwell, C., Gaynor, J., *et al.*, Haystack Ultra-Wideband Satellite Imaging Radar Measurements of the Orbital Debris Environment: 2014-2017, NASA/TP-2019-220302, NASA Johnson Space Center, Houston, TX, USA, 2019.

4) Stokely, C. L., Foster, J.L., *et al.*, Haystack and HAX Radar Measurements of the Orbital Debris Environment; 2003, NASA/ JSC-, Johnson Space Center, Houston, TX, USA, November 2006.

5) Murray, J. and Kennedy, T., Haystack Ultra-Wideband Satellite Imaging Radar Measurements of the Orbital Debris Environment: 2019, NASA/TP-2021-0013669, NASA Johnson Space Center, Houston, TX, USA, 2021.

6) Matney, M., Anz-Meador, P., Murray, J., *et al.*, “The NaK Population: A 2019 Status,” 1st International Orbital Debris Conference, Sugar Land, TX, December 2019.

7) Foster, J.L., Krisko, P., *et al.,* “NaK Droplet Source Modeling,” IAC-03-IAA.5.2.02, 54th International Astronautical Congress, Bremen, Germany, 2003.

8) Krisko, P.H. and J.L. Foster. “Modeling the sodium potassium droplet interactions with the low earth orbit space debris environment,” *Acta Astronautica 60*, pp. 939-945, 2007.

9) Dalquist, C. and Bohannon, G. “Physical Descriptions of Debris Objects Used in Static RCS Measurements,” XonTech Report 910555-1978, August 1991.

10) Bohannon, G., Caampued, T., and Young, N. “First Order RCS Statistics of Hypervelocity Impact Fragments,” XonTech Report 940128-BE-2305, April 1994.

11) Barton, D. K., *et al*., “Final Report of the Haystack Orbital Debris Data Review Panel,” NASA/JSC Technical Memorandum 4809, Houston, TX, February 1998.

12) Everett, R., Caampued, T., and Chu, J. “Summary of Data Processing of September 1990 SPC Debris Data,” XonTech Report 910147-1937, March 1991.

13) Everett, R., Dalquist, C., and Caampued, T. “Summary of Processing of January 1991 SPC Debris Data,” XonTech Report 9100393-1965, July 1991.

14) Hill, N. “Measurement Techniques for Hypervelocity Impact Test Fragments,” 59th International Astronautical Congress, Glasgow, Scotland, 2008.

15) Xu, Y.-l and C.L. Stokely. "A Statistical Size Estimation Model for Haystack and HAX Radar Detections," 56th International Astronautical Congress, Fukuoka, Japan, 2005.

16) "2018 Ends with Breakup of an ORBCOMM Constellation Spacecraft," Orbital Debris Quarterly News Vol. 23, Issues 1 & 2, pp. 1, 2019.

17) Peterson, G., Sorge, M., and McVey, J., "Forensic Analysis of Debris-Generating Events: Orbcomm FM 16," 1st International Orbital Debris Conference, Sugar Land, TX, December 2019.

18) Johnson, N., Krisko, P., *et al.*, NASA's New Breakup Model of EVOLVE 4.0. Adv. Space Res., 28 (9), 1377-1384, 2001.

19) Ester, M., Kriegel, H., *et al.*, A density-based algorithm for discovering clusters in large spatial databases with noise. Proceedings of the Second International Conference on Knowledge Discovery and Data Mining (KDD-96). AAAI Press. pp. 226–231, 1996.

20) Pedregosa, F., Varoquaux, G., *et al*., Scikit-learn: Machine Learning in Python, JMLR 12, pp. 2825-2830, 2011.

21) "Second Fragmentation of *Fregat* Upper Stage Debris," Orbital Debris Quarterly News Vol. 24, Issues 3, pp. 2-3, 2020.

22) Slatton, Z. and McKissock, D., "Methods of Predicting and Processing Breakups of Space Objects," 7th European Conference on Space Debris, 2017.

23) Murray, J. and Kennedy, T., Haystack Ultra-Wideband Satellite Imaging Radar Measurements of the Orbital Debris Environment: 2018, NASA/TP-2020-5006606, NASA Johnson Space Center, Houston, TX, USA, 2020.

Appendix A: Total Number of Hours Received from MIT/LL

Table A-1: Data Collection Summary Reflecting the Total Number of Observation Hours Received from MIT/LL in CY2020

Waveform	75° East	20° South	10° South	Total Received	Total Retained
	Hours of Observation	Hours of Observation	Hours of Observation	Hours of Observation	Hours of Observation
10.0 GHz	166.6	57.2	45.5	269.2	166.2
10.1 GHz	37.4	17.7	17.2	72.3	71.1

Appendix B: Empirical Sensitivity Estimation

To aid in comparisons between data taken at different radar sensitivities, it is necessary to estimate the size to which a dataset is complete, *i.e.*, all objects of that size and larger are being detected. This quantity is strongly dependent on the range from the target due to the $1/R^4$ dependence of the radar range equation. To remove the range effects and focus on the noise-limiting characteristics of the receiver, we define a quantity we call "excess SNR" or XSNR. XSNR scales the measured RCS of all detections to a common range of 1000 km. In decibels, XSNR is defined as

$$XSNR_{dB} = RCS_{dB} - 40 \log_{10} \frac{R_{km}}{1000}$$

where RCS_{dB} is the measured RCS in decibels and R_{km} is the range of the detection in kilometers. While this quantity can be calculated for PP RCS, OP RCS, or total RCS, here we specifically focus on the PP XSNR. Figure B-1 shows a cumulative distribution of PP XSNR for the HUSIR CY2020, 75E, 10.1 GHz dataset. Here it can be seen that the distributions follow a power law across a wide range of XSNR, from which a roll-off at smaller values can be easily and consistently determined from dataset to dataset. The power law deviation at larger values of XSNR likely is related to the automatic gain control employed by HUSIR, which reduces the sensitivity of the receiver to avoid saturation during the detection of larger objects.

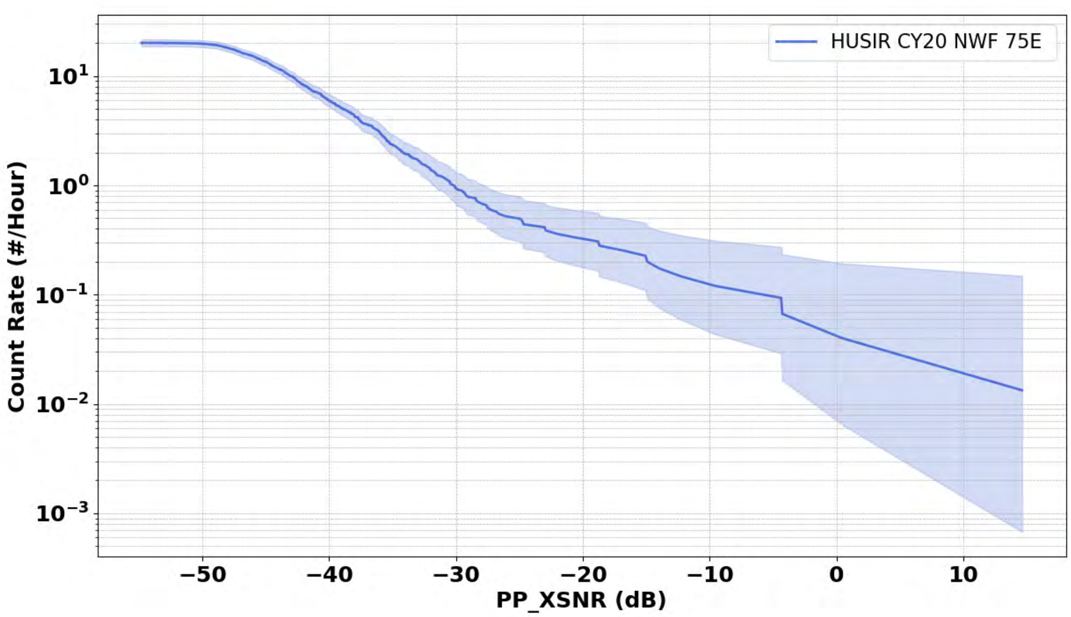

Figure B-1. Cumulative PP XNR for the HUSIR CY2020 75E, 10.1 GHz dataset.

To estimate the XSNR at which a dataset rolls-off, an automated method was developed. The basic steps involve performing a least-squares fit in log-log space on a subinterval of the

PP XSNR distribution, taking the ratio of the fit to the data, and then determining at what XSNR the data-to-fit ratio falls below predefined levels of completeness. To choose the optimal subinterval of the distribution, the data is resampled at 100 points evenly in log-log space using the Piecewise Cubic Hermite Interpolating Polynomial (PCHIP) routine, excluding the top and bottom 1% of the data. Figure B-2 shows an example cumulative PP XSNR versus log10(counts) showing the original distribution in blue and the resampled distribution in orange.

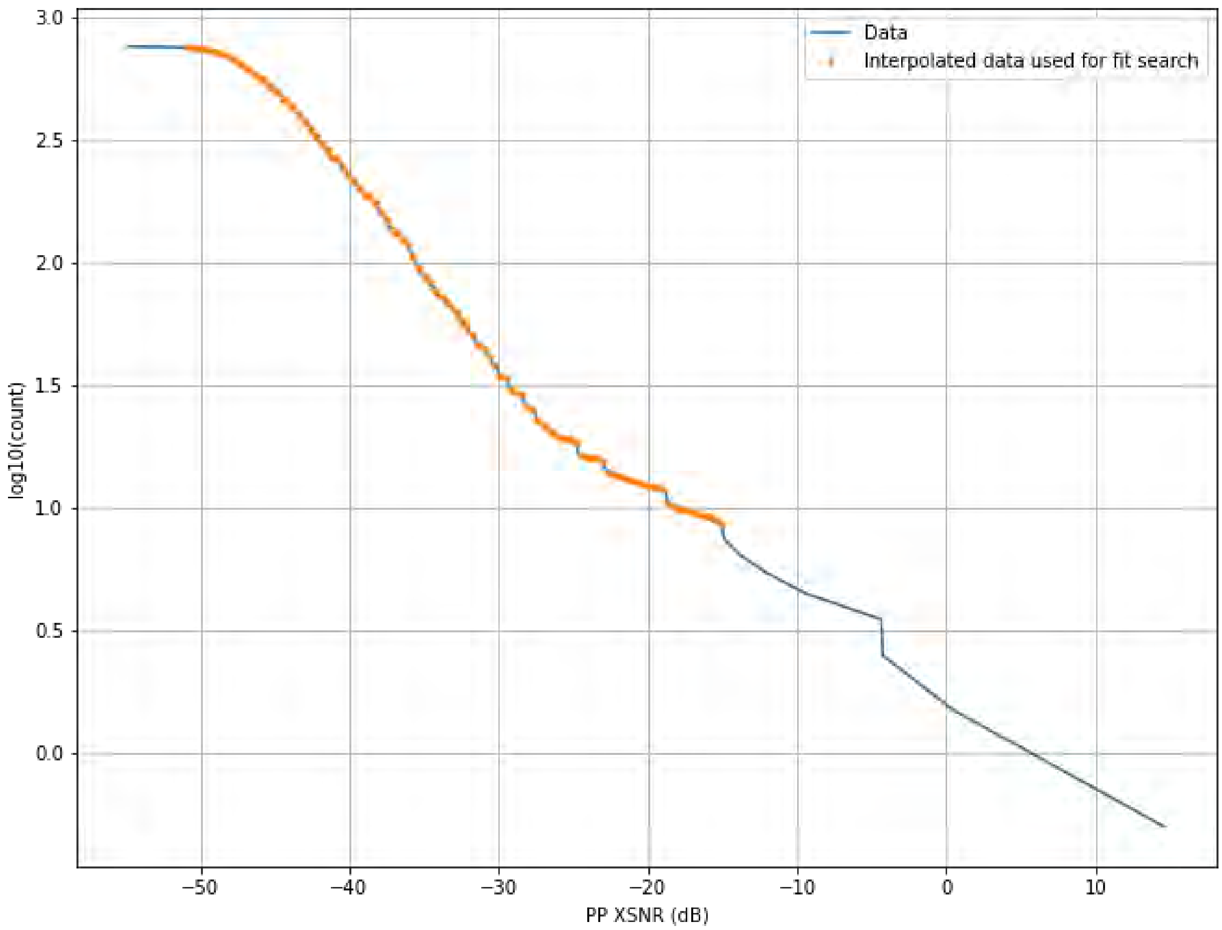

Figure B-2. Cumulative PP XSNR versus log10(counts) showing the original distribution in blue and the resampled distribution in orange.

To find the optimal subinterval to use for the fit, all contiguous subintervals that contain at least 10% of the resampled points are checked. For each of these candidate subintervals, a least-squares fit in log-log space is performed and the coefficient of determination, R^2, of the fit is calculated. The subinterval that maximizes the R^2 is chosen for the final fit. A ratio of the cumulative counts from the data relative to the cumulative counts predicted by the final fit is then taken in the roll-off region to determine at what values of XSNR the ratio falls below 0.99, 0.95, and 0.90, which correspond to 99%, 95%, and 90% levels of completeness. Figure B-3 shows an example ratio of data to fit in the roll-off region, with completeness XSNR values and corresponding sizes at 1000 km altitude to 99%, 95%, and 90% indicated.

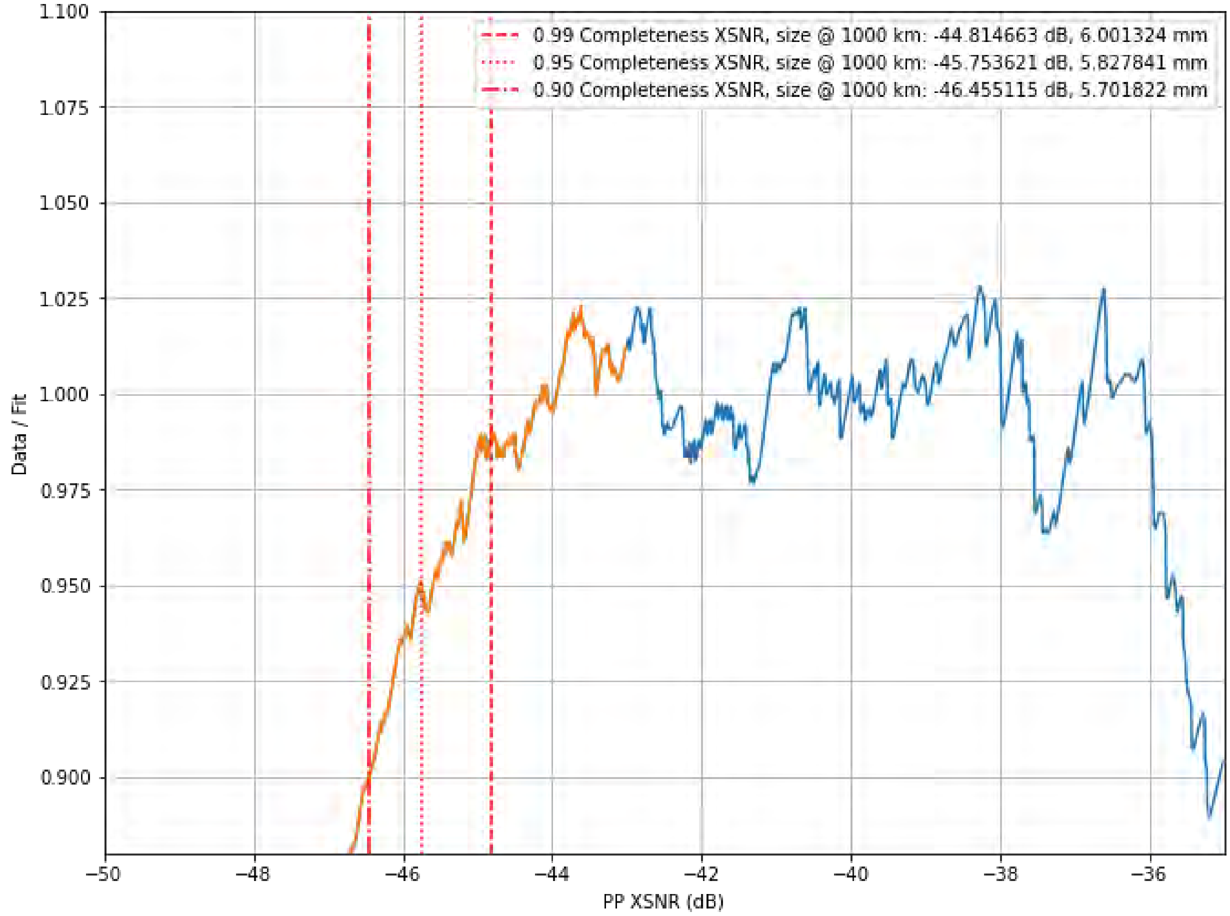

Figure B-3. Example ratio of data to fit in the roll off region, with completeness XSNR values and corresponding sizes at 1000 km altitude to 99%, 95%, and 90% indicated.

Figure B-4 shows, for the HUSIR CY2020, 75E, 10.1 GHz dataset, the cumulative PP XSNR distribution with the original data as a blue line, the resampled points used in the fit as red "+" symbols, the linear fit as a dashed black line, and the XSNR levels for a data to model fit ratio of 99%, 95%, and 90% as red dashed, dotted, and dash-dotted vertical lines. When compared in this way, the 99% line corresponds roughly to where the data starts to diverge from the linear fit. It also turns out that the 95% completeness XSNR is comparable to the theoretical size of an object with a single-pulse SNR of 5.65 dB shown as a function of altitude in Section 4.2.3. In general, the completeness sizes estimated using this new method are consistent with previous estimates. Charts equivalent to Figure B-4 all pointings and waveforms are shown in Figures B-5 through B-9.

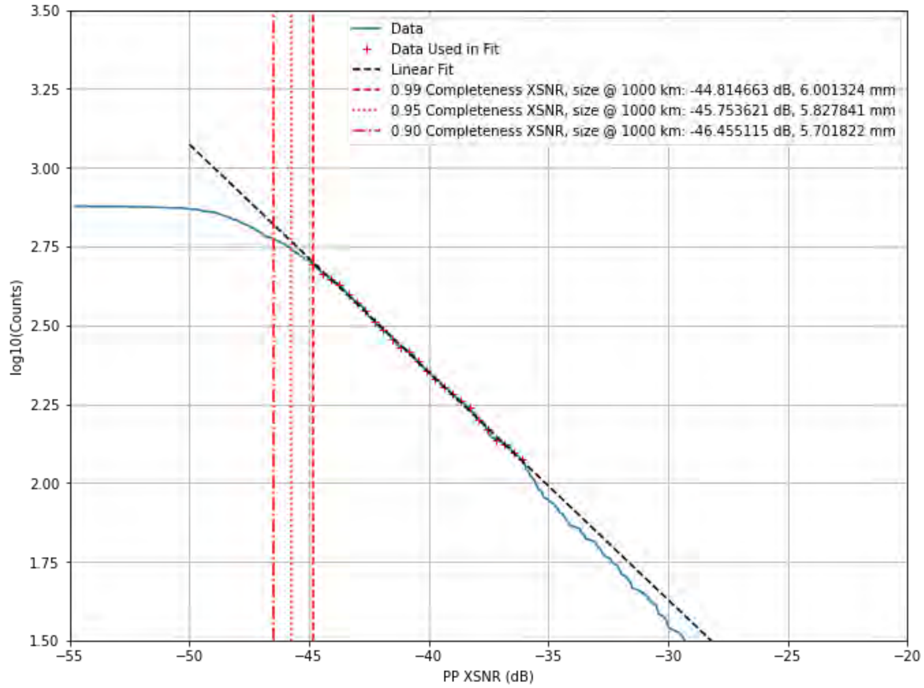

Figure B-4. HUSIR CY2020, 75E, 10.1 GHz cumulative PP XSNR distribution with the original data as a blue line, the resampled points used in the fit as red "+" symbols, the fit as a dashed black line, and the XSNR levels of 99%, 95%, and 90% as red dashed, dotted, and dash-dotted vertical lines.

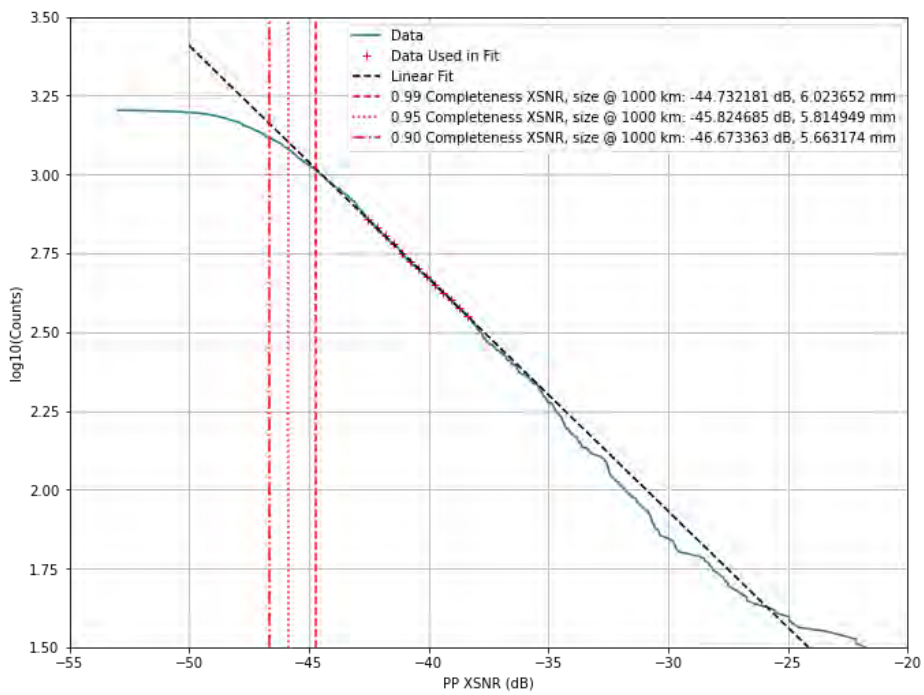

Figure B-5. HUSIR CY2020, 75E, 10.0 GHz cumulative PP XSNR distribution with the original data as a blue line, the resampled points used in the fit as red "+" symbols, the fit as a dashed black line, and the XSNR levels of 99%, 95%, and 90% as red dashed, dotted, and dash-dotted vertical lines.

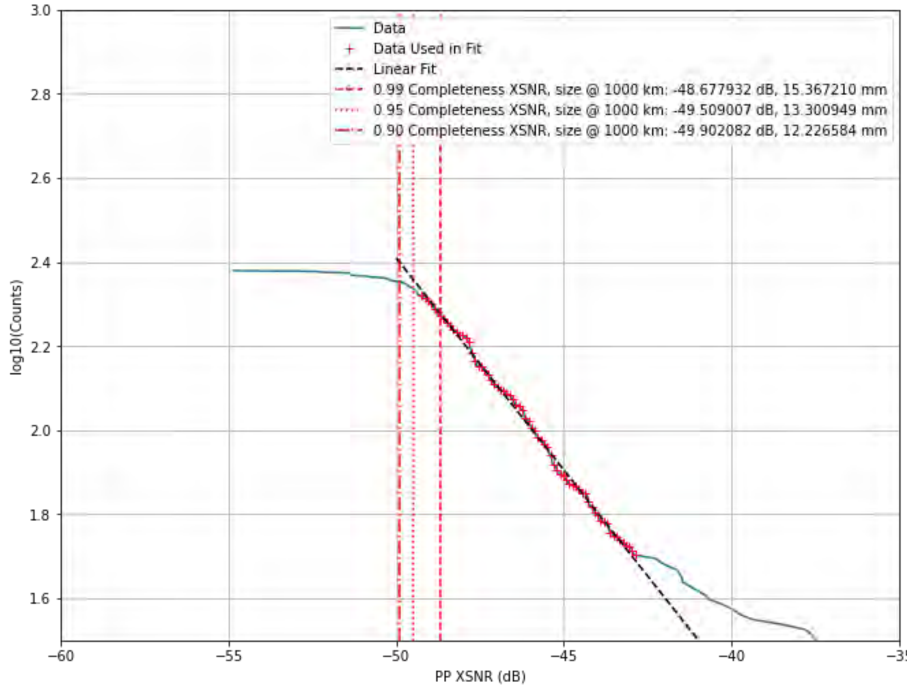

Figure B-6. HUSIR CY2020, 20S, 10.1 GHz cumulative PP XSNR distribution with the original data as a blue line, the resampled points used in the fit as red "+" symbols, the fit as a dashed black line, and the XSNR levels of 99%, 95%, and 90% as red dashed, dotted, and dash-dotted vertical lines.

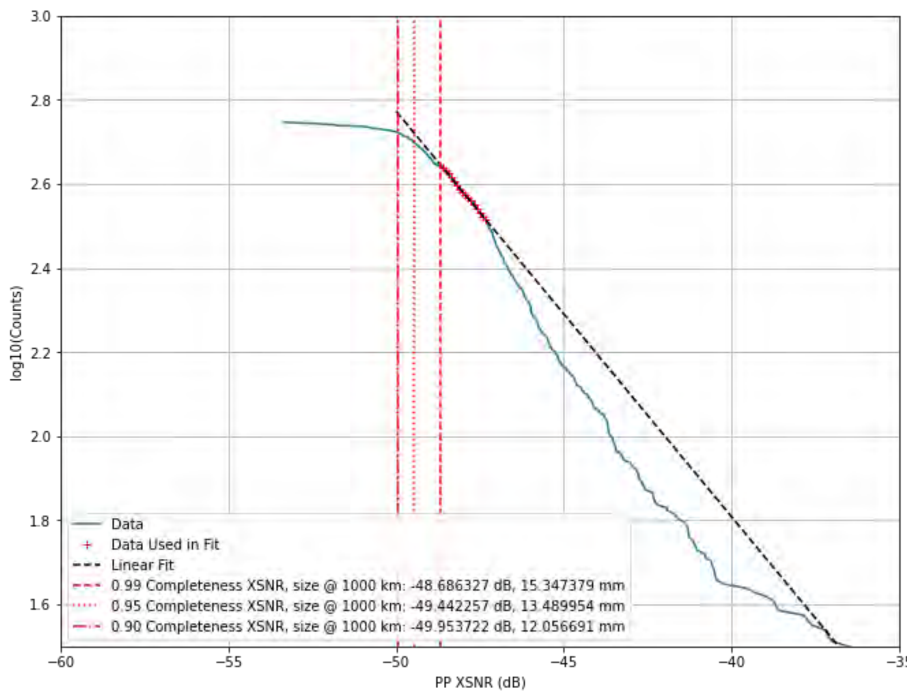

Figure B-7. HUSIR CY2020, 20S, 10.0 GHz cumulative PP XSNR distribution with the original data as a blue line, the resampled points used in the fit as red "+" symbols, the fit as a dashed black line, and the XSNR levels of 99%, 95%, and 90% as red dashed, dotted, and dash-dotted vertical lines.

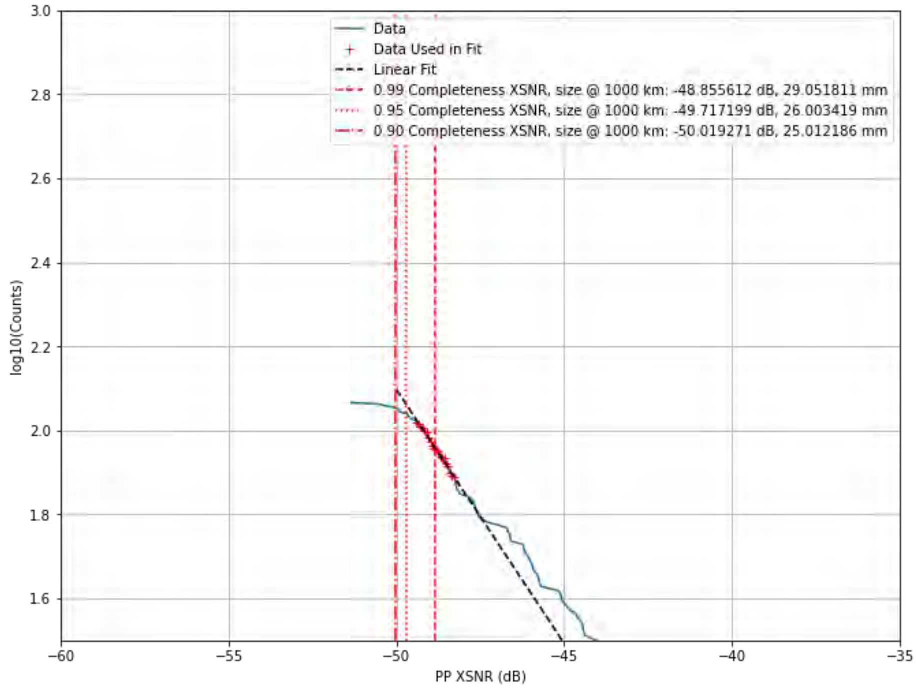

Figure B-8. HUSIR CY2020, 10S, 10.1 GHz cumulative PP XSNR distribution with the original data as a blue line, the resampled points used in the fit as red "+" symbols, the fit as a dashed black line, and the XSNR levels of 99%, 95%, and 90% as red dashed, dotted, and dash-dotted vertical lines.

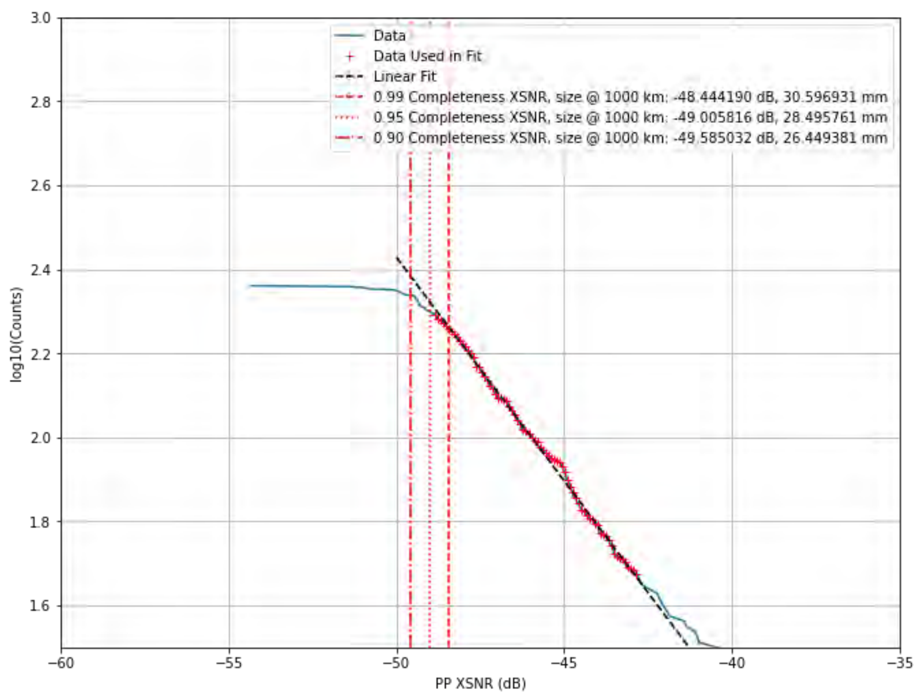

Figure B-9. HUSIR CY2020, 10S, 10.0 GHz cumulative PP XSNR distribution with the original data as a blue line, the resampled points used in the fit as red "+" symbols, the fit as a dashed black line, and the XSNR levels of 99%, 95%, and 90% as red dashed, dotted, and dash-dotted vertical lines.

Appendix C: HUSIR 75° Elevation, East Pointing, 10.0 GHz

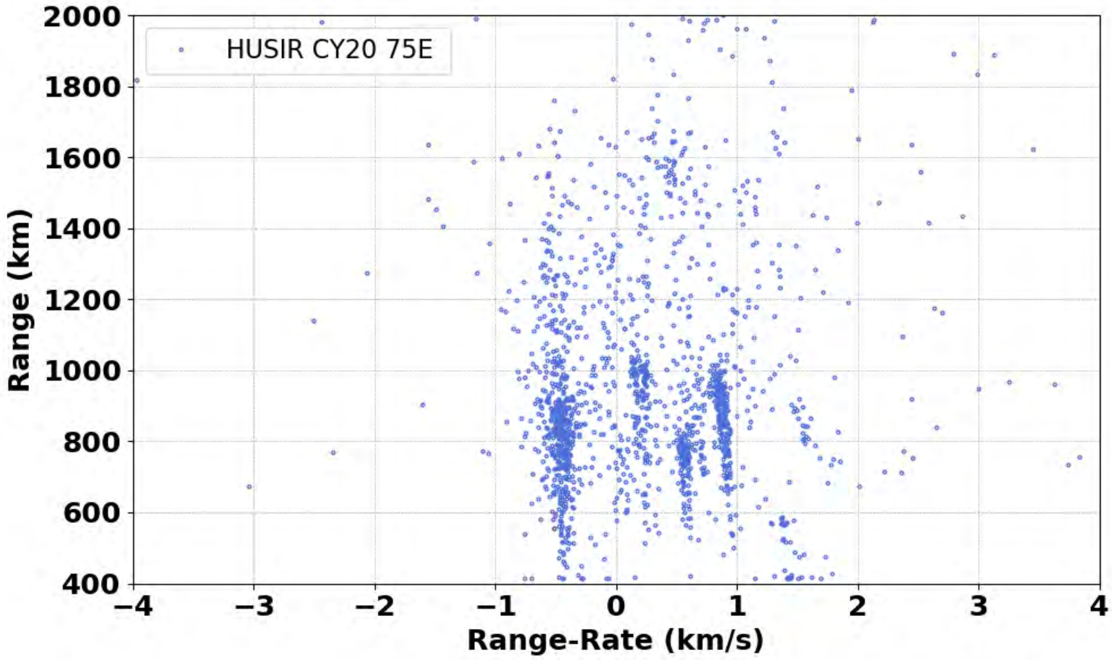

Figure C-1. Range versus Range-Rate, HUSIR 75E, CY2020.

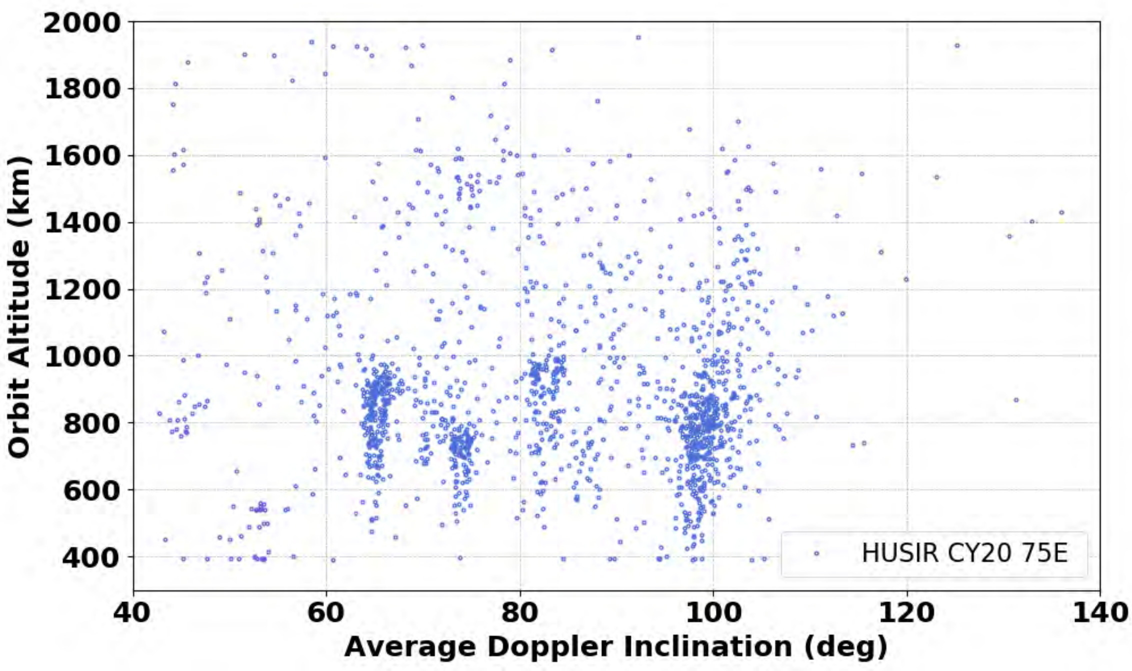

Figure C-2. Altitude versus Doppler inclination, HUSIR 75E, CY2020.
Inclination derived from Range and Range-Rate assuming a circular orbit.

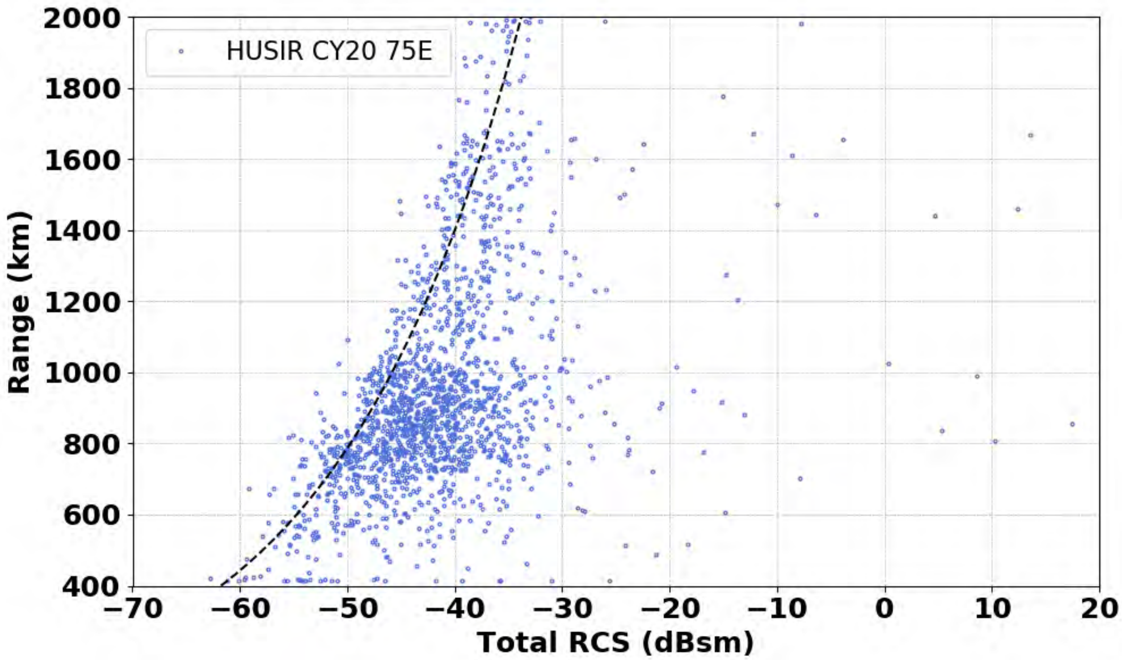

Figure C-3. Range versus Radar Cross Section, HUSIR 75E, CY2020.
The black dashed line represents the theoretical RCS of an object
with a single-pulse SNR of 5.65 dB as a function of range.

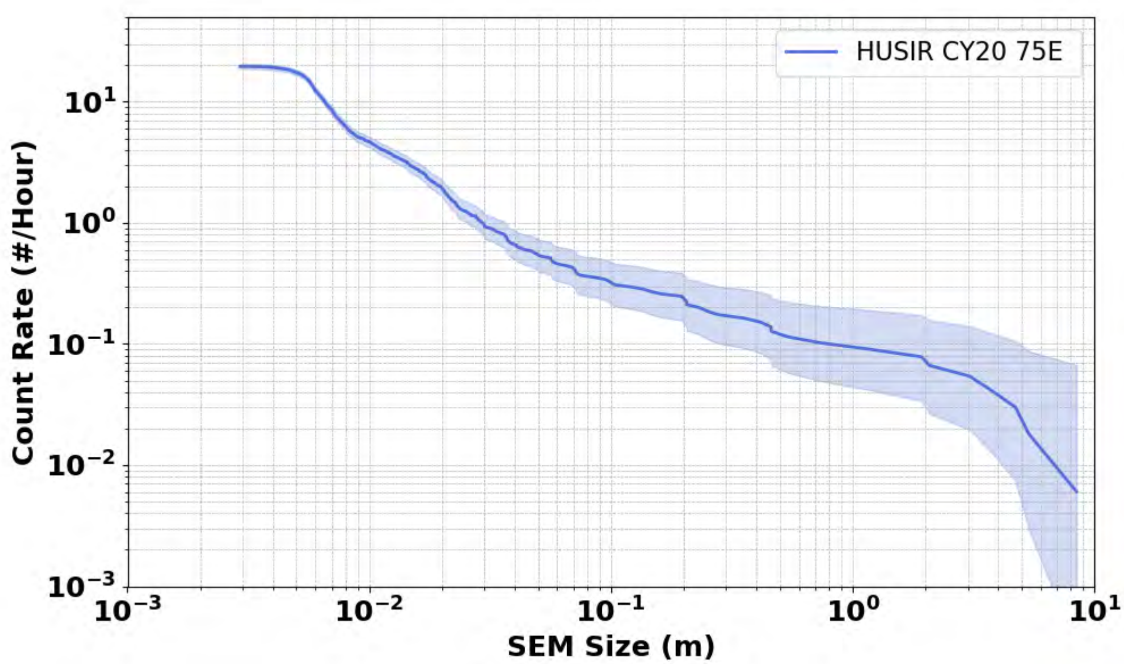

Figure C-4. Cumulative count rate versus SEM Size, HUSIR 75E, CY2020.

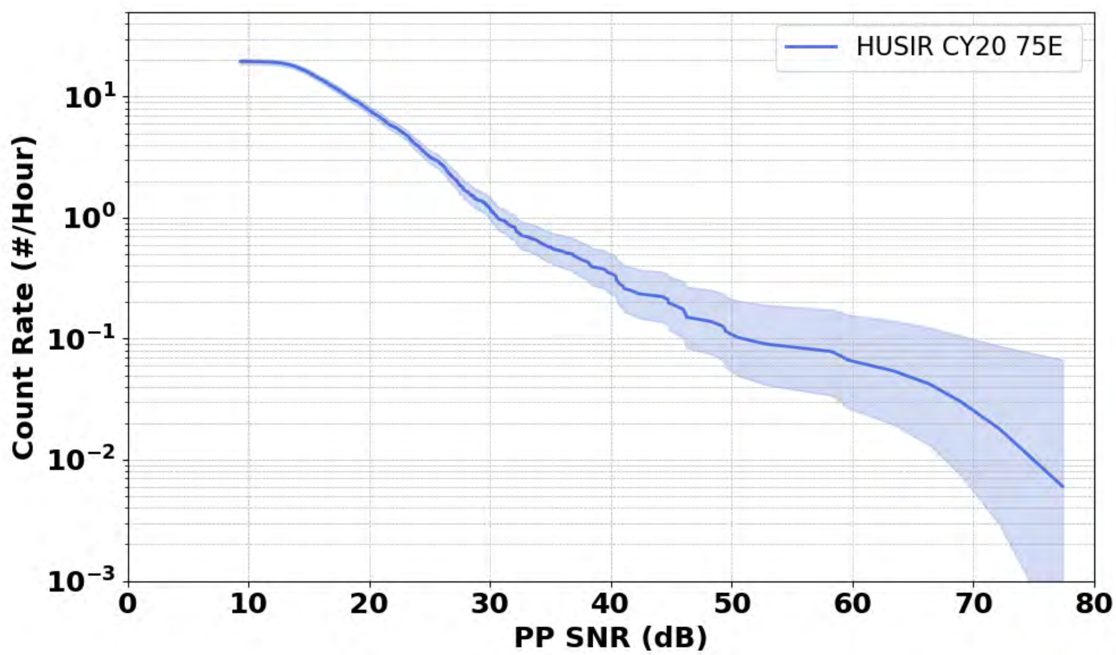

Figure C-5. Cumulative count rate versus detection SNR of the principal polarization, HUSIR 75E, CY2020.

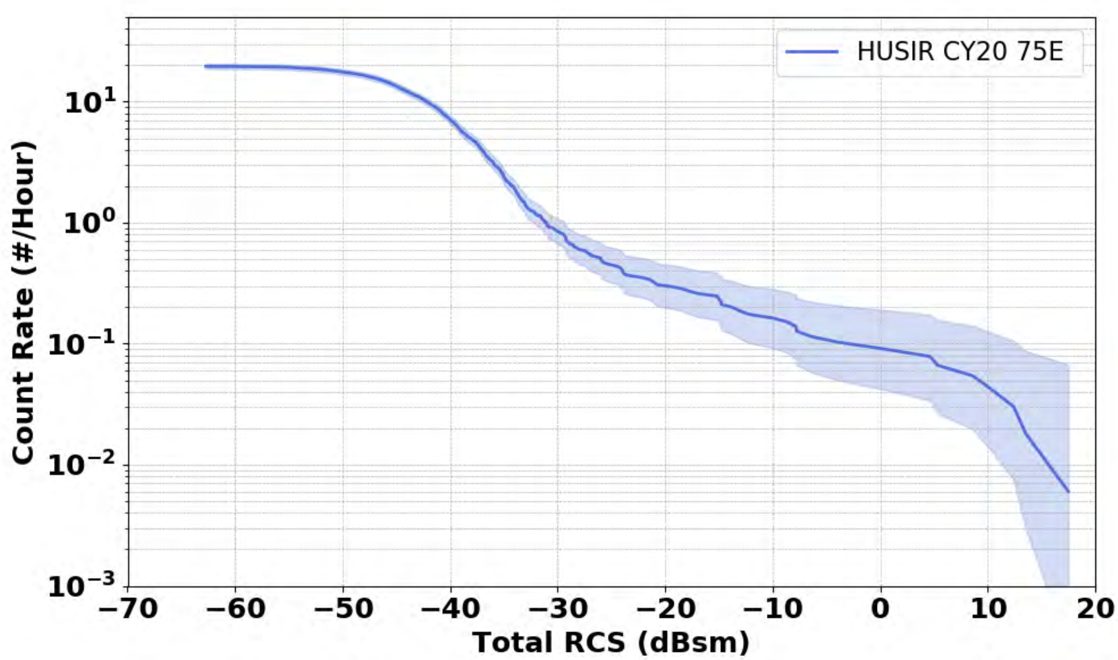

Figure C-6. Cumulative count rate versus Total Radar Cross Section, HUSIR 75E, CY2020.

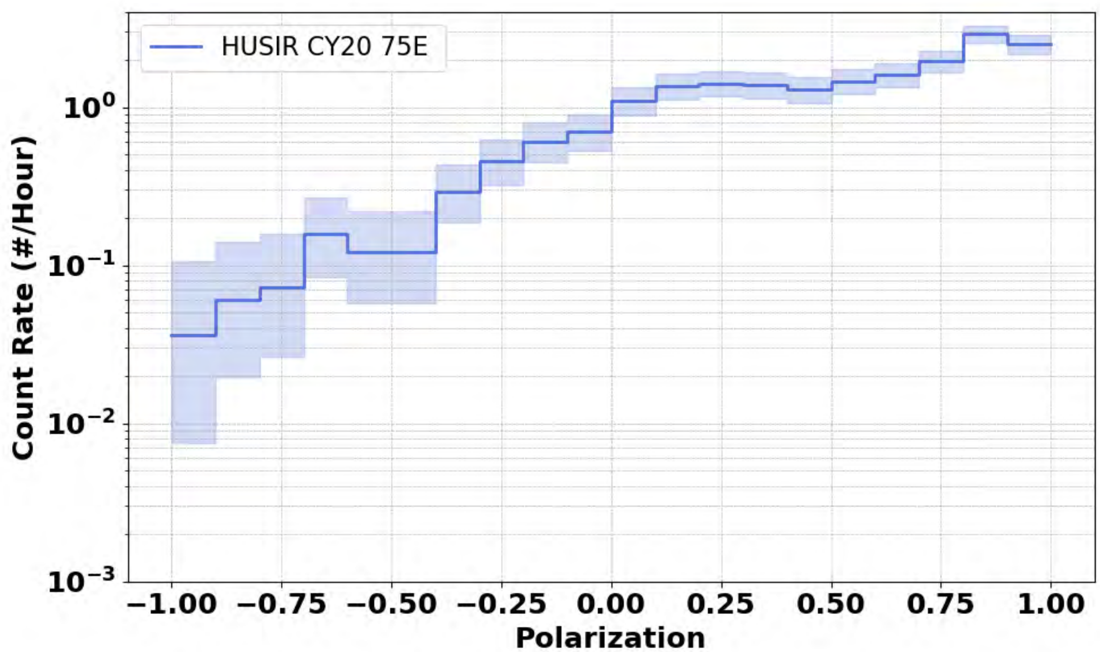

Figure C-7. Count Rate versus polarization ratio, HUSIR 75E, CY2020.

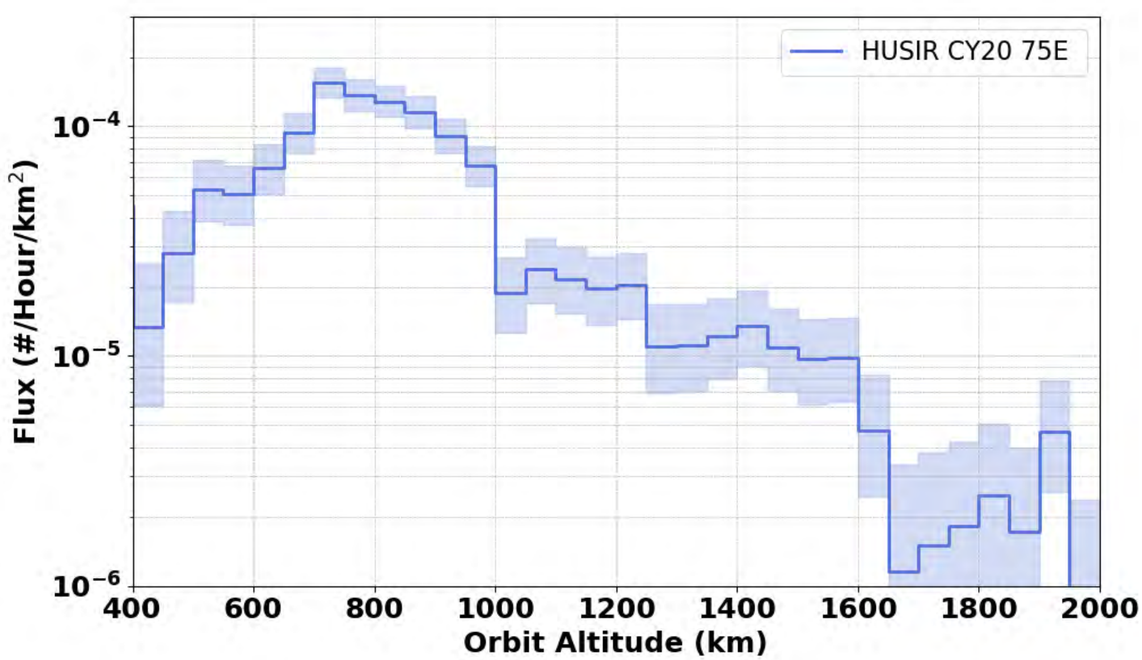

Figure C-8. Flux versus altitude, HUSIR 75E, CY2020. No size or altitude limits are applied.

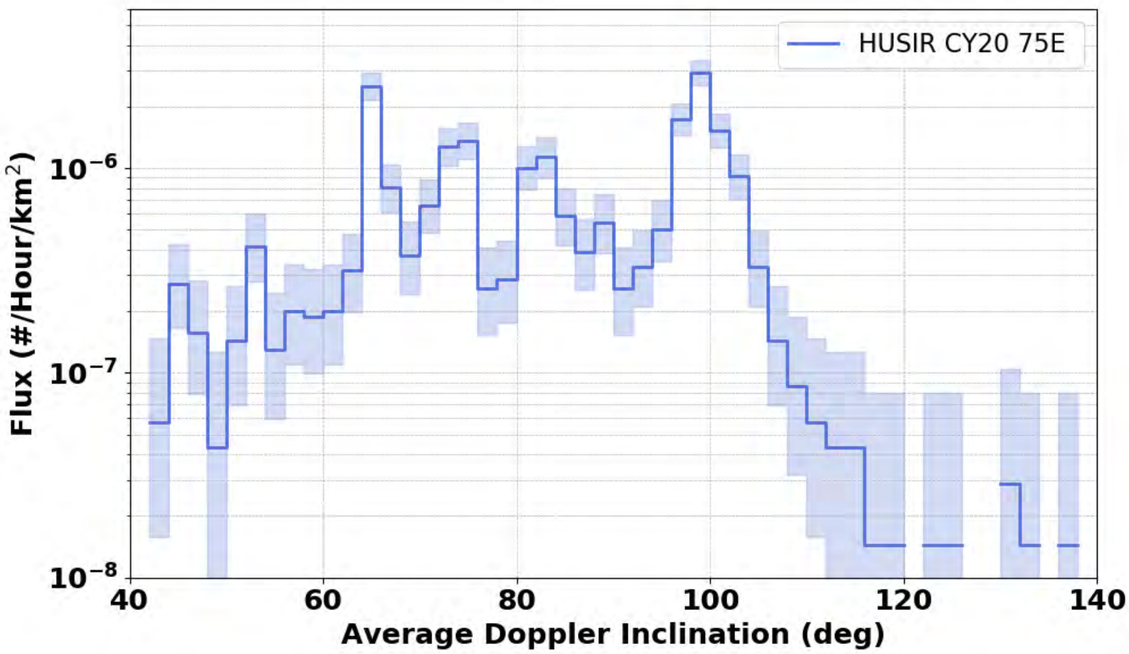

Figure C-9. Flux versus orbital inclination, HUSIR 75E, CY2020. No size or altitude limits are applied.

Appendix D: HUSIR 75° Elevation, East Pointing, 10.1 GHz

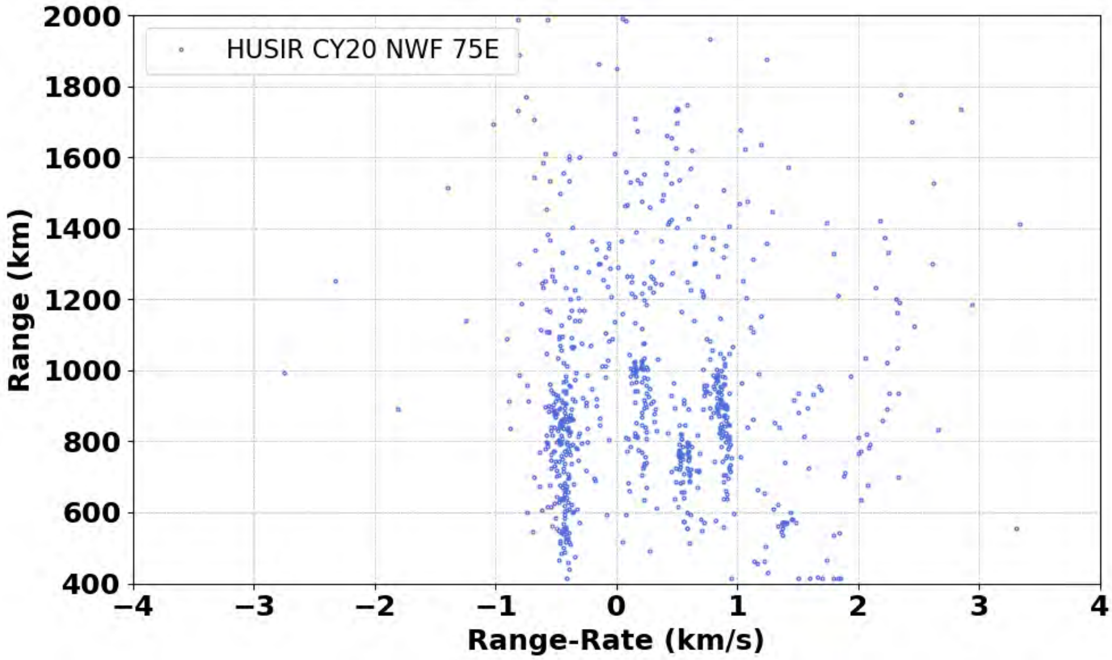

Figure D-1. Range versus Range-Rate, HUSIR 75E, CY2020.

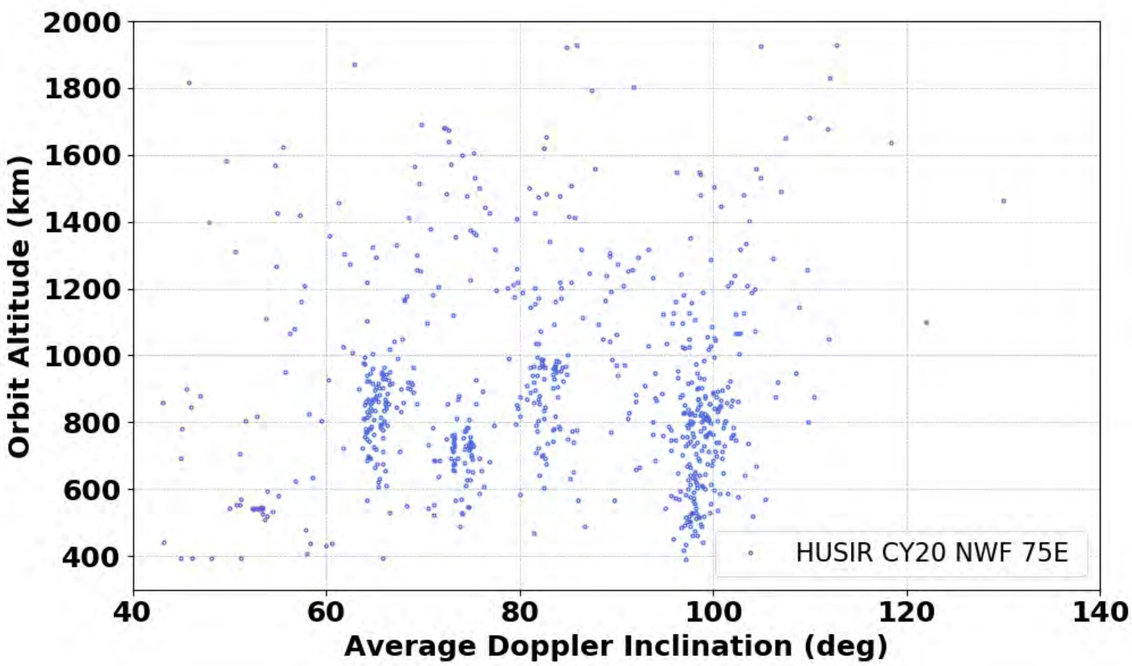

Figure D-2. Altitude versus Doppler inclination, HUSIR 75E, CY2020.
Inclination derived from Range and Range-Rate assuming a circular orbit.

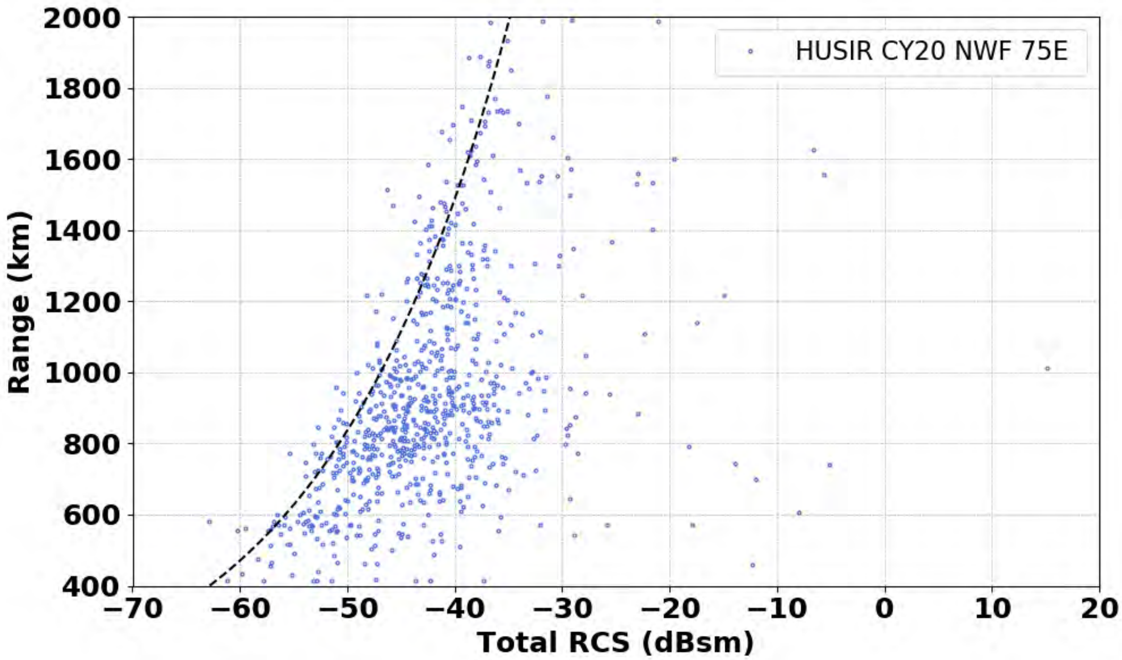

Figure D-3. Range versus Radar Cross Section, HUSIR 75E, CY2020.
The black dashed line represents the theoretical RCS of an object
with a single-pulse SNR of 5.65 dB as a function of range.

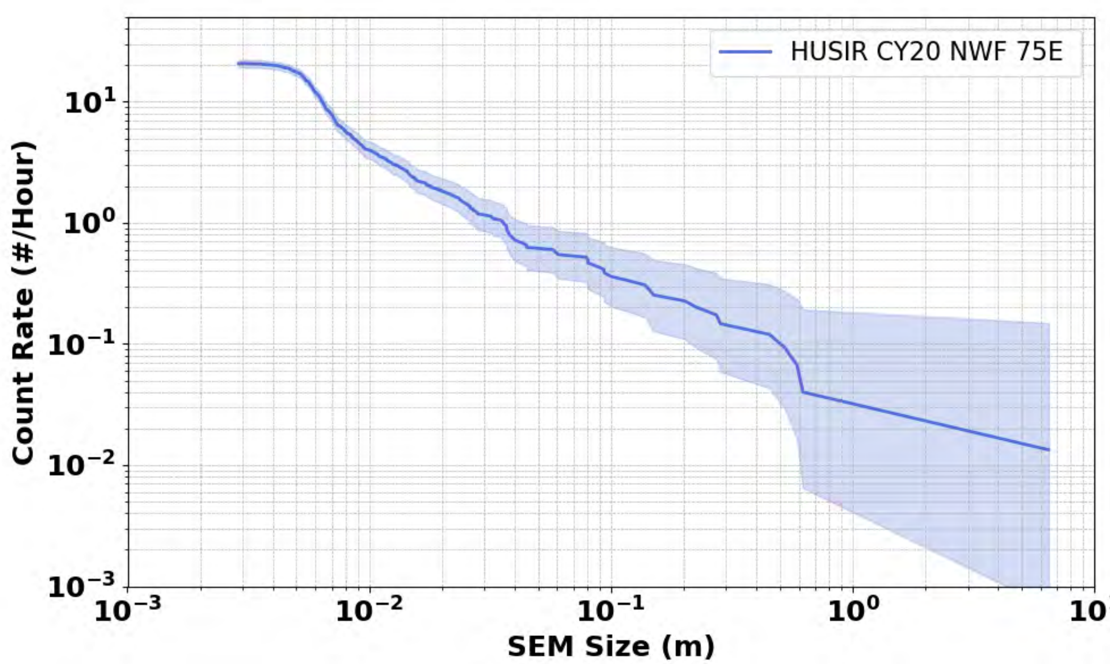

Figure D-4. Cumulative count rate versus SEM Size, HUSIR 75E, CY2020.

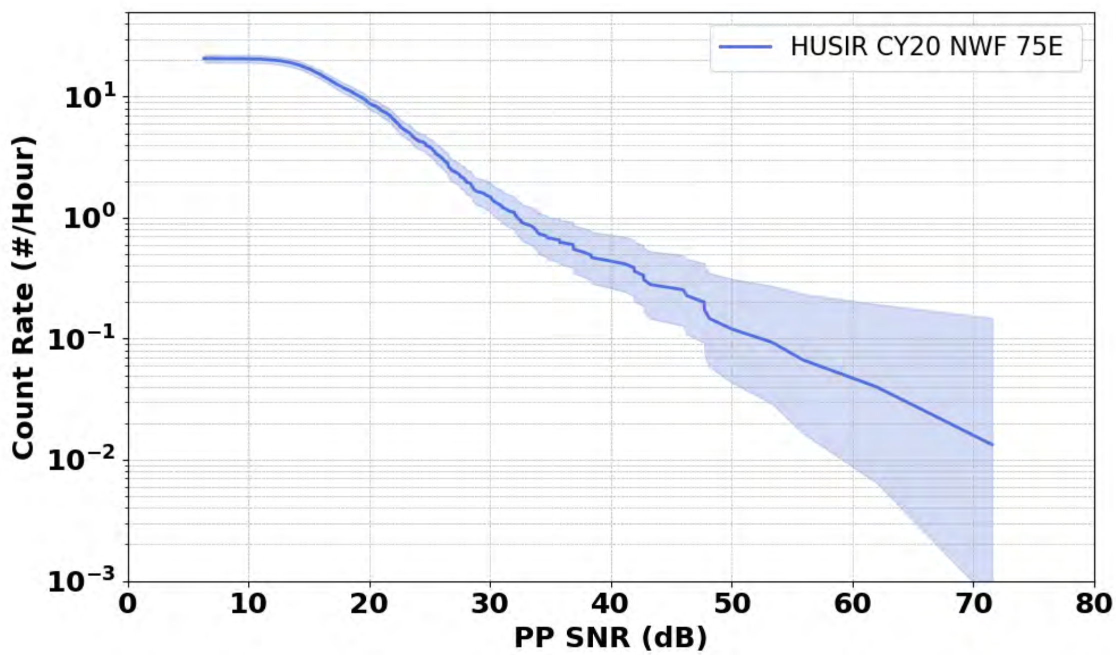

Figure D-5. Cumulative count rate versus detection SNR of the principal polarization, HUSIR 75E, CY2020.

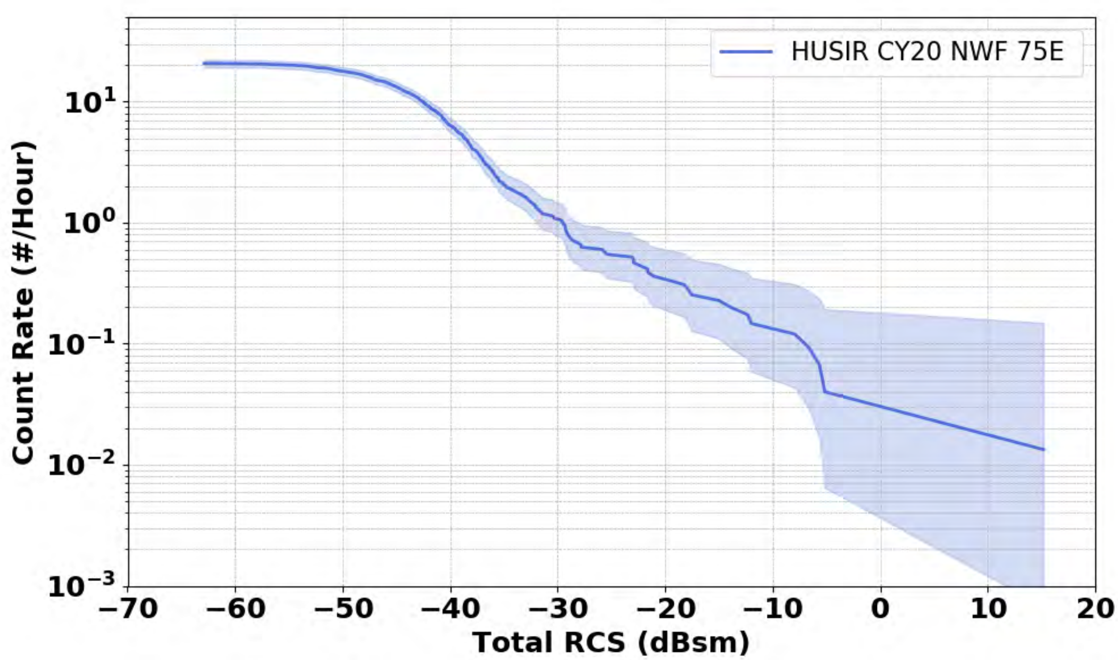

Figure D-6. Cumulative count rate versus Total Radar Cross Section, HUSIR 75E, CY2020.

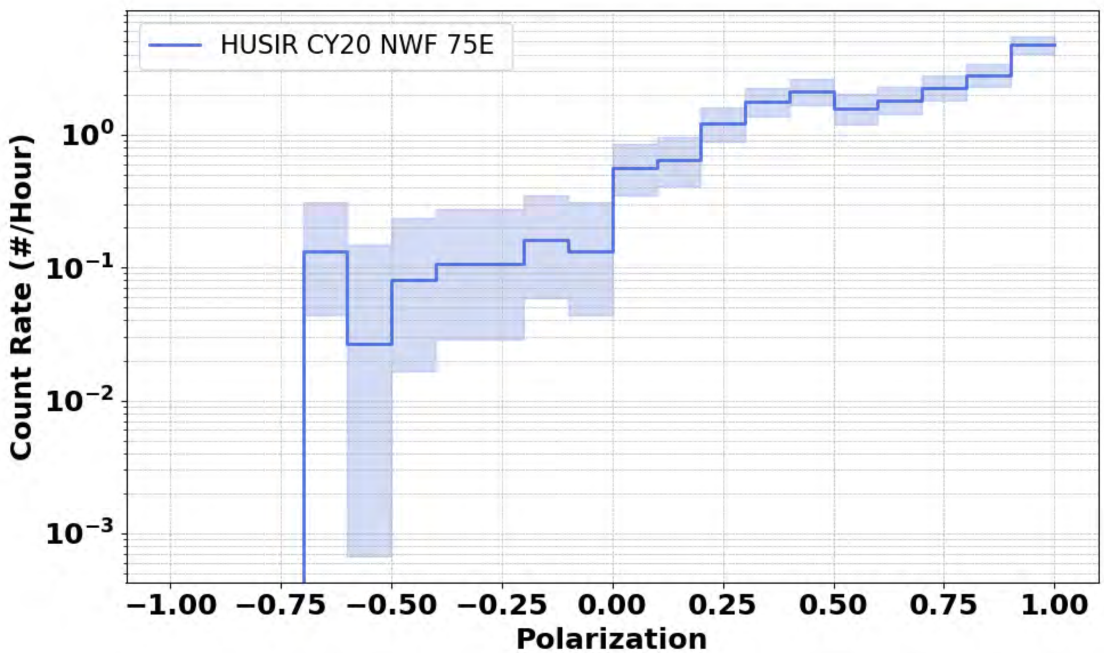

Figure D-7. Count Rate versus polarization ratio, HUSIR 75E, CY2020.

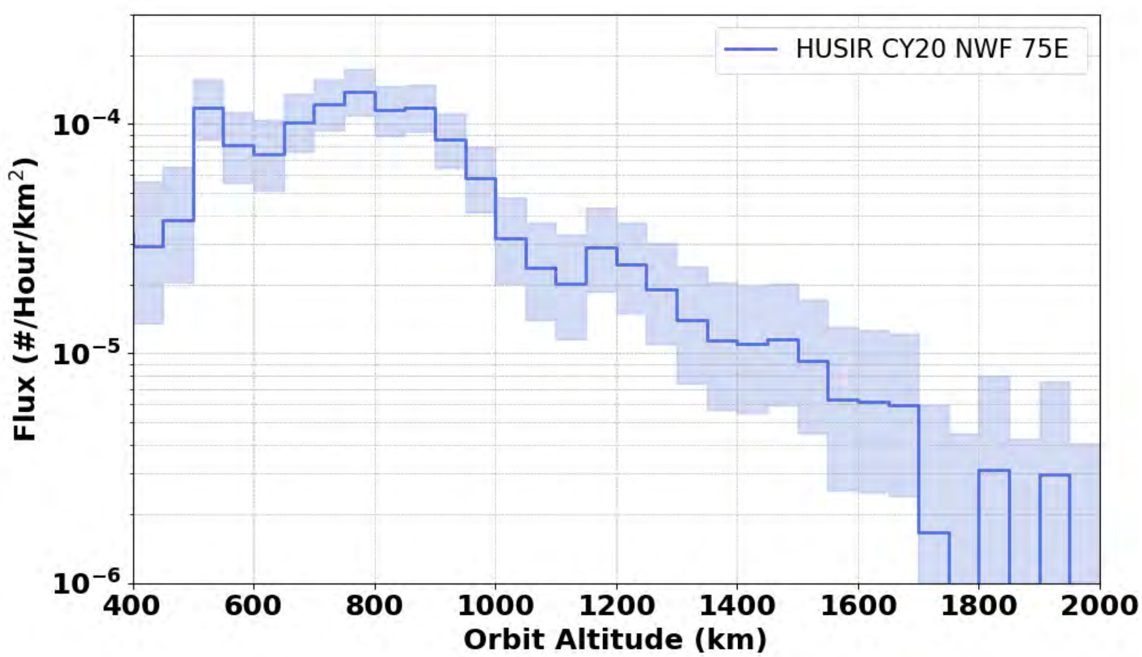

Figure D-8. Flux versus altitude, HUSIR 75E, CY2020. No size or altitude limits are applied.

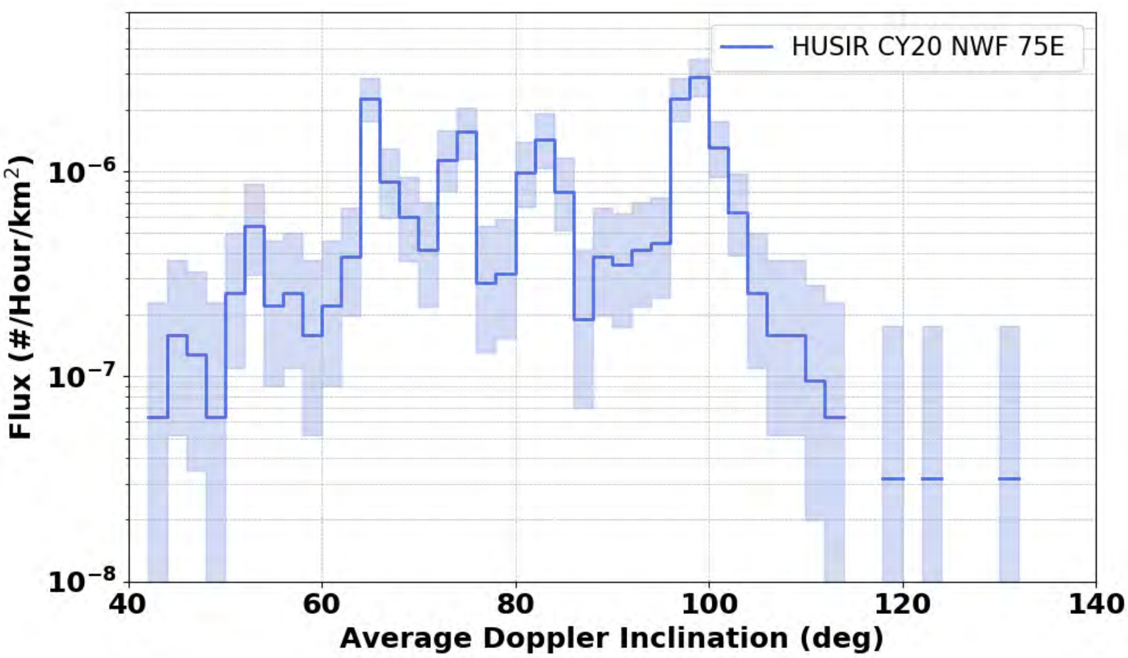

Figure D-9. Flux versus orbital inclination, HUSIR 75E, CY2020. No size or altitude limits are applied.

Appendix E: HUSIR 10° Elevation, South Pointing, 10.0 GHz

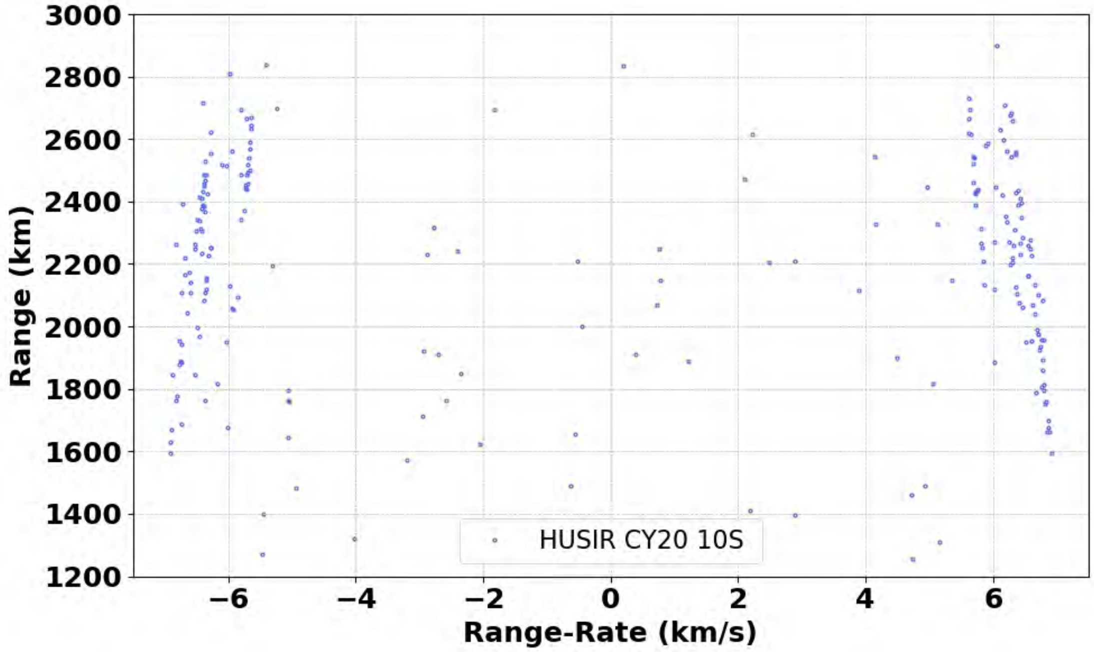

Figure E-1. Range versus Range-Rate, HUSIR 10S, CY2020.

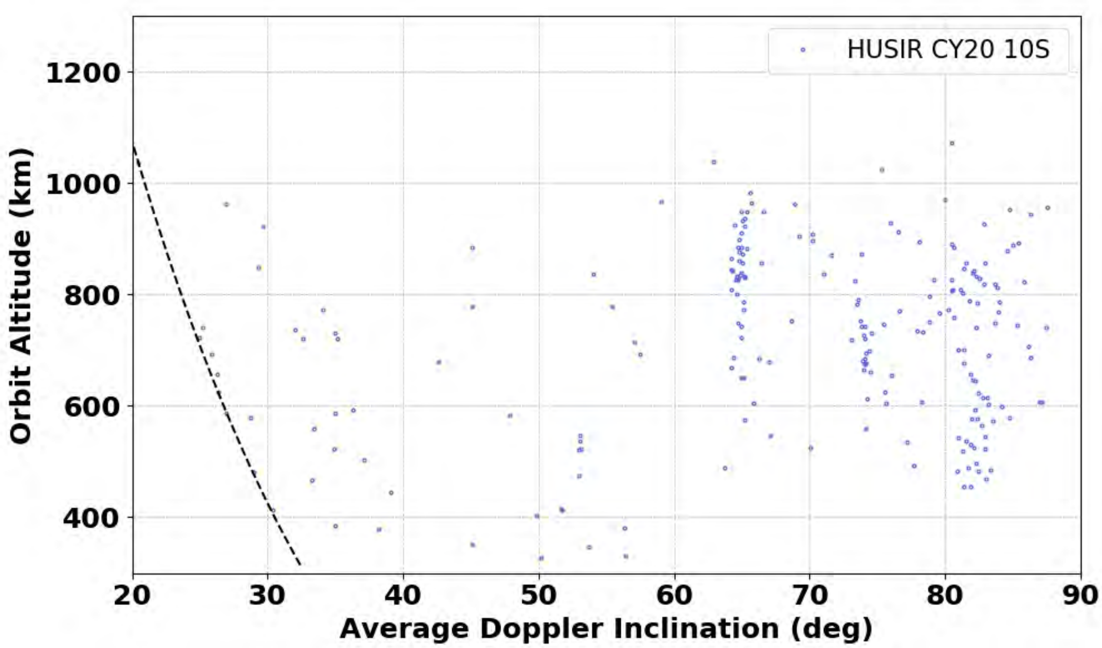

Figure E-2. Altitude versus Doppler inclination, HUSIR 10S, CY2020.
Inclination derived from Range and Range-Rate assuming a circular orbit. The dashed black line represents the minimum inclination visible to HUSIR as a function of orbit altitude.

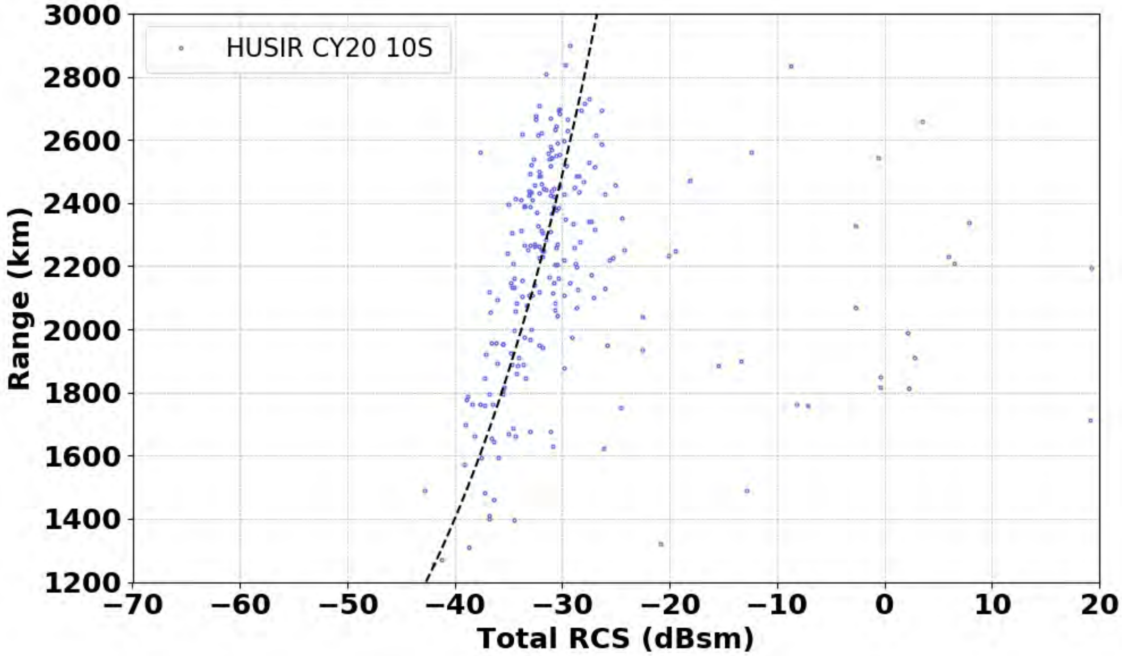

Figure E-3. Range versus Radar Cross Section, HUSIR 10S, CY2020.
The black dashed line represents the theoretical RCS of an object
with a single-pulse SNR of 5.65 dB as a function of range.

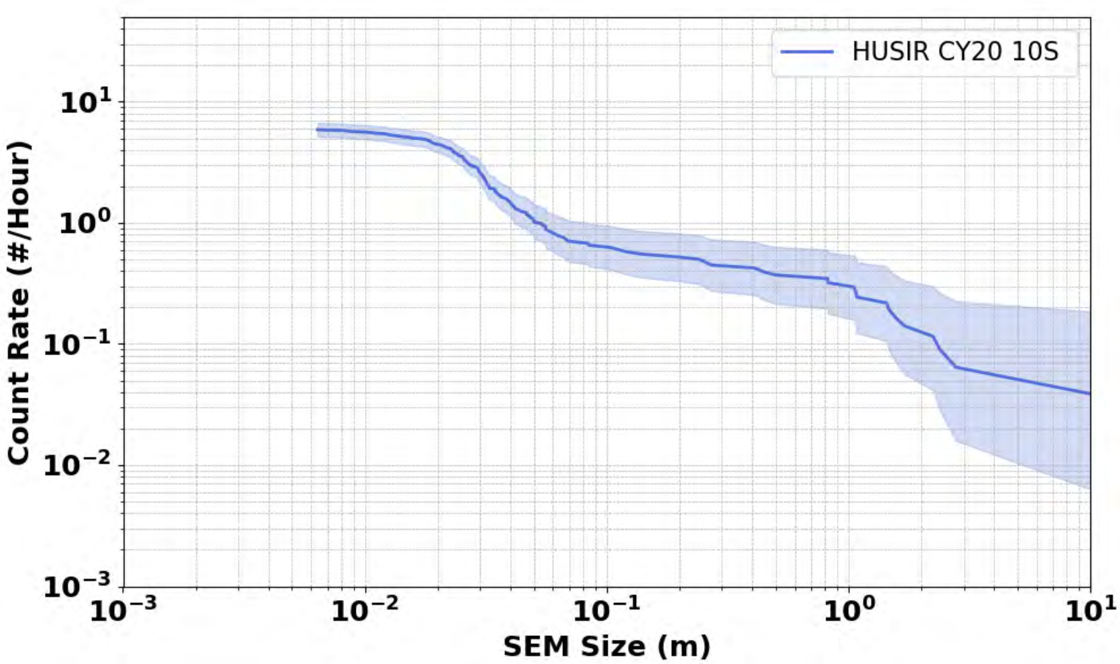

Figure E-4. Cumulative count rate versus SEM size, HUSIR 10S, CY2020.

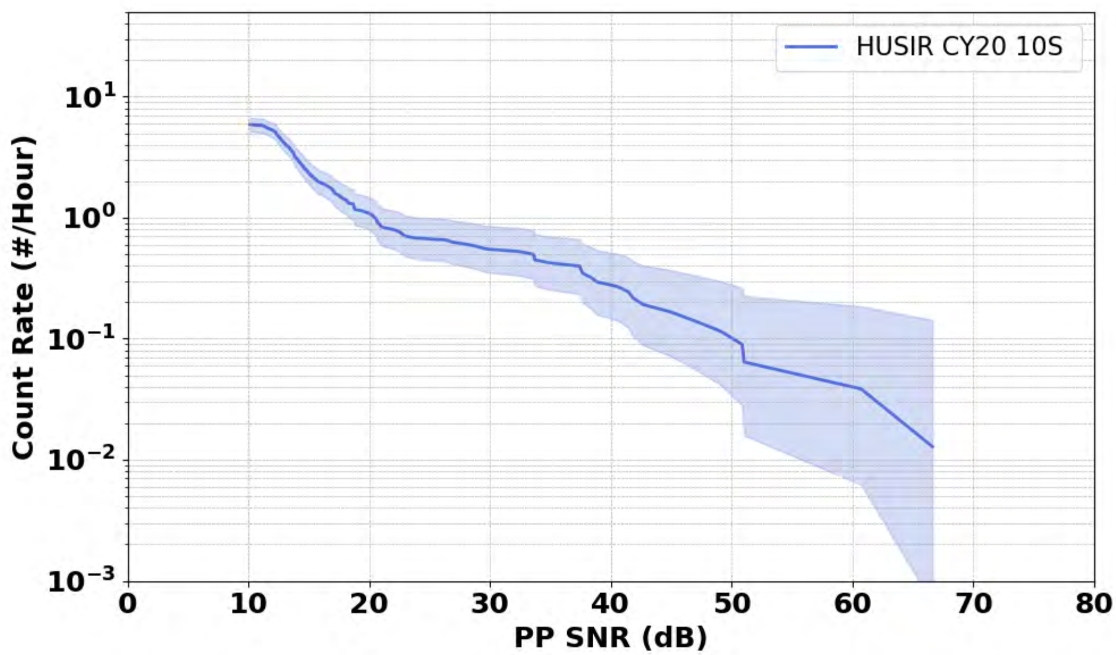

Figure E-5. Cumulative count rate versus detection SNR of the principal polarization, HUSIR 10S, CY2020.

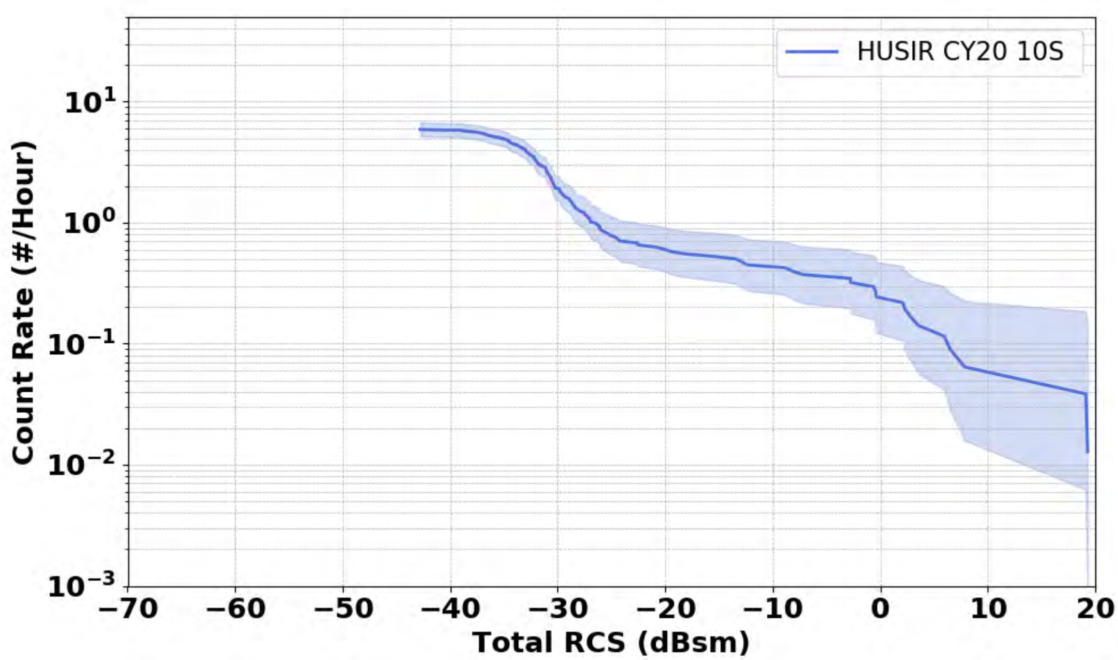

Figure E-6. Cumulative count rate versus Total Radar Cross Section, HUSIR 10S, CY2020.

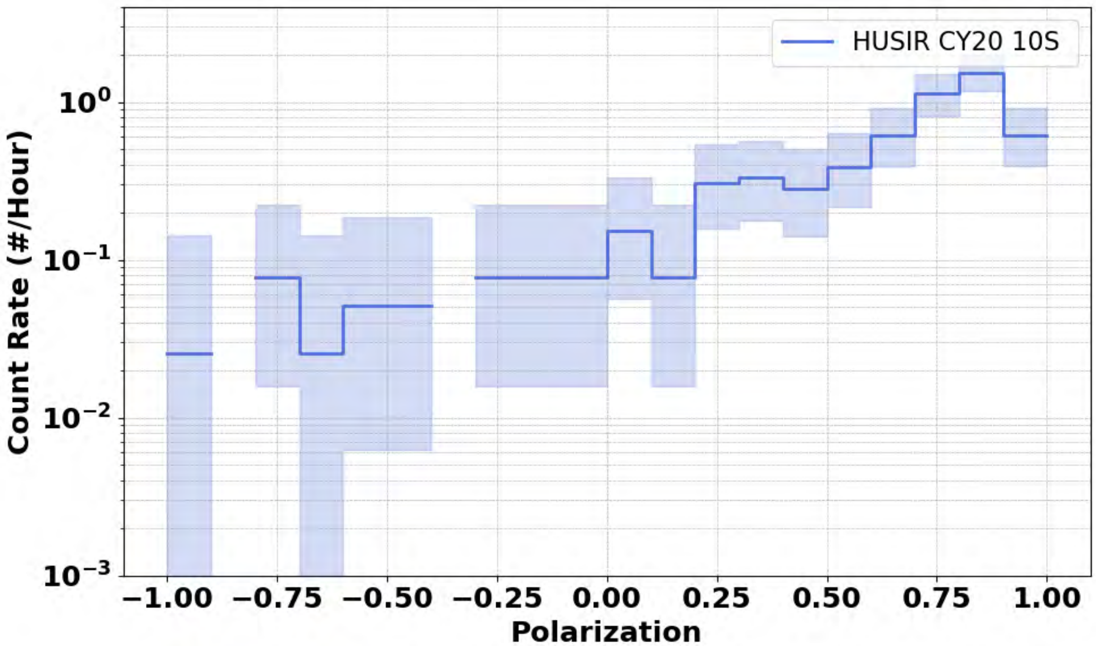

Figure E-7. Count Rate versus polarization ratio, HUSIR 10S, CY2020.
The shift of the polarization peak away from + 1 relative to the 75E distribution is related to the reduced signal strength of NaK detections relative to the OP channel noise power due to the longer slant ranges to observe the NaK population in this geometry.

Appendix F: HUSIR 10° Elevation, South Pointing, 10.1 GHz

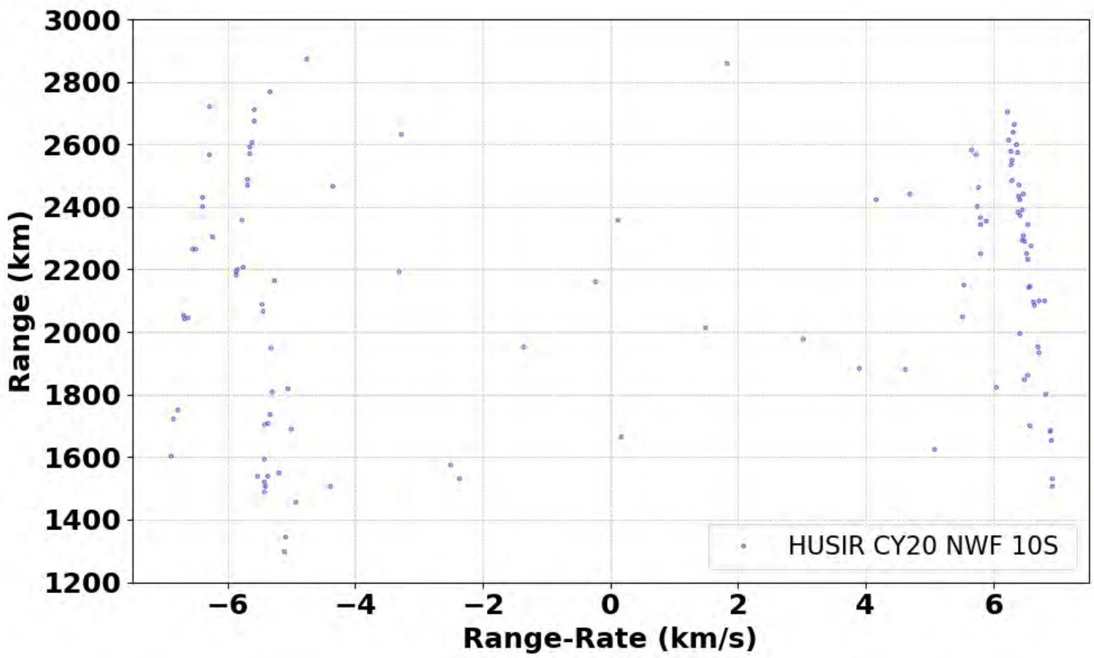

Figure F-1. Range versus Range-Rate, HUSIR 10S, CY2020.

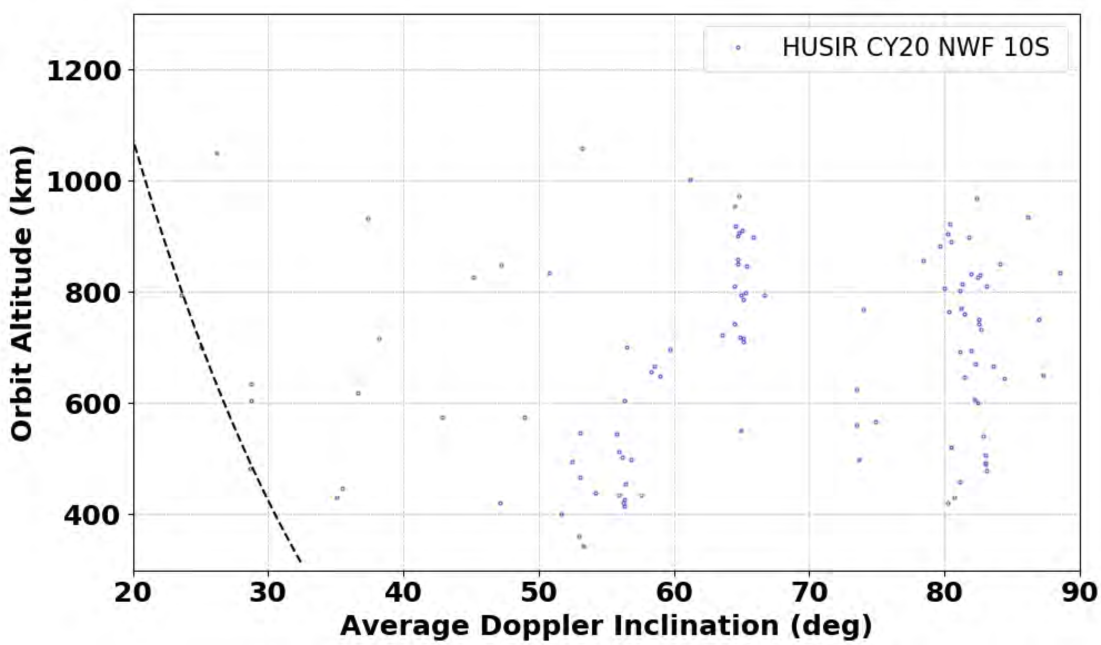

Figure F-2. Altitude versus Doppler inclination, HUSIR 10S, CY2020.
Inclination derived from Range and Range-Rate assuming a circular orbit. The dashed black line represents the minimum inclination visible to HUSIR as a function of orbit altitude.

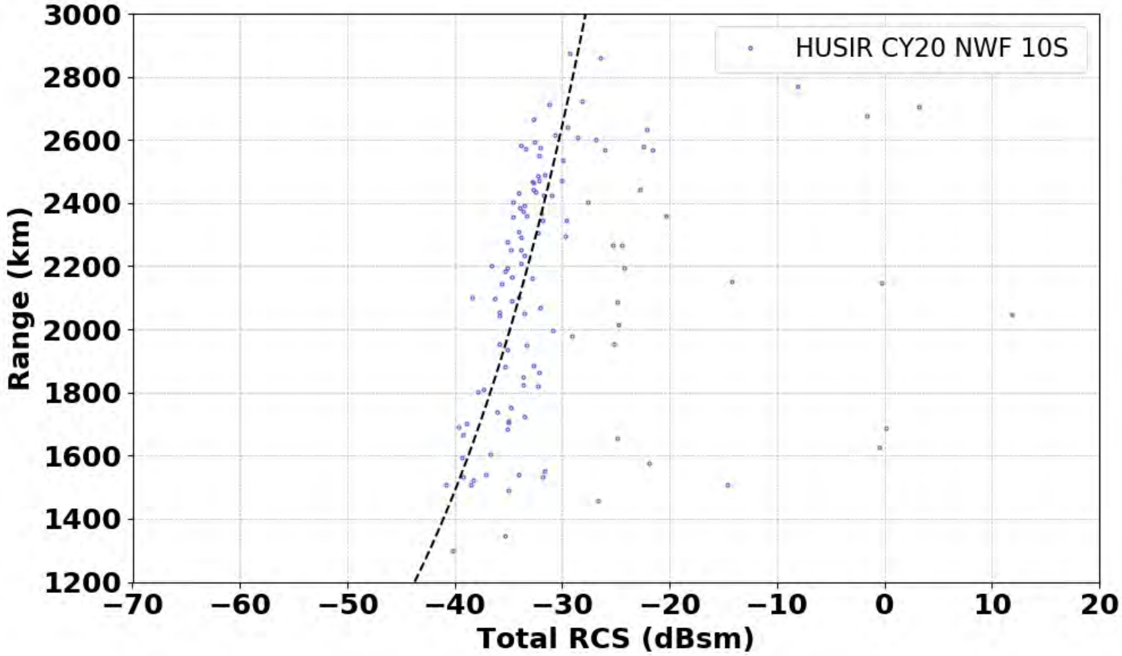

Figure F-3. Range versus Radar Cross Section, HUSIR 10S, CY2020.
The black dashed line represents the theoretical RCS of an object with a single-pulse SNR of 5.65 dB as a function of range.

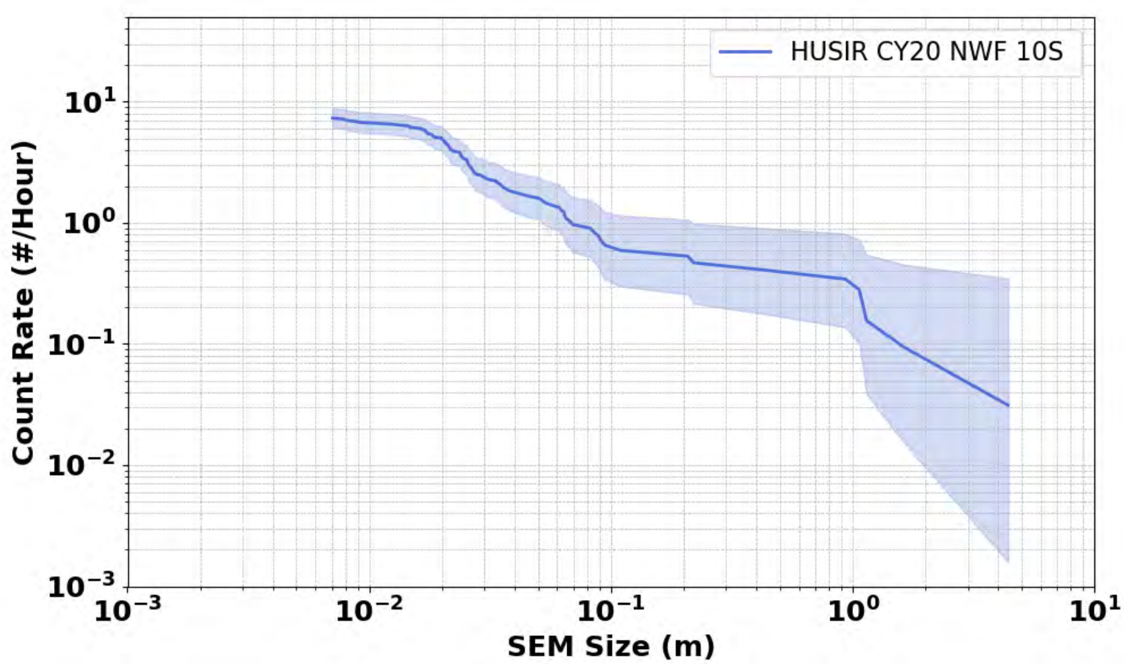

Figure F-4. Cumulative count rate versus SEM size, HUSIR 10S, CY2020.

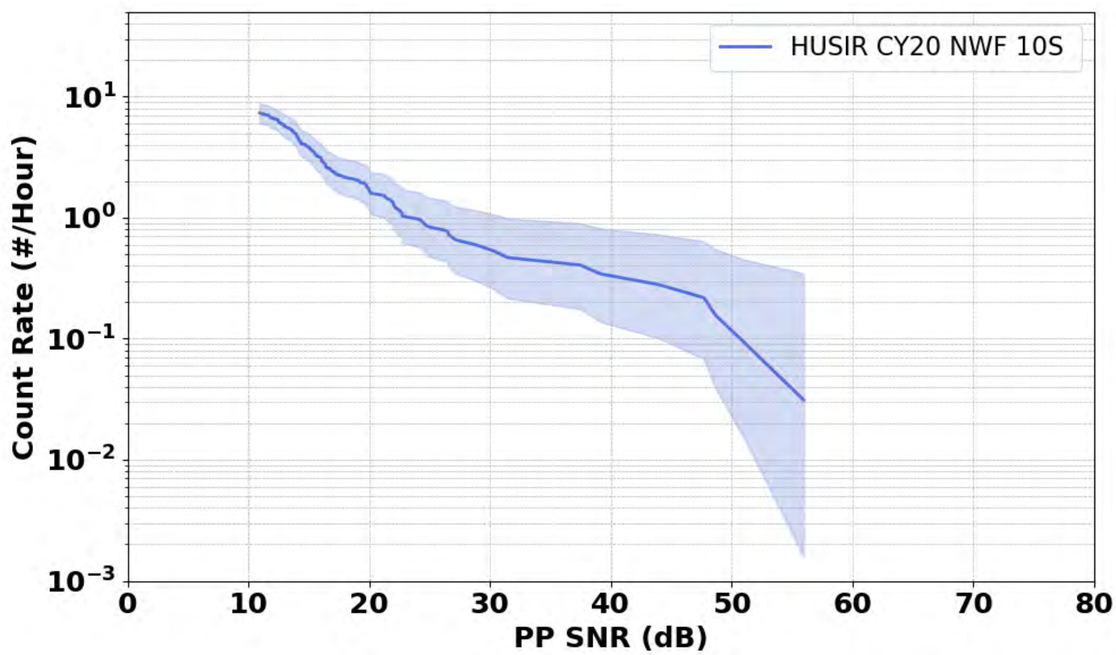

Figure F-5. Cumulative count rate versus detection SNR of the principal polarization, HUSIR 10S, CY2020.

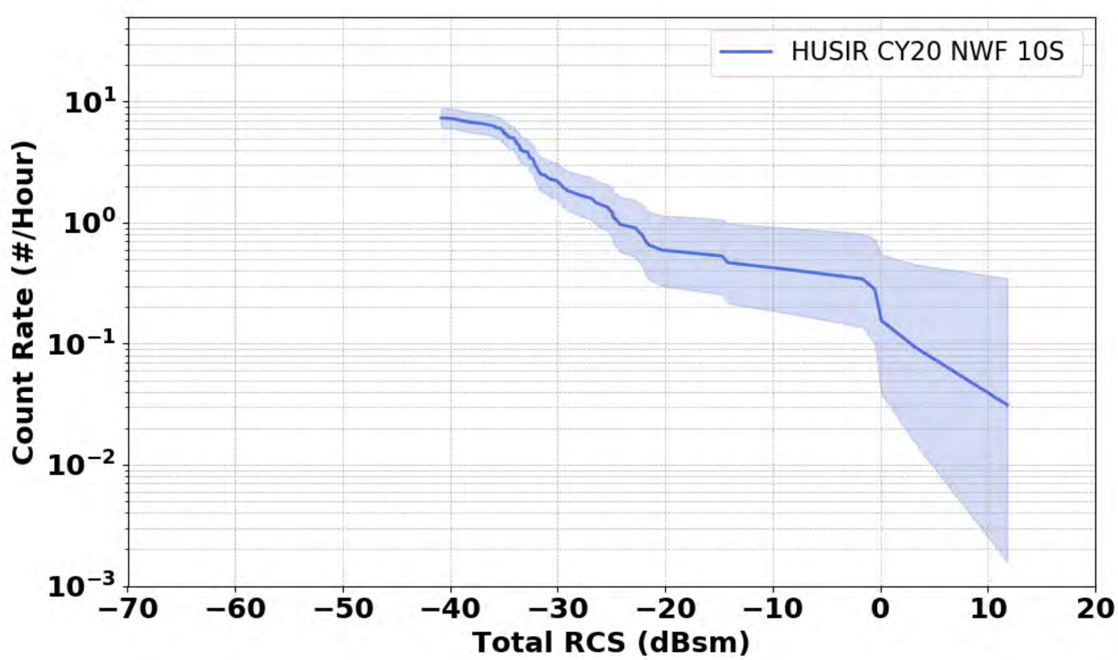

Figure F-6. Cumulative count rate versus Total Radar Cross Section, HUSIR 10S, CY2020.

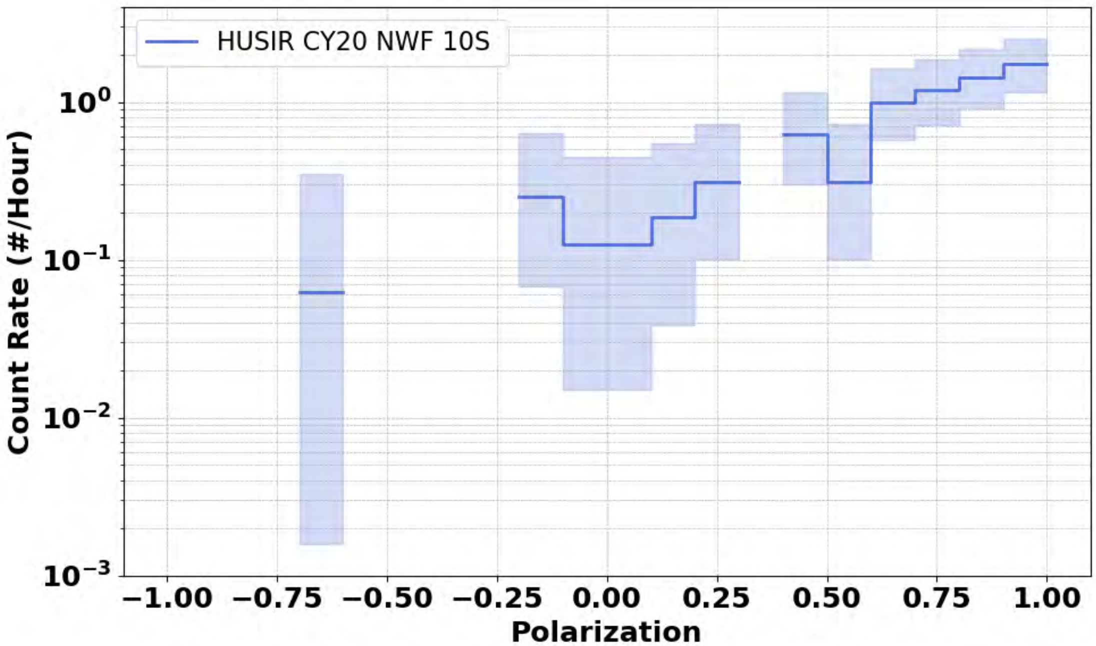

Figure F-7. Count Rate versus polarization ratio, HUSIR 10S, CY2020.
The shift of the polarization peak away from + 1 relative to the 75E distribution is related to the reduced signal strength of NaK detections relative to the OP-channel noise power due to the longer slant ranges to observe the NaK population in this geometry.

Appendix G: HUSIR 20° Elevation, South Pointing, 10.0 GHz

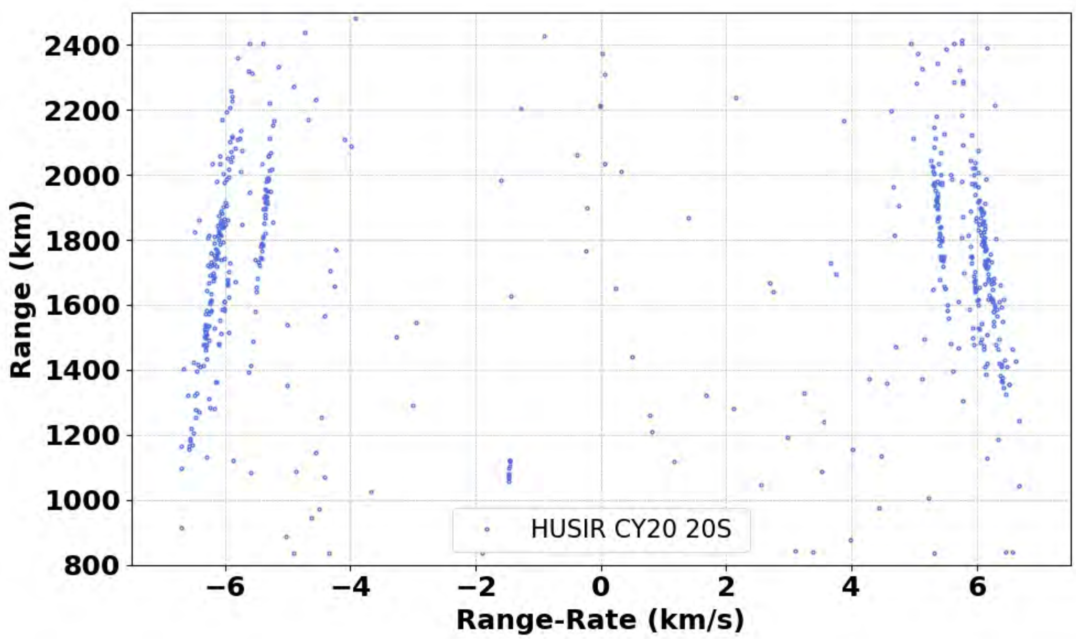

Figure G-1. Range versus Range-Rate, HUSIR 20S, CY2020.

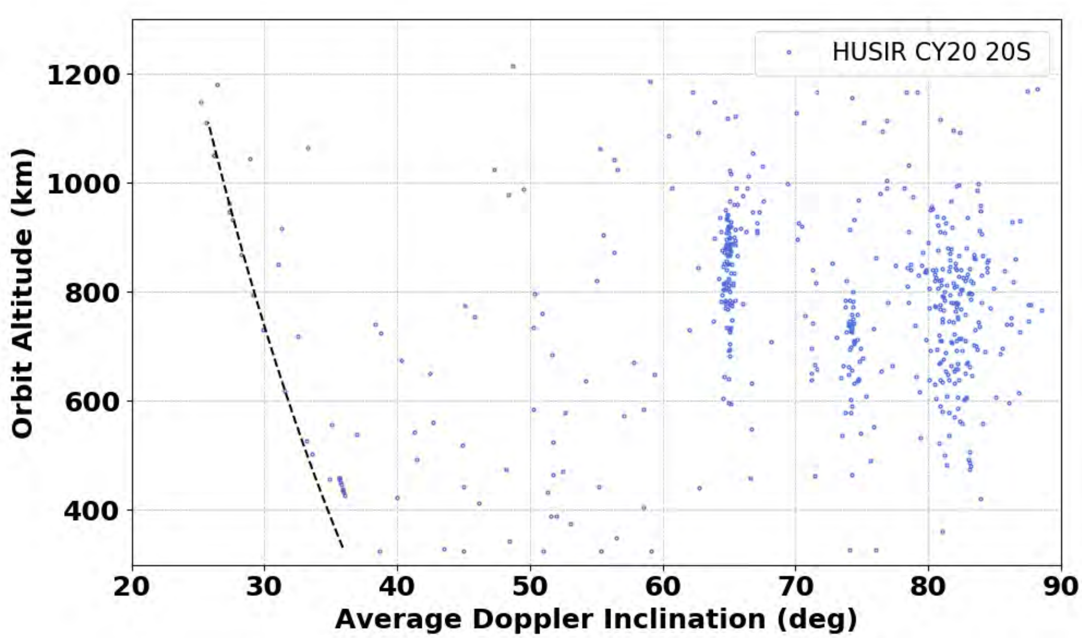

Figure G-2. Altitude versus Doppler inclination, HUSIR 20S, CY2020.
Inclination derived from Range and Range-Rate assuming a circular orbit. The dashed black line represents the minimum inclination visible to HUSIR as a function of orbit altitude.

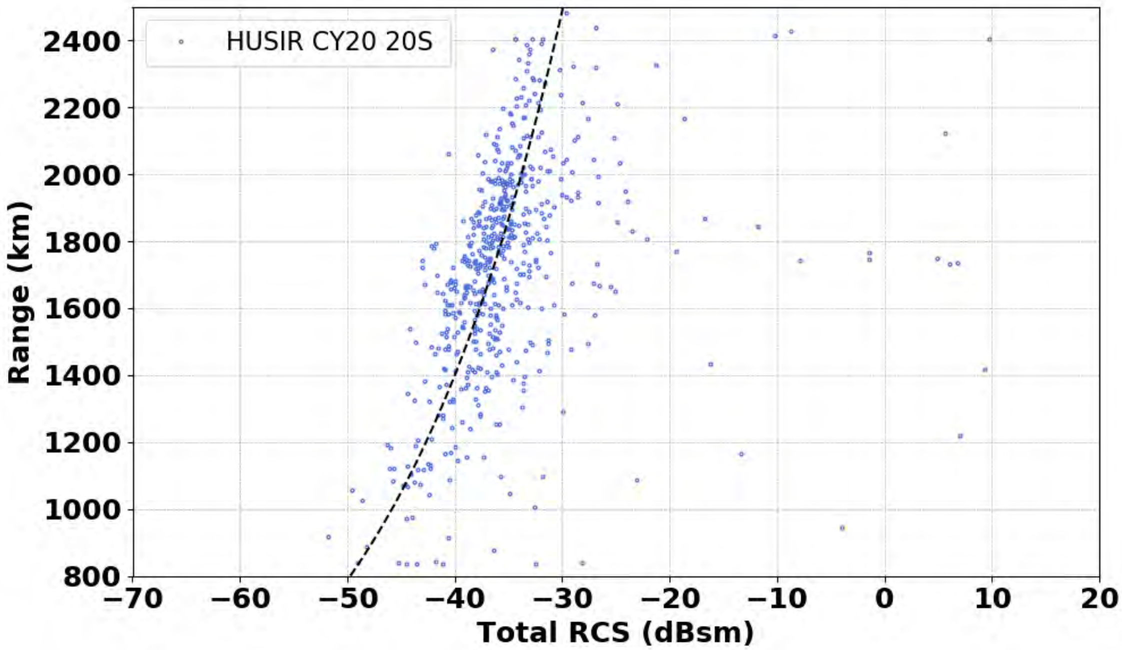

Figure G-3. Range versus Radar Cross Section, HUSIR 20S, CY2020.
The black dashed line represents the theoretical RCS of an object
with an SNR of 5.65 dB as a function of range.

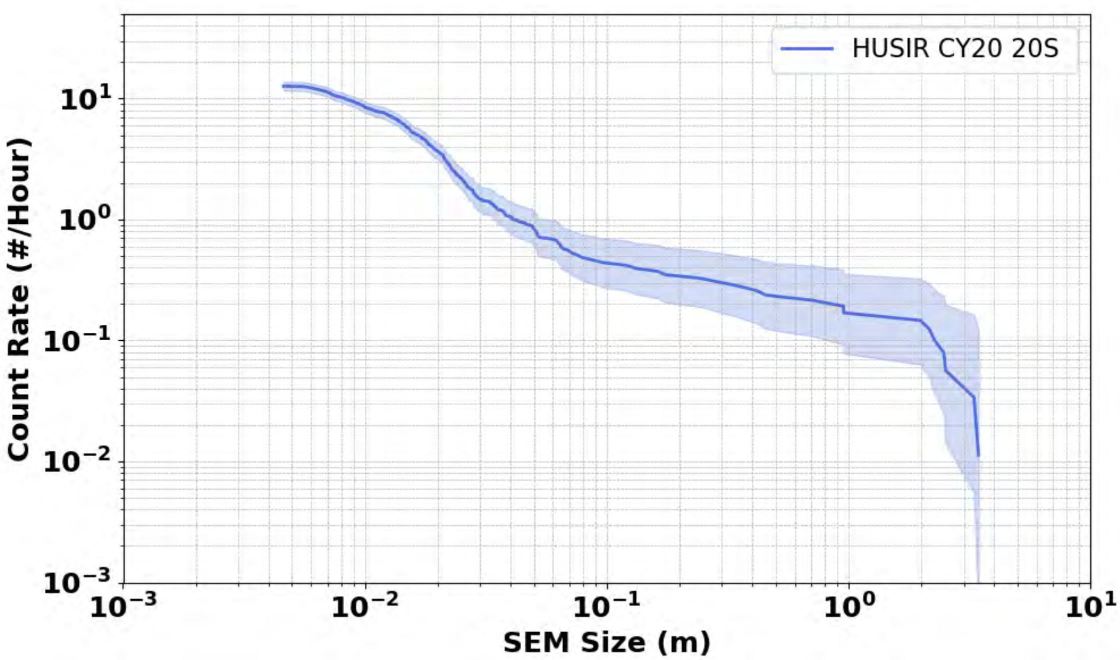

Figure G-4. Cumulative count rate versus SEM size, HUSIR 20S, CY2020.

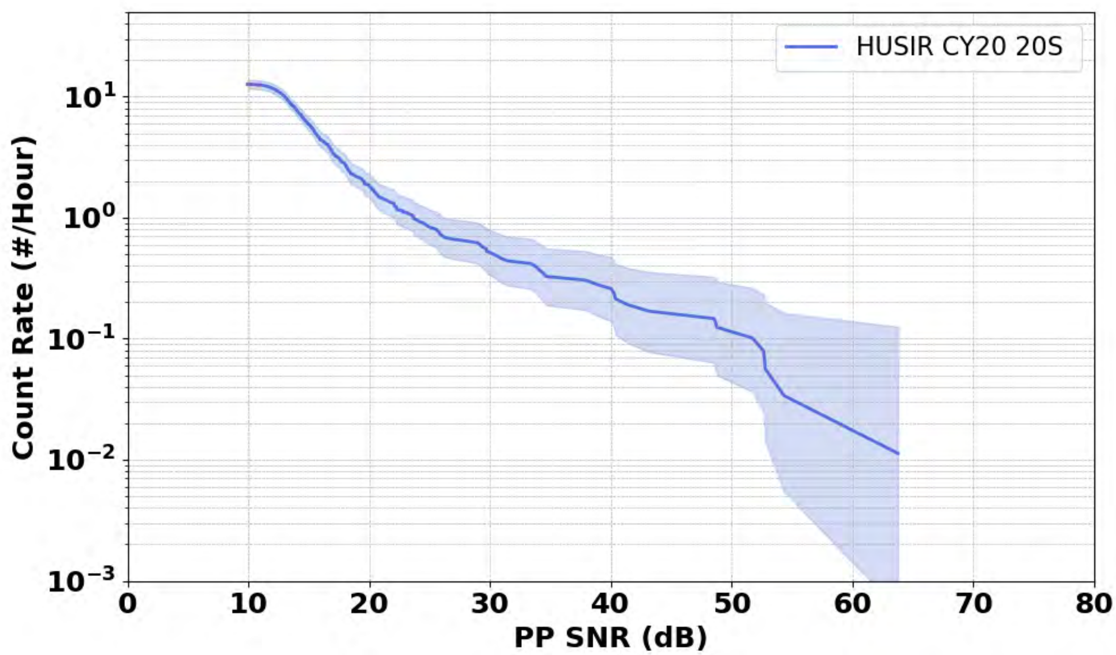

Figure G-5. Cumulative count rate versus detection SNR of the principal polarization, HUSIR 20S, CY2020.

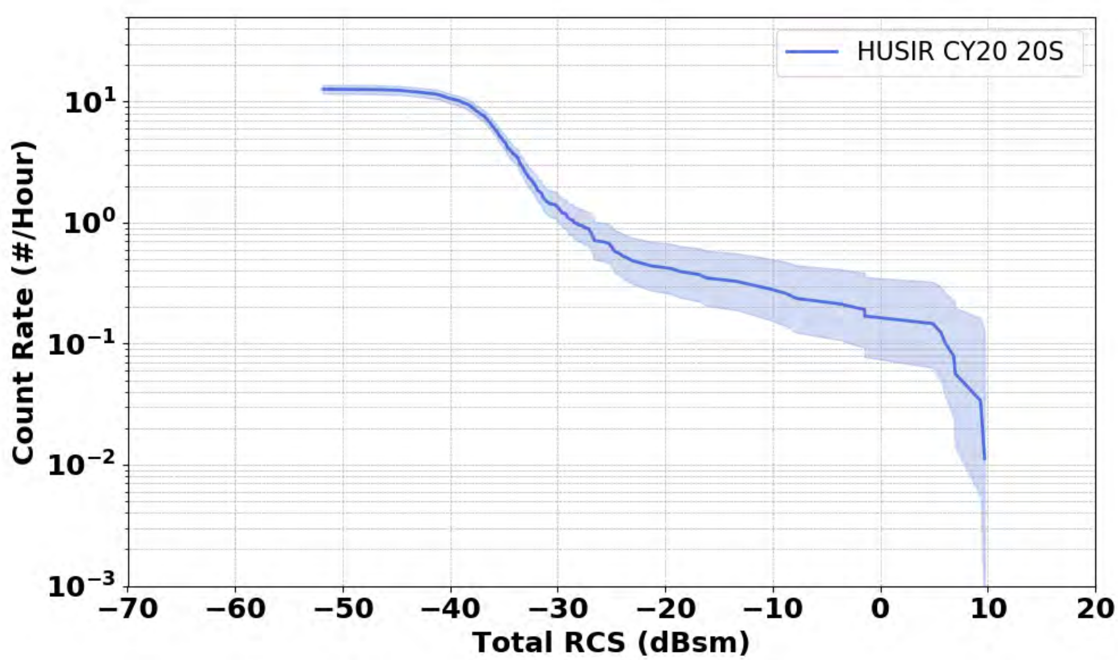

Figure G-6. Cumulative count rate versus Total Radar Cross Section, HUSIR 20S, CY2020.

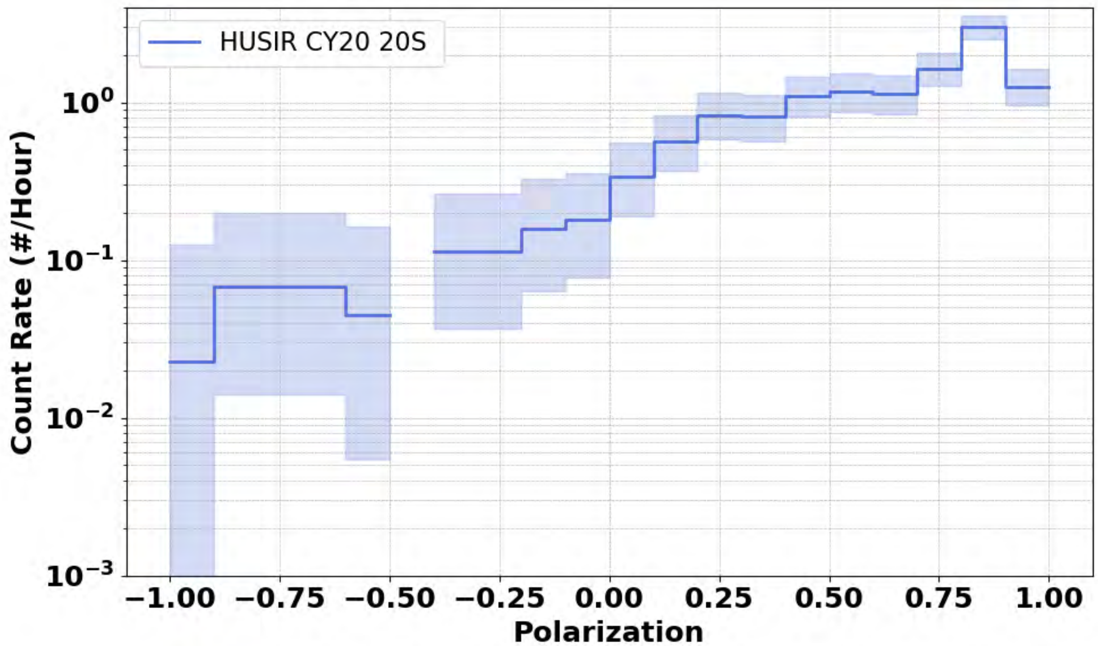

Figure G-7. Count Rate versus polarization ratio, HUSIR 20S, CY2020.
The shift of the polarization peak away from + 1 relative to the 75E distribution is related to the reduced signal strength of NaK detections relative to the OP-channel noise power due to the longer slant ranges to observe the NaK population in this geometry.

Appendix H: HUSIR 20° Elevation, South Pointing, 10.1 GHz

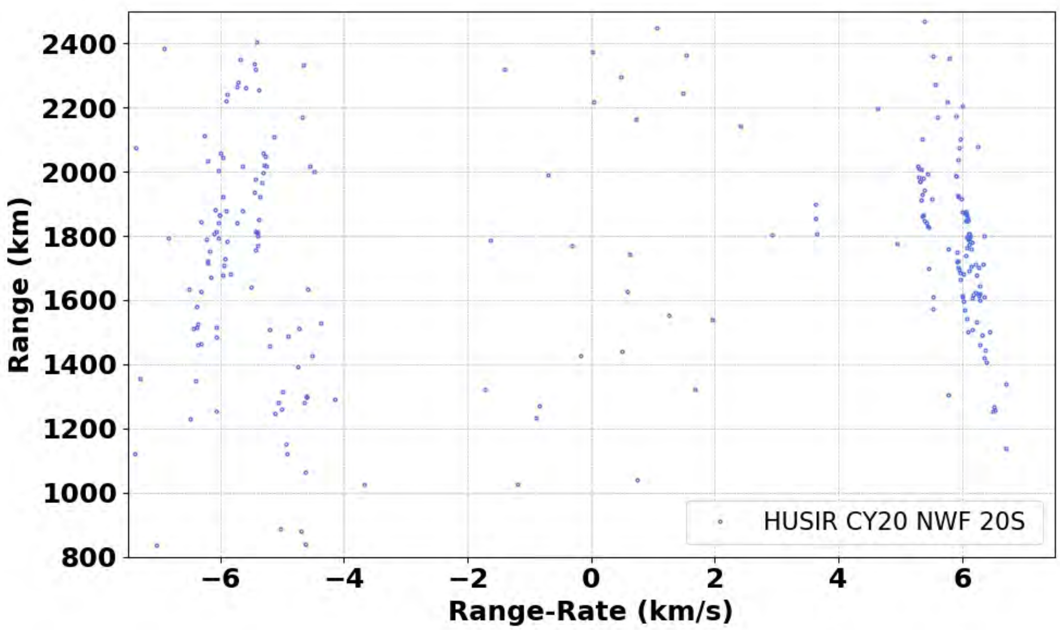

Figure H-1. Range versus Range-Rate, HUSIR 20S, CY2020.

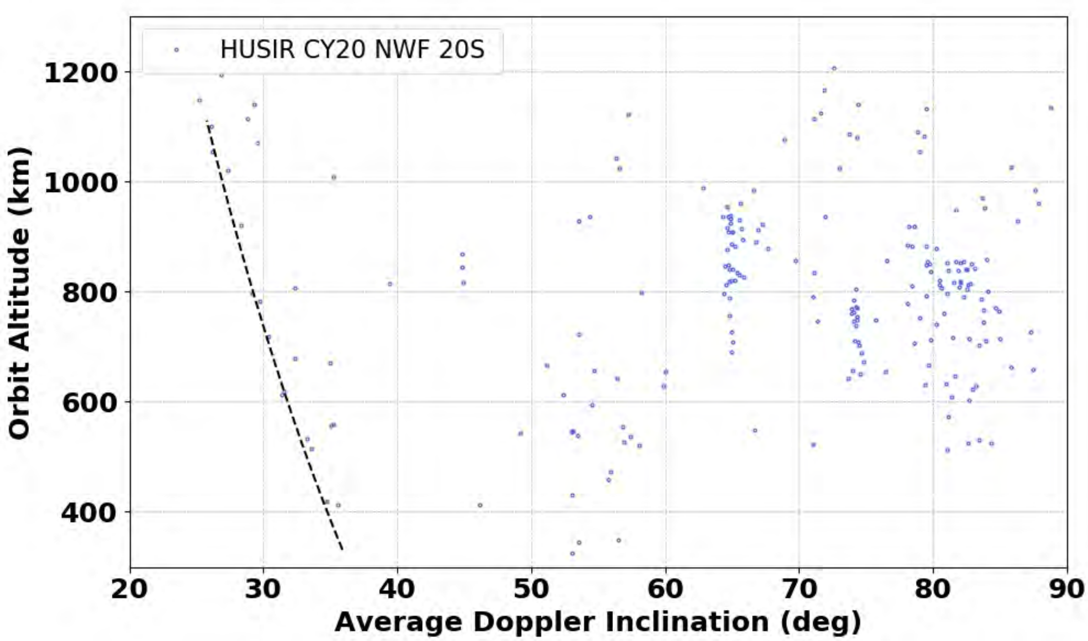

Figure H-2. Altitude versus Doppler inclination, HUSIR 20S, CY2020.
Inclination derived from Range and Range-Rate assuming a circular orbit. The dashed black line represents the minimum inclination visible to HUSIR as a function of orbit altitude.

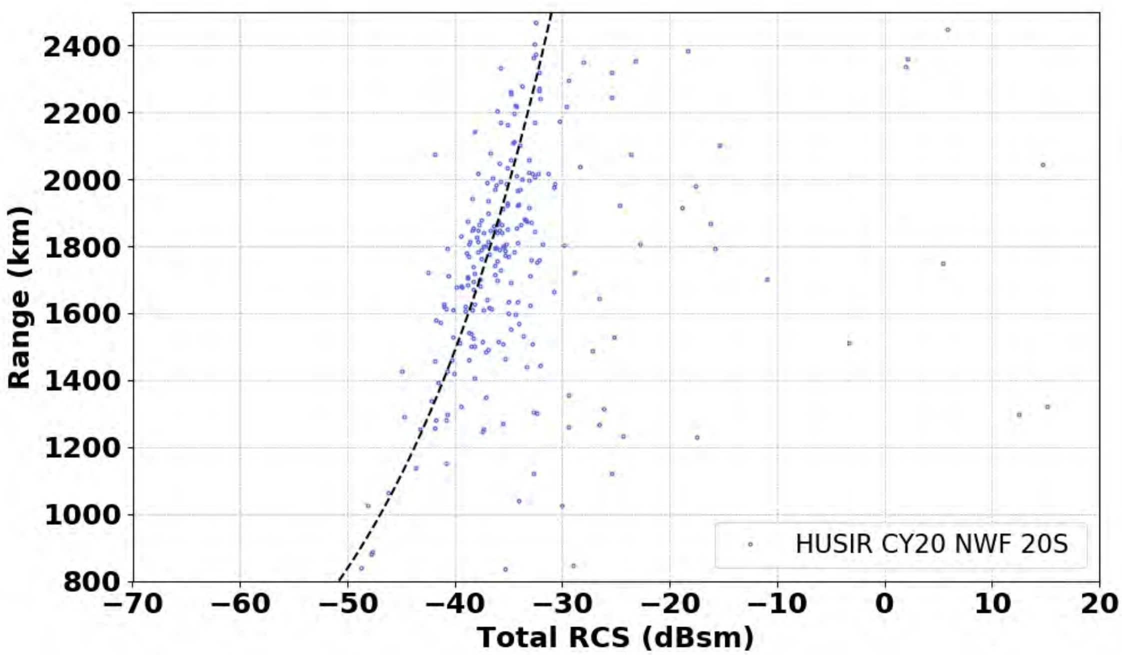

Figure H-3. Range versus Radar Cross Section, HUSIR 20S, CY2020.
The black dashed line represents the theoretical RCS of an object
with an SNR of 5.65 dB as a function of range.

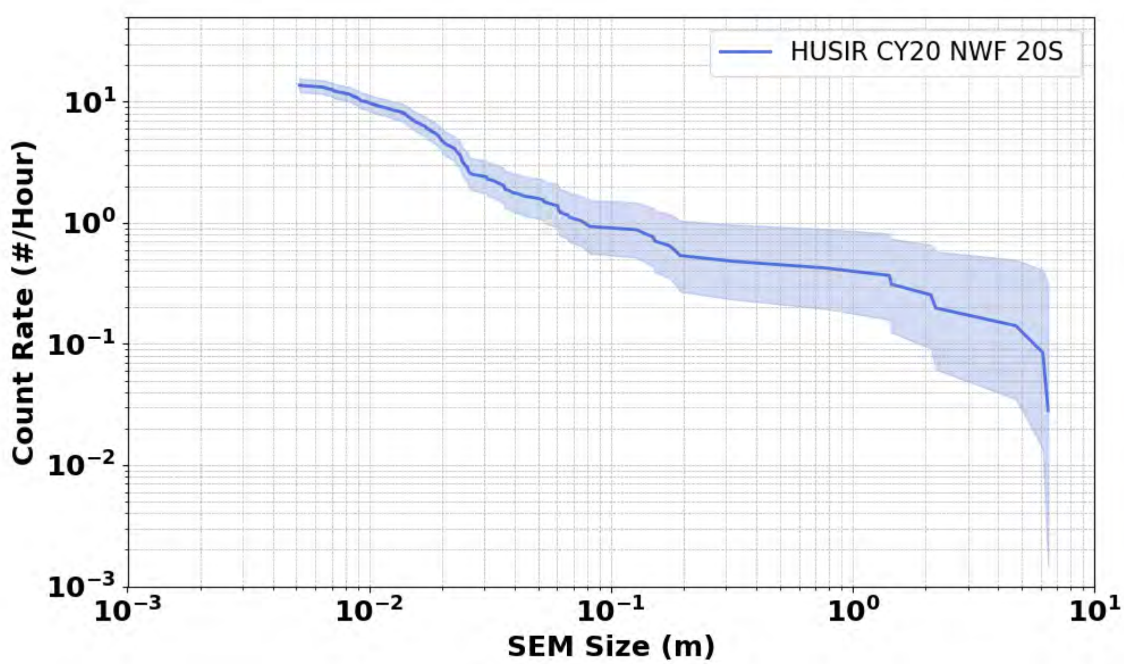

Figure H-4. Cumulative count rate versus SEM size, HUSIR 20S, CY2020.

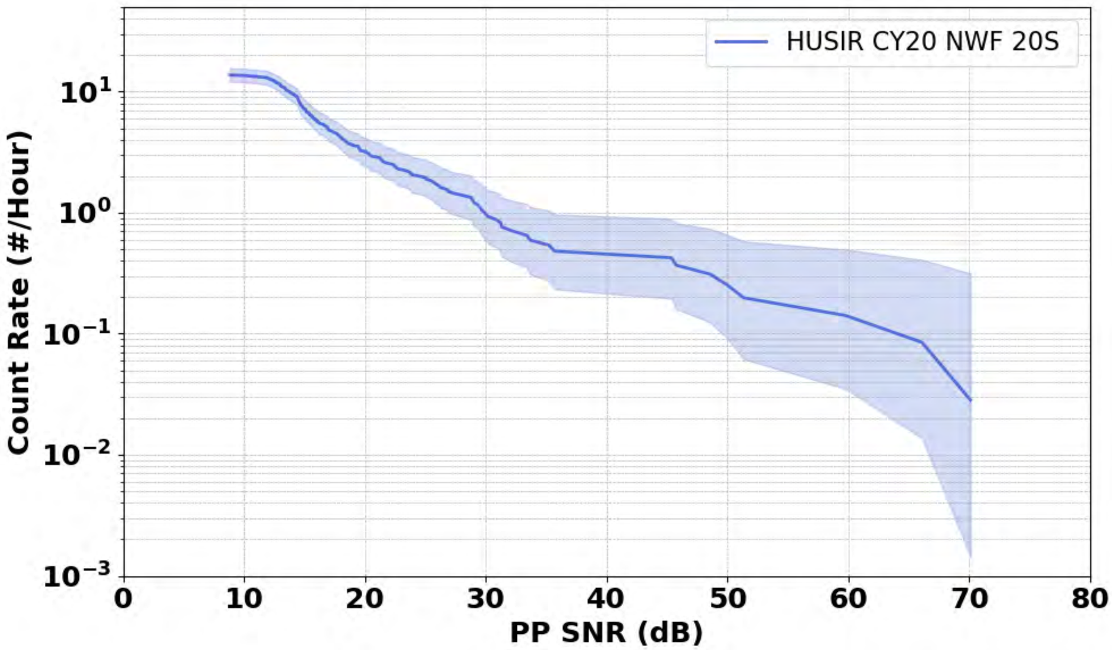

Figure H-5. Cumulative count rate versus detection SNR of the principal polarization, HUSIR 20S, CY2020.

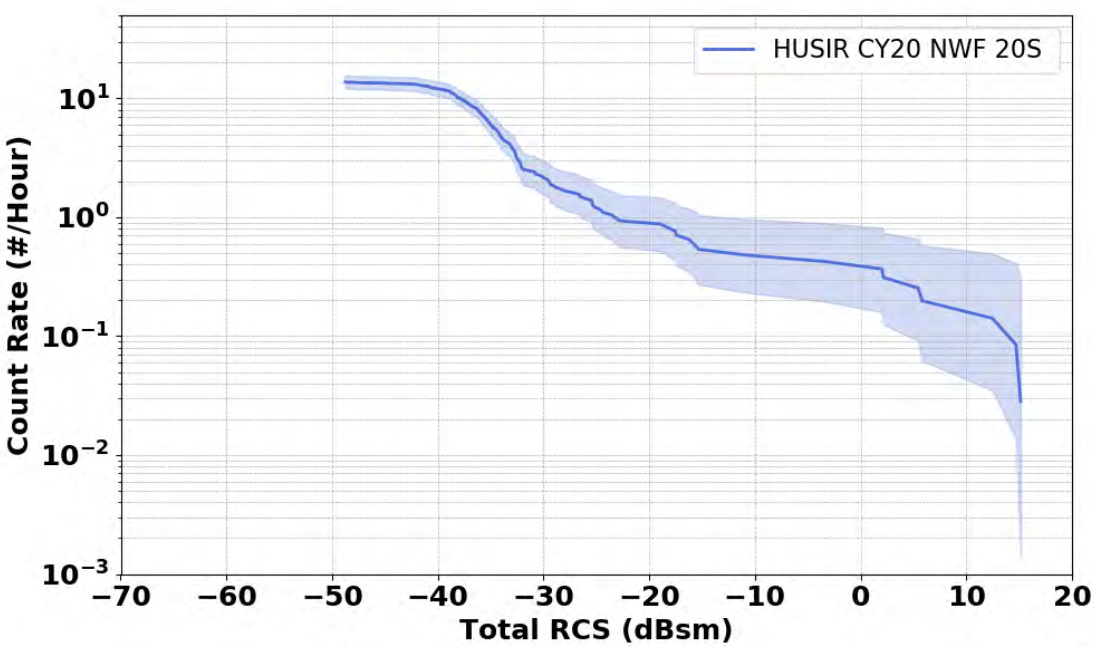

Figure H-6. Cumulative count rate versus Total Radar Cross Section, HUSIR 20S, CY2020.

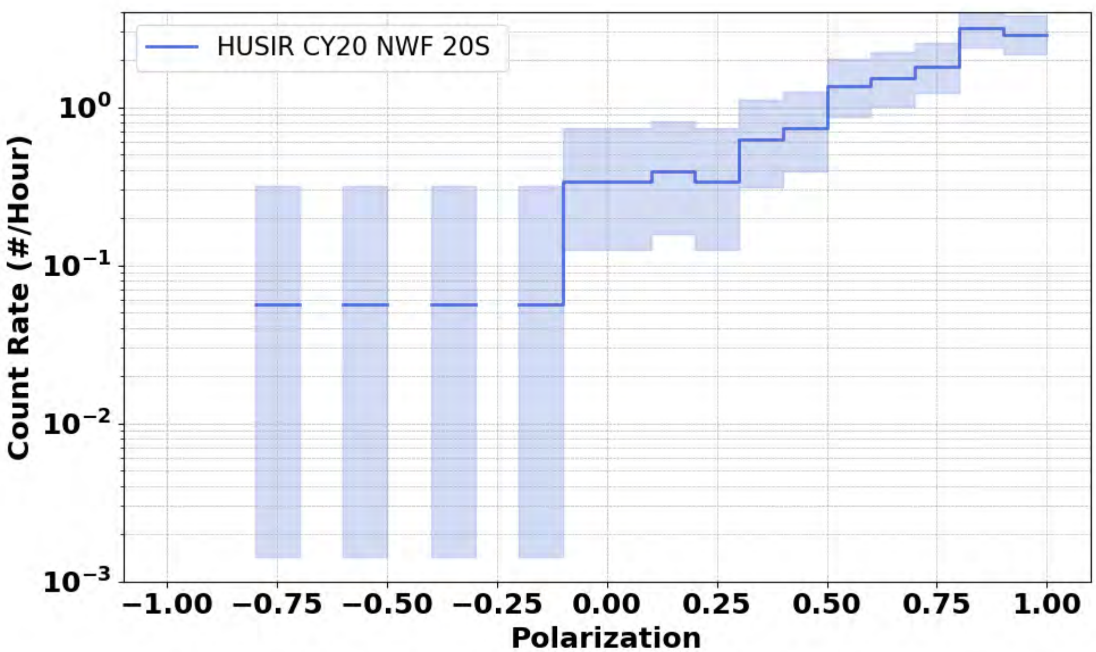

Figure H-7. Count Rate versus polarization ratio, HUSIR 20S, CY2020.
The shift of the polarization peak away from + 1 relative to the 75E distribution is related to the reduced signal strength of NaK detections relative to the OP-channel noise power due to the longer slant ranges to observe the NaK population in this geometry.